



**SETCOR**  
Conferences & Exhibitions

**The SMS/NanoMed/Sensors/EGF 2021  
International Joint Conference**

**Hybrid event - Oct 20 to 22, 2021  
Conference Proceedings**

**DOI:**

**<https://doi.org/10.26799/cp-sms-egf-nanomed-sensors2021>**

# Challenges for a High Temperature Glass Solder for the Assembly Concept of a Piezoelectric Resonator

F. Kohler<sup>1</sup>, D. Hahn<sup>1</sup>, M. Schulz<sup>2</sup>, H. Fritze<sup>2</sup>, J. Wilde<sup>1</sup>

<sup>1</sup> University of Freiburg – IMTEK, Department of Microsystems Engineering, Freiburg, Germany,  
fabian.kohler@imtek.de

<sup>2</sup> Clausthal University of Technology, Institute of Energy Research and Physical Technologies, Goslar,  
Germany

## Abstract

For the implementation of sensors with high sensitivity, low measurement uncertainty and high reliability the enclosure plays a decisive role in the temperature range up to 1000 °C. In this assembly concept for a temperature sensor a glass solder provides the connection between the ceramic components of the housing.

The resonator is a bulk acoustic wave (BAW) sensor. The propagation of the acoustic waves occurs in the 300 µm thick substrate. The sensor material is Ca<sub>3</sub>TaGa<sub>3</sub>Si<sub>2</sub>O<sub>14</sub> (CTGS) as a piezoelectric single crystal. With a melting point of 1370 °C, CTGS promises sufficient temperature stability. The body oscillation frequency and the amplitude change with temperature, which allows a sensor signal to be generated. The resonator has a keyhole-shaped platinum electrode on the top and bottom sides applied by thick-film metallization.

Various requirements are placed on this glass solder connection between the housing element and the substrate. On the one hand, it should have low electrical conductivity even at high temperatures, since a metal feed-through of the sensor contacts through this material is planned. Furthermore, the coefficient of thermal expansion must be adapted to the structural elements to avoid high thermomechanical stress. With respect to the hermeticity, the glass solder connection represents a component of the encapsulation of the sensor to the outside. It should be hermetically tight to protect the sensitive sensor from harsh environmental conditions.

Therefore, conductivity measurements on glass solder samples are performed in this work. Furthermore, the thermal expansion coefficient of the material itself is characterized as well as the expansion in connection with the housing components. The hermeticity is determined by helium leakage tests based on complete sensor housings.

Through the presented investigations, functional temperature sensors could be built according to this concept. The overall concept provides an excellent platform for further sensor.

**Keywords:** High temperature sensors, glass solder, 1000°C assembly and packaging.

## 1. Introduction

A reliable assembly concept for high-temperature sensors requires precise knowledge of the material parameters and the behavior of these materials under the influence of temperature. Among the most commonly used materials exposed to high temperatures are ceramics and glass solders. Ceramics are available on the market in different degrees of purity and thus also differ in their electrical and mechanical properties. Glass solders are multi-material mixtures of various ceramic components and can be adapted to the requirements by individual mixing [1,4].

In the overall concept of the sensor assembly, the glass solder represents the bonding technology for the individual ceramic components. It should be noted that the glass solder covers two parallel conductor tracks on the sapphire (Figure 1). Therefore, the electrical properties of the glass solder must also be taken into account in this concept.

The requirements specified in this paper for the glass solder material are given below:

- Adhesive strength with a suitable material system
- Sufficient electrical insulation properties
- Hermeticity of the housing

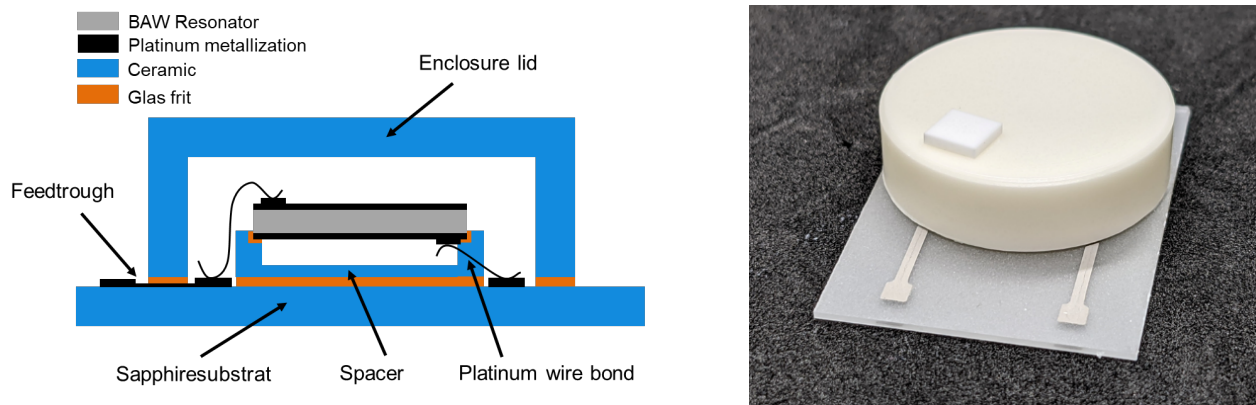


**Fig. 1:** Left: Schematic drawing of the sensor setup. Right: Realized sensor housing for the piezoelectric CTGS resonator as temperature sensor.

The design concept is shown schematically in Figure 1 (left). The substrate material is a single-crystal sapphire substrate on which platinum tracks are deposited using thick-film technology. Cap and spacer are applied to the substrate via a glass solder joint. The CTGS sensor element is fixed on the spacer with glass solder and contacted via platinum wire bonds. The final sensor assembly is shown in Figure 1 (right). Uniform outgassing of the organic binders of the glass solder can be realized through a hole in the cap. The subsequent closure takes place by a ceramic chip using a further glass soldering process step.

## 2. Technology and Materials

In this chapter, the technologies and materials used are explained in more detail. The focus is on the ceramic housing elements and the glass solder used for the production of a sensor prototype as a temperature sensor.

### 2.1. Ceramic and glass solder

Ceramic materials based on oxide, nitride and carbide show shock resistance owing to their high thermal conductivity, low CTE and high strength. Therefore, they are suitable for high-temperature applications. Depending on the purity, alumina can be used up to 1700 °C [1-3].

In the work, sapphire (single-crystalline  $\text{Al}_2\text{O}_3$ ), is used as substrate material. This is cut from wafers with a thickness of 650  $\mu\text{m}$ . The cap and spacer are manufactured with an ultrasonic milling machine and are made of multicrystalline alumina with a purity of 96 %.

The G18-385 glass solder is a reactive joining glass for high temperature applications. The material proportions of the individual components are listed in Table 1. The multi-material mix is fired at 950 °C.

Material	$\text{Al}_2\text{O}_3$	$\text{B}_2\text{O}_3$	CaO	MgO	$\text{SiO}_2$	YO	$\text{ZrO}_2$
<b>Weight percentage</b>	1-10	1-10	10-50	1-10	10-50	10-50	1-10

**Table 1:** Composition of the glass solder ingredients G18-385.

### 2.2. Temperature treatment and shear test

Two methods are used to analyse the performance of the sensor housing under thermal load. On the one hand, thermal ageing of the glass soldered ceramic samples at 1000 °C is carried out. To analyze the thermal shock resistance, cycles between 200 °C and 1000 °C are performed using an infrared oven.

Thermal shock is performed on 2 mm by 2 mm alumina chips on sapphire substrate with 9 chips per cyclization stage. The complete packages as shown in figure 1 (right) are subjected to thermal ageing for several hours.

To analyze the interconnection quality of the glass solder, glass-soldered chips are tested in shear tests. The maximum force achieved is determined and divided by the joint area. This results in the maximum shear strength for the respective chip soldered on sapphire. The tests were performed at room temperature and a shear height of 300  $\mu\text{m}$ .

### 2.3. Electronic Speckle Pattern Interferometry (ESPI)

The Electronic Speckle Pattern Interferometry is an interferometric measuring method for non-contact measurement of surface deformations. The ESPI system is equipped with a laser with a wavelength of 532.8 nm. Speckle images are taken before and after the temperature load. From the difference of the images, the deformation image can be evaluated via computer software.

In this work the ESPI is used to analyze the sapphire alumina connection. Ceramic chips are attached to the sapphire with glass solder and then measured during heating up to 500 °C on a hotplate with the ESPI.

### 2.4. Electrical measurement

The conductivity of the glass solder is a crucial variable in the application, since the glass solder connection of the housing ring represents a short-circuit between the conductor paths. Therefore, a DC measurement for the monocrystalline sapphire and the multimaterial behavior of the glass solder is carried out. The measuring setup is similar to a plate condenser. The material thickness of the sapphire sample is 650 µm. The thickness of the glass solder chip is 1.2 mm. Both sides of the chip surfaces are coated with platinum thick-film paste and electrically contacted with platinum wires with a diameter of 250 µm.

### 2.5. Hermeticity testing

In order to measure the tightness of the housing, a test is carried out in accordance with the standard (MIL-STD-883G). For this purpose, the complete housing is placed in helium atmosphere with 3,2 bar overpressure for 5 h. After removing it from the helium atmosphere, it is checked for leakage using a mass spectrometer. This was done both for unaged assemblies and for assemblies thermally aged at 1000 °C in in an oven under vacuum atmosphere.

## 3. Experimental

### 3.1. Thermal shock on glass-soldered alumina chips on sapphire and shear test

The initial shear strength shows values in the range of 60 MPa (Figure 2). Almost identical values can be obtained even after 200 temperature cycles. In addition to shear strength, the cause of failure is also an important criterion. During the first 100 cycles, the predominant cause of failure was chip fracture or sapphire fracture. No failure occurred in the glass solder layer.

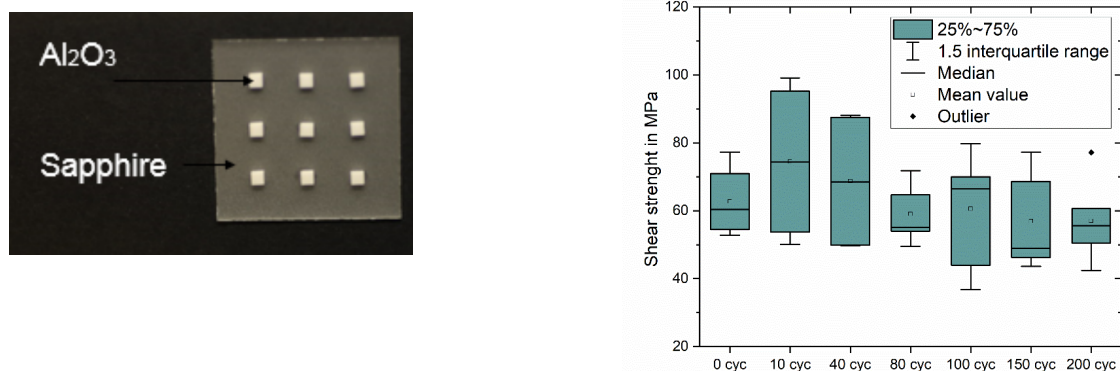


**Fig. 2:** Left: Sapphire sample with alumina chips. Right: Tested shear strength values after up to 200 thermal cycles between 200 °C and 1000 °C.

Metallographic analysis shows no cracking even after 200 temperature cycles between 200 and 1000°C (Figure 3). Likewise no layer detachment from sapphire or aluminum oxide ceramics is recognizable. It can be concluded that the glass solder connection withstands cyclic thermal load over 200 cycles between 200 °C and 1000 °C.

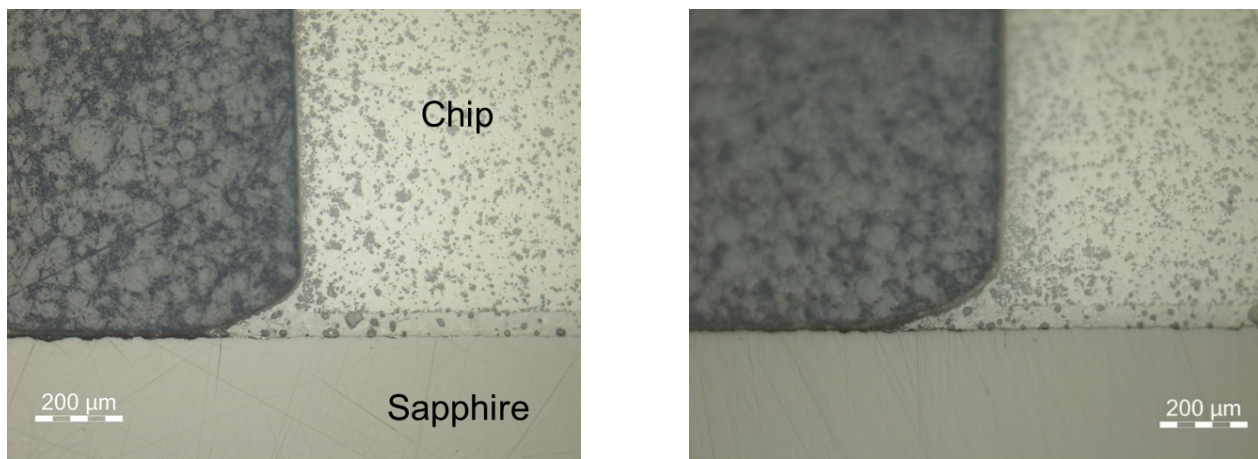


**Fig. 3:** Left: Glass soldered Al<sub>2</sub>O<sub>3</sub> chip after 40 temperature cycles (200 °C / 1000 °C). Right: Glass soldered Al<sub>2</sub>O<sub>3</sub> chip after 200 cycles (200 °C / 1000 °C).

### 3.2. Optical analysis – ESPI

The measurement in figure 4 shows a uniform shift of the chip surface over the individual temperature steps. The respective peaks lie on top of each other. This means that there is no chip bending at elevated temperatures over the measuring distance. Furthermore, due to the low deformation under temperature load, no high thermomechanical stress is to be expected.

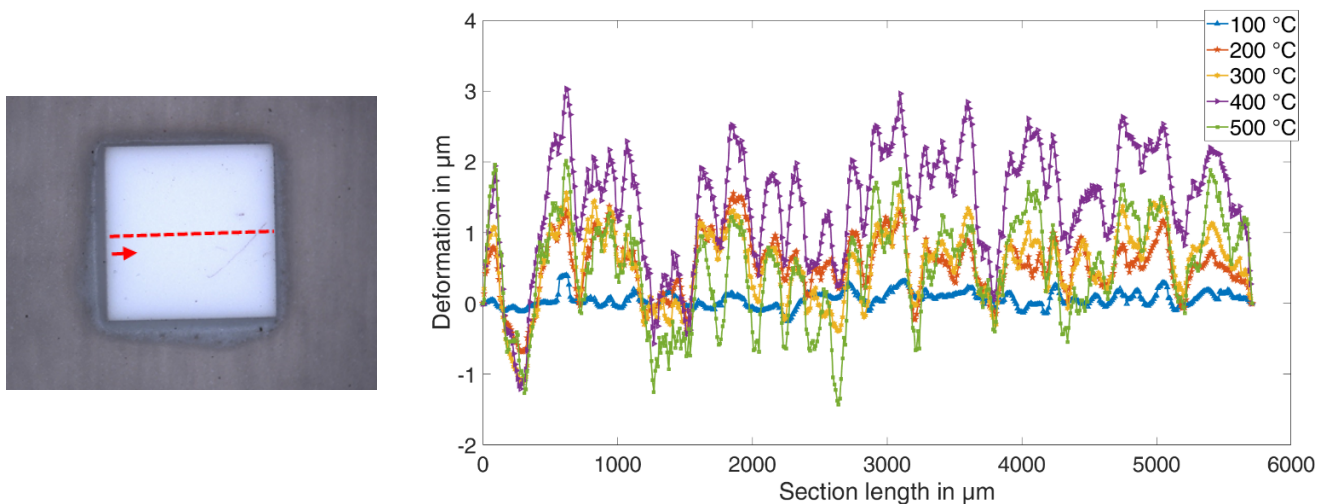


**Fig. 4:** Left: Alumina chip measured by ESPI. The red line symbolizes the measuring section for the evaluation. Right: Z-Displacement along the section of the chip.

### 3.3. Conductivity of sapphire and glass solder at high temperature

The measurement in Fig. 3 shows significant differences in the conductivity of sapphire compared to the glass solder at higher temperatures. The conductivity of the sapphire substrate increases from  $9.8 \cdot 10^{-10} \text{ S} \cdot \text{m}^{-1}$  at 400 °C to  $5.3 \cdot 10^{-7} \text{ S} \cdot \text{m}^{-1}$  at 900 °C. The increase in the conductivity of the glass solder is from  $7.2 \cdot 10^{-10} \text{ S} \cdot \text{m}^{-1}$  at 400 °C to  $8.9 \cdot 10^{-3} \text{ S} \cdot \text{m}^{-1}$  at 900 °C.

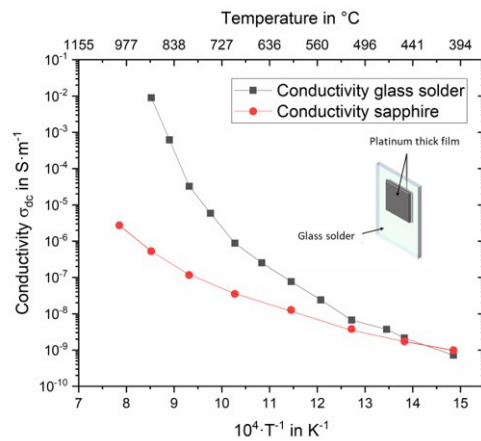


Fig. 5: Conductivity of glass solder and sapphire at temperature up to 1000 °C.

This can be attributed to the generation of carriers and thus to a higher intrinsic conductivity of the glass solder. The multi material glass has more cations, vacancies, grain boundaries and dislocations compared to the single crystal form of sapphire. Due to the geometric distance of the conductive tracks in the sensor concept, the insulating property of the glaslots can be considered sufficient even at high temperatures.

### 3.4. Hermeticity of the housing

The measured values determined by the helium leakage test show values in the range of 10<sup>-8</sup> mbar·l/s. Samples 1a and 1b were produced with the identical process steps as 2a and 2b but not in the same oven cycle. Even after thermal aging for 112 h at 1000 °C the helium leak rate keeps a value in a range of 10<sup>-8</sup> mbar·l/s.

Sample	0 hours	6 hours	12 hours	24 hours	112 hours
	Leak rate in mbar·l/s				
1a	1.5 · 10 <sup>-9</sup>	1.2 · 10 <sup>-9</sup>	1.5 · 10 <sup>-9</sup>	3.0 · 10 <sup>-9</sup>	8.0 · 10 <sup>-8</sup>
1b	5.0 · 10 <sup>-8</sup>	3.0 · 10 <sup>-8</sup>	2.7 · 10 <sup>-8</sup>	2.6 · 10 <sup>-8</sup>	2.6 · 10 <sup>-8</sup>
2a	3.0 · 10 <sup>-8</sup>	1.0 · 10 <sup>-8</sup>	1.4 · 10 <sup>-8</sup>	2.3 · 10 <sup>-8</sup>	8.0 · 10 <sup>-8</sup>
2b	5.0 · 10 <sup>-8</sup>	4.0 · 10 <sup>-8</sup>	2.0 · 10 <sup>-8</sup>	2.1 · 10 <sup>-8</sup>	2.5 · 10 <sup>-7</sup>

**Table 1:** Leakage rates of the enclosures tested in the helium leakage test. Initial and after thermal aging up to 112 h at 1000°C.

This confirms the thermal stability of the glass solder layer, which was suspected after the thermal shock tests in chapter 3.1. Furthermore, hermeticity of the glass solder connection at temperature load over 112 h at 1000 °C can be observed.

## 4. Conclusion

This work has shown the challenges that apply to a glass solder material in conjunction with a sensor housing under high temperature. The glass solder can be considered suitable for use in this sensor concept. The glass material shows stable shear strength and sufficient insulating properties at high temperature. The metallography shows no mechanical failure of the glass solder after 200 cycles with thermal cycling between 200 °C and 1000 °C. The sensor housing seems to be hermetic over 112 h at a high temperature load of 1000 °C. It can be shown by optical analysis that there is similar deformation over the glass soldered chip surface and therefore no high thermomechanical stresses at higher temperatures are expected.

The sensor concept presented represents a platform for other properties to be measured. The setup as a temperature sensor has already been functionally tested. Further setups as a pressure sensor or chemical sensor are planned.

## **Acknowledgements**

The authors thank the German Research Foundation (Deutsche Forschungsgemeinschaft, DFG) for the financial support under grants FR 1301/35-1 and WI1987/6-1.

## **References**

1. L. Roske, T. Lebey, Z. Valdez-Nava, “High temperature behavior of ceramic substrates for power electronics applications,” in *Annual Report Conference on Electrical Insulation and Dielectric Phenomena*, 2013, pp. 595-598.
2. Y. Lv, Y. Han, S. Zhao, Z. Du, and J. Fan, “Nano-in-situ-composite ultrafine-grained W–Y2O3 materials: Microstructure, mechanical properties and high heat load performances,” in *J. Alloys and Compounds*, 855, 157366. doi: 10.1016/j.jallcom.2020.157366, 2021.
3. H. Hassanin, “Fabrication of ceramic and ceramic composite microcomponents using soft lithography,” *Ph.D. dissertation*, University of Birmingham, 2011.
4. L. J. Zang, A. Sharif, H. B. Yeung, E. P. J. Rong, “Ceramic - ceramic joining using glass frit for high temperature application,” in *IEEE 14th Electronics Packaging Technology Conference (EPTC)*, doi: 10.1109/EPTC.2012.6507047, 2012.
5. F. Kohler, J. Wilde, “Assembly Technologies for Piezoelectric Sensors up to 1000 °C,” in *IEEE Electronic Components and Technology Conference (ECTC)*, doi: 10.1109/ECTC32862.2020.00334, 2020.

# New Methodology to Improve an Implantable Microsensor for NMR Spectroscopy.

José A. Bernardo<sup>1</sup>, Abel Rangel Trejo<sup>1</sup>, Adam Adewolu<sup>1,4</sup>, Lucas Werling<sup>2</sup>, Wilfried Uhring<sup>2</sup>, Luc Hebrard<sup>2</sup>, Christian Gontrand<sup>3,4</sup>, Latifa Fakri-Bouchet<sup>1,4</sup>

<sup>1</sup>Université de Lyon, CNRS, Université Claude Bernard Lyon 1, Institut des Sciences Analytiques, UMR 5280, 5 rue de la Doua, 69100 Villeurbanne, France, [jose.bernardo@etu.univ-lyon1.fr](mailto:jose.bernardo@etu.univ-lyon1.fr), <sup>2</sup> Icube ICube Laboratory, Université de Strasbourg, 67037 Strasbourg, France, <sup>3</sup> Institut de Nanotechnologies de Lyon, 69621 Villeurbanne, <sup>4</sup> INSA Lyon, France, [Latifa.fakri-bouchet@insa-lyon.fr](mailto:Latifa.fakri-bouchet@insa-lyon.fr)

## Abstract

The opportunity to predict and optimize from the expected performances (high Q factor and Signal to Noise Ratio - SNR) the geometry of the NMR microcoil would lead to the manufacture of different desired geometries (Rectangular, Ellipsoidal, Square and Circular) with the optimal dimensions according to the application. In our case, the needle microprobe (micro-coil + Transmission Line + connecting path) is dedicated to detect small samples and low concentrations of analytes using localized NMR spectroscopy (MRS). In This work, we demonstrate the relevance of using an Artificial Neuronal Network (ANN) to design the implantable NMR microsensors, predicting their performance parameters in terms of Q factor and SNR. We performed an ANN model, and reached an accuracy of 99.67% for the model Test (which corresponds to RMSE = 0.0322). Our ANN model was trained, validated and tested using a dataset from simulation (6528 data observations), generated through the 3D-TLE (Transmission Line Extractor), a GUI (Graphical User Interface) platform developed in MATLAB. We will be able to generalize this optimization (multi-parameter) solution dedicated to the NMR micro-antenna for any sensor and other applications.

**Keywords:** Microcoil, Electrical parameters, Q factor, SNR, 3D – TLE, ANN, ML, NMR Spectroscopy.

## 1. Introduction

One of the main challenges of the Nuclear Magnetic Resonance (NMR) and, more particularly Nuclear Magnetic Resonance Spectroscopy (MRS) is improving its sensitivity and spectral resolution in the case of weak metabolites concentration in a small region of interest (ROI ~ 2 $\mu$ L-3 $\mu$ L for our applications).

The NMR sensitivity has been a subject of numerous studies for years. Thus, several approaches were already proposed for its optimization. Using a higher static magnetic field can improve the sensitivity in terms of Signal to Noise Ratio (SNR) [1]. The enhancing of sensitivity of the Radio Frequency (RF) receiver coil. In our case, we miniaturize the implantable NMR antenna; thus, the microcoil part will be adapted to the sample dimension, improving its filling factor and its SNR performance criteria. However, multiparametric simulation work is required to optimize the microprobe (Q factor and an SNR) before its fabrication.

Nowadays, artificial intelligence (AI), more particularly Artificial Neural Networks (ANN), has been widely used in several application areas: Predict the resonance frequency of a rectangular micro-strip Antenna at its fundamental mode, for several substrate thicknesses [2]. Change the geometry of the microstrip antenna from a rectangular to an equilateral triangle [3]. Recently, ANN has also been used to solve complex problems such as antenna parameters extractions. ANN has become an extremely useful tool for modelling complex systems with elaborate mathematical functions between inputs and outputs. The advantages of ANN assisted antenna modelling are: reducing complexity, time, and cost compared to traditional computational modelling, and ultimately leading to accurate data set analysis and prediction[4]. These advantages represent a great asset in dealing with the complexity of our microprobe structure and the optimization of its performances.

This work demonstrates how the ANN succeeded in predicting the microprobe performances by training AI model with dataset generated by simulations using 3D-TLE (Transmission Line Extractor) according to its geometrical parameters, material properties, and working frequency for an NMR spectroscopy application.

## 2. Materials and Methods

### 2.1. Microprobe Sensitivity criterion definition

Microprobe sensitivity can be defined as the ratio of the SNR and the sample concentration ( $[C]$ ):

$$S_c = \frac{SNR}{[C]} \quad (1)$$

With SNR defined by:

$$SNR = \frac{\text{signal}}{\text{noise}} \propto \omega_0 B_0 V_e \frac{B_1}{i} \frac{1}{\sqrt{k_B T R \Delta f}} \quad (2)$$

Where  $\omega_0$  is the angular resonance frequency,  $B_0$  is the static magnetic field,  $V_e$  is the volume of the sample,  $\frac{B_1}{i}$  is the RF magnetic field by a current  $i$ ,  $k_B$  Boltzmann constant,  $T$  is the system temperature,  $R$  is the microprobe resistance and  $\Delta f$  the bandwidth. In the literature, the SNR formula is reduced to:

$$SNR \propto \sqrt{\eta Q} \quad (3)$$

In the optimal case of the filling factor  $\eta \approx 1$ , the probe sensitivity is quickly evaluated by the Q factor that is easy to calculate from the frequency response of the circuit [5].

$$Q = \frac{L\omega_0}{R} \quad (4)$$

When the NMR micro-coil is miniaturized, the noise would essentially come from the microprobe resistance [6], given the sample noise becomes negligible [5]. Thus, the equivalent microprobe resistance is defined by the following equation:

$$R_{AC} \approx R_{DC} + R_\delta + R_{proximity} \quad (5)$$

The AC resistance includes the ‘ohmic’ values of all wires in presence, the static resistance due to the skin effect [7] and the one of proximity effect [8] that is usually neglected.

So, the AC resistance was calculated by:

$$R_{AC} = \rho \frac{2l_{avg}}{\pi \delta (t+w-2\delta)} \quad (6)$$

Where the skin thickness ( $\delta$ ) is defined by:

$$\delta = \sqrt{\frac{\rho}{\pi \mu f}} \quad (7)$$

With:  $\mu$ , Magnetic permeability of the wire [ $Hm^{-1}$ ],  $f$ , alternating current frequency [ $Hz$ ],  $\rho$ , electrical resistivity [ $Sm^{-1}$ ] and  $l_{avg}$ , length of the copper stripline [mm].

### 2.2. Microprobe designing and simulation

The microprobe dataset was generated by performing a numerical simulation of microprobe Resistance and Q factor thanks to the 3D-TLE (Transmission Line Extractor) platform and ADS (Advanced Design System) software. We simulated the micro-coil part, designing four geometries (rectangular, square, circular and Ellipsoidal). 3D-TLE, the homemade software, helped extract the transmission line electrical parameters [9]. So, we could deduce the microprobe resistive losses. Figure 1 summarizes the blocks diagrams representing the main steps to simulate microprobe performances. Thanks to this, we generated 6528 observations, used for training, validations and test. The microprobe dataset includes four micro-coil geometries, eight working frequencies (from 200 MHz to 900 MHz), and two substrate types (glass and silicon).

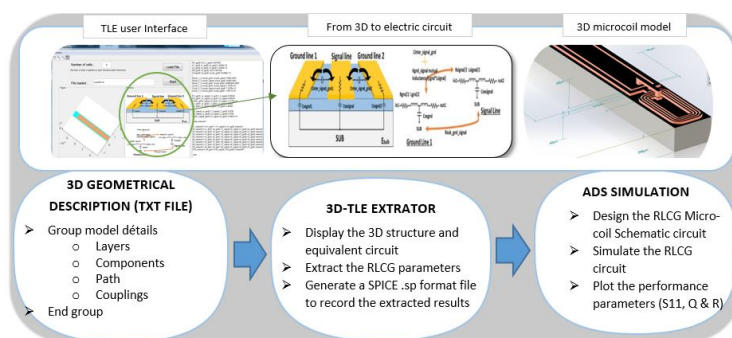


**Fig. 1.** Block diagrams of the simulation methodology: TLE user interface to 3D micro-coil mode

## 2.2. ANN Modelling

The Artificial Neuronal Network (ANN) was developed using the MATLAB Toolbox, Deep Learning (DL). Figure 2 shows the ANN shallow architecture we used for AI model training. Note that, between the input layer (Predictors) and the output layer (Targets), there is only one hidden layer that we optimized making trial testing. As hyper-parameters, we use a hyperbolic tangent (*tanh*) function activation for the hidden layer and a Rectified Linear Unit (*ReLU*) for the Output layer. To train our model, we developed a custom-made script to automatically test a different number of neurons from the hidden layer. That script allows choosing the optimal amount of neurons from the hidden layer in terms of RMSE (Root Mean Square Error) and Test dataset performance.

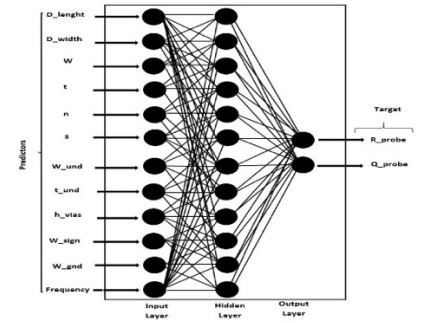


**Fig. 2.** ANN architecture for Microprobe dataset training model.

## 3. Results

The following table summarizes the Model Testing performance. We have three prediction cases, 1<sup>st</sup> model predicting both targets together, 2<sup>nd</sup> and 3<sup>rd</sup> for each performance parameter separately (Q factor or Resistance).

Targets	ANN	RMSE	<R <sup>2</sup> > (%)
[R_probe Q_probe]	12 : 52 : 2	0.977	96.56
[Q_probe]	16: 48 : 1	0.032	99.79
[R_probe]	15 : 44 : 1	0.042	91.34

**Tab.1.** Performance from different ANN architecture for three target cases.

Figure 3 shows that microprobe Q-factor, resistance prediction, and the corresponding true data values from the ANN model are in good agreement. Thus, with this ANN model we are able to accurately predict the Q factor and its Resistance of any microprobe.

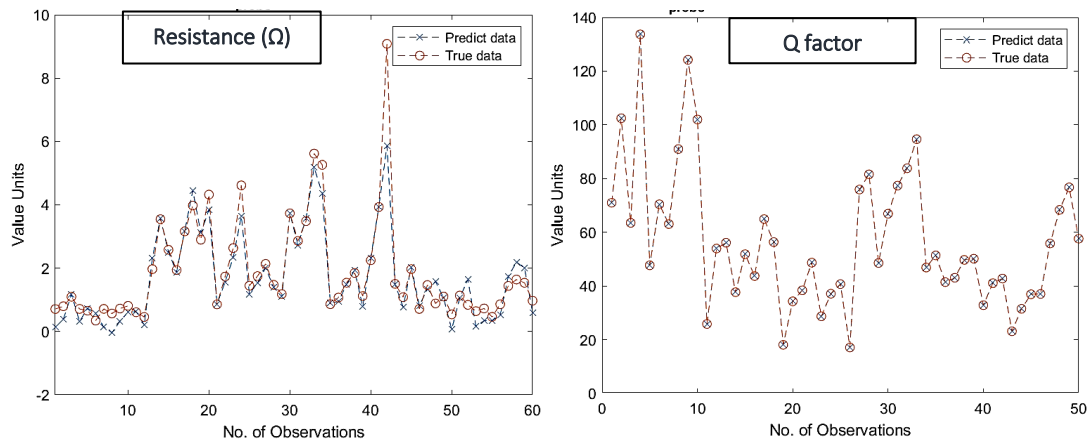


**Fig.3.** The microprobe parameters prediction and the true value after the trial number optimization

## 4. Conclusion

Throughout our study, we demonstrated that our 3D-TLE platform combined with Machine Learning (ML) represents a new and powerful tool to improve NMR microprobes performances. We are able to predict the microprobe performance based on its geometrical parameters for four different shapes, materials electrical properties and working frequency. We were able to predict the Q-factor very accurately (RMSE = 0.0316, which corresponds to 99.79% of the model accuracy in the Test performance). The resistance prediction, in that case, is about 91.34% accurate and still need some enhancement.

The proposed ANN Model can be applied to the designing and optimization of RF coils and microcoil used in MRS or MRI application. It provides, in short time, very accurate performances parameters information for a rapid comparison of different NMR coil designs.

### **Acknowledgements**

The authors would like to thank the National Research Agency (ANR) for financial support through the ANR-16-CE19-0002-01 project and Dr Y. Zaim Wadghiri from *Grossman School of Medicine, New York University*, for his help in simulating micro-coils using CST MWS® software.

### **References**

1. D. I. Hoult and R. E. Richards, 'The signal-to-noise ratio of the nuclear magnetic resonance experiment', *J. Magn. Reson.* 1969, vol. 24, no. 1, pp. 71–85, Oct. 1976.
2. A. A. Deshmukh, S. D. Kulkarni, A. P. C. Venkata, and N. V. Phatak, 'Artificial Neural Network Model for Suspended Rectangular Microstrip Antennas', *Procedia Comput. Sci.*, vol. 49, pp. 332–339, 2015.
3. A. A. Deshmukh, M. Shukla, S. Patel, S. Labde, and A. P. C. Venkata, 'Resonance Frequency Estimation for Equilateral Triangular Microstrip Antennas Using Artificial Neural Network Model', in *Proceedings of International Conference on Wireless Communication*, Singapore, 2018, pp. 67–74.
4. A. Rawat, R. N. Yadav, and S. C. Shrivastava, 'Neural network applications in smart antenna arrays: A review', *AEU - Int. J. Electron. Commun.*, vol. 66, no. 11, pp. 903–912, Nov. 2012.
5. J. Mispelter, M. Lupu, A. Briguët, 'NMR Probeheads for Biophysical and Biomedical Experiments'. Imperial College Press ISBN 978-1-84816-662-2; July 2015
6. T. L. Peck, R. L. Magin, and P. C. Lauterbur, 'Design and Analysis of Microcoils for NMR Microscopy', *J. Magn. Reson. B*, vol. 108, no. 2, pp. 114–124, Aug. 1995.
7. H. B. Dwight, 'Proximity effect in wires and thin tubes', *J. Am. Inst. Electr. Eng.*, vol. 42, no. 9, pp. 961–970, Sep. 1923.
8. S. Eroglu, G. Friedman, and R. L. Magin, 'Estimate of losses and signal-to-noise ratio in planar inductive micro-coil detectors used for NMR', *IEEE Trans. Magn.*, vol. 37, no. 4, pp. 2787–2789, Jul. 2001.
9. A. Nabil *et al.*, 'Electrical modelling of tapered TSV including MOS-Field effect and substrate parasitics: Analysis and application', *Microelectron. J.*, vol. 100, p. 104797, Jun. 2020.

# Ultra-Wideband Microstrip Patch Sensor Antenna Embedded into Bra for Comfortable Breast Cancer Microwave Imaging

Abel Rangel-Trejo<sup>1</sup>, José A. Bernardo<sup>1</sup>, L. Konadu<sup>1</sup>, Latifa Fakri-Bouchet<sup>1,2</sup>

<sup>1</sup>Univ Lyon, CNRS, Université Claude Bernard Lyon 1,  
Institut des Sciences Analytiques, UMR 5280, 5 rue de la Doua,  
F-69100 VILLEURBANNE, France, [abel.rangel@cetys.edu.mx](mailto:abel.rangel@cetys.edu.mx)  
<sup>2</sup>INSA Lyon, France, [latifa.fakri-bouchet@insa-lyon.fr](mailto:latifa.fakri-bouchet@insa-lyon.fr)

## Abstract

Microwave Imaging (MWI) Technique for Early Breast Cancer has been studied during the last years with several Microstrip Patch Antennas (MPA) configurations due to their ability to detect the electrical footprint of biological tissues. These antennas had shown advantages concerning the space resolution, portability, effective-cost, flexibility, and easy-fabrication. This study reports an overview about the essential characteristics to consider while designing these Ultra-Wide-Band (UWB) MPA and their variations in the use of Radar configuration for MWI. Our work aims the development of optimal RF sensors working inside the unlicensed spectrum frequencies defined by the Federal Communications Commission (FCC) and European Telecommunications Standards Institute (ETSI). This analysis is done using theoretical formulations about MPA, and data mining from automated antenna simulations using CST Microwave Studio and MATLAB API. This research also includes a comparison between different dielectric substrates, different dimensions, reflection-coefficient, and discussions about gain analysis with manufacturing reproducibility over identical UWB antennas.

**Keywords:** Microstrip Patch antennas, Microwave imaging, Microwave measurement, Radar Imaging, Ultra-Wide-Band, Data mining, Breast-Cancer.

## 1. Introduction

Breast Cancer deaths in 2021 are estimated to be around 43,600 for the USA [1] and more than 93,571 for Europe [2]. Today is known that early diagnosis increases the survival chances among patients, and they require less extensive treatments [3]. Recently the Microwave Imaging (MWI) System has been confirmed by several authors to be one of the most efficient non-invasive, cost-effective, easy-to-use, Breast Cancer detection technique. MWI is reported with an accuracy around 80 – 90 % for Breast Tumor detection compared to other systems like X-ray with 70.2%, MRI with 72.9%, Ultrasound with 67.8% and Clinical examinations with 63.6% of accuracy to detect malignant Tumors [4], [5].

However, to work with these MWI systems in Radar Configuration, a UWB antenna is needed as sensor, a key part of the imaging system. Our work present different UWB Microstrip Patch antenna variations with working frequency shift inside the MW unlicensed spectrum-range as established by the FCC in the USA (3.1-10.6 GHz) and the ETSI in Europe (3.4-8.5 GHz) [6].

The MWI is typically used in two configurations, *Radar* or *Tomography*. Both can create an image from the breast; however, they have different advantages.

- i. The *Radar* is known as a *Qualitative Imaging* (approximative), because doesn't require complicated computation, only weak *a priori* information is needed. It has good spatial resolution and is sensitive to changes of tissue distribution.
- ii. The *Tomography* is a *Quantitative Imaging* (Exact Calculation), which requires complicated computation (forward problem), *a priori* information is usually needed. Tomography has low spatial resolution, and is quantitative only in terms of its ability to calculate the value of dielectric permittivity of the imaged object or tissue [7].

For simplicity, effective cost, and good accuracy, the Radar configuration is more interesting. Its working frequency range requires being UWB to transmit Microwaves in different frequencies that will interact differently with the sample under test or tissues and will have different penetration depths to make the microwave image.

## 2. Materials and Methods

## 2.1. UWB Microstrip Patch Antenna (UWB-MPA) Design

Microstrip Patch Antenna electrically looks bigger than its physical dimensions because of the fringing effects. To avoid this phenomenon, the length of the patch has been extended on each side by  $\Delta L$ , Fig. 1.

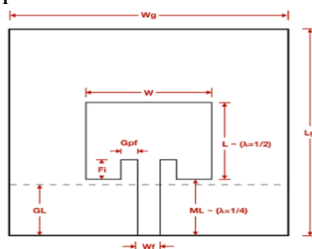


**Figure 1** : Diagram of Microstrip Patch Antenna [8]

$\Delta L$  is in function of the effective dielectric constant  $\epsilon_{eff}$  and the width-to-height ratio ( $W/h$ ). Then the effective length of the patch is given by equation (1), where ( $L$ ) is given by equation (2).

$$L_{eff} = L + 2\Delta L \quad (1)$$

$$L = \lambda / 2 \quad (2)$$

Another way to avoid the fringing effects, one can use an effective dielectric constant ( $\epsilon_{eff}$ ), and the ( $L_{eff}$ ) to calculate the real ( $L$ ) length with the real dimensions [8]. First is required to specify ( $\epsilon_r$ ) substrate dielectric constant, ( $f_r$ ) resonance frequency in Hz (or  $f_c = \text{central frequency in our case of UWB}$ ), and ( $h$  or  $SH$ ) thickness of the substrate. Then it is possible to determine the following elements using the design procedure described in Fig. 1 and the equations numbered from (3) to (13). The Microstrip Patch Antenna dimensions and characteristics are: ( $W$ ) Width of the patch, ( $\epsilon_{eff}$ ) Effective dielectric constant, ( $\Delta L$ ) Length difference, ( $L_{eff}$ ) Effective length, ( $L$ ) Length of the patch, ( $Fi$ ) Feeding inset, ( $Gpf$ ) Gap patch-feedline, ( $ML$ ) Microstrip-feedline length, ( $Wg$ ) Substrate width, ( $Lg$ ) Substrate length, ( $GL$ ) Ground length, and ( $Wf$ ) Width of feed.

The design procedure is done by resolving the following formulas in the presented order.

$$W = \frac{c}{2f_r \sqrt{\frac{\epsilon_r + 1}{2}}} \quad (3)$$

$$\epsilon_{eff} = \frac{\epsilon_r + 1}{2} + \frac{1 - \epsilon_r}{2} \left(1 + 12 \frac{h}{W}\right)^{-1/2} \quad (4)$$

$$\Delta L = 0.412h \frac{(\epsilon_{eff} + 0.3) \left(\frac{W}{h} + 0.264\right)}{(\epsilon_{eff} - 0.258) \left(\frac{W}{h} + 0.8\right)} \quad (5)$$

$$L_{eff} = \frac{c}{2f_r \sqrt{\epsilon_{eff}}} \quad (6)$$

$$L = L_{eff} - 2\Delta L \quad (7)$$

$$Lg = 2 \times L \quad (8)$$

$$Wg = 2 \times W \quad (9)$$

$$Fi = \frac{(6h)}{2} \quad (10)$$

$$Gpf \approx 0.25 < Gpf < 1 \quad (11)$$

$$ML = W \quad (12)$$

$$GL = Lg \quad (13)$$

Where  $c$  is the free-space velocity of light,  $Gpf$  is usually 1 mm,  $Wf$  is found using a matching simulator to have  $50\Omega$  of input impedance transmission line (like CST impedance matching assistant),  $f_r$  is the frequency of resonance and all the other determined values are specific distance-constraints for the microstrip patch antenna (Fig. 1) [8], [9].

## 2.2. Antenna Fabrication and Characterization setup

The designs and simulations of these antennas were done using CST Microwave Studio, after considering the previous formulas. Our specific working frequency was defined ranging from 3.4 GHz to 4.5 GHz because of the overlapping Unlicensed Frequencies (3.4 GHz - 8.5 GHz) & our Vector Network Analyzer (VNA) measurable frequency range (200 MHz – 4.5 GHz).

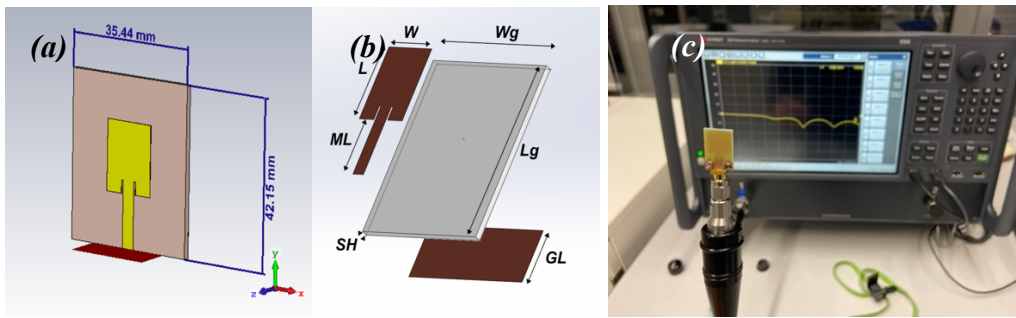


**Figure 2** – (a) Generic Microstrip Patch Antenna CST Simulation, (b) SolidWorks Exploded view, (c) specific UWB for our application of Early Breast Cancer Detection.

This study includes the simulation of generic UWB-MPA parametric analysis to understand the overall behaviors of these kind of antennas (Fig. 2). For all our UWB-MPA antennas, we selected the substrate FR-4 with dielectric constant of 4.3, thickness of 1.6 mm, and double 35  $\mu\text{m}$  layer of copper.

### 3. Results: Generic UWB-MPA Characterization and Parametric Analysis

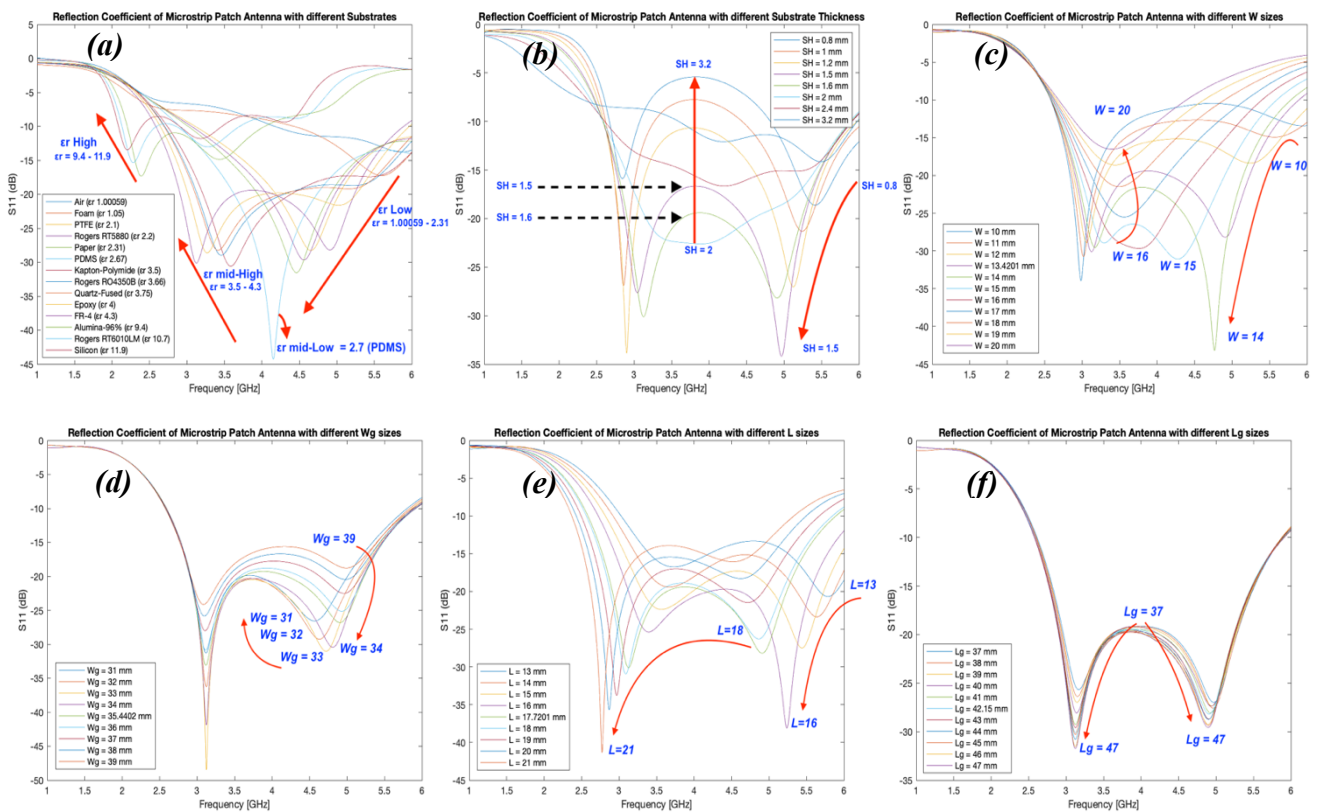


**Figure 3** – UWB MPA Parametric frequential analysis: (a) substrates dielectric constant, (b) substrate thickness, (c) width of patch, (d) width of substrate, (e) length of patch, (f) length of substrate.

Various UWB MPA antennas were simulated using CST MW Studio. Their behavior was recorded and analyzed by changing individually each of their following parameters ( $SH$ ), ( $ML$ ), ( $W$ ), ( $Wg$ ), ( $L$ ), and ( $Lg$ ). An identified tradeoff exists between the dielectric constant and the thickness of the substrate, (Fig. 3 (a) & (b)). The desired substrate for larger bandwidth is with lower ( $\epsilon_r$ ) and higher thickness, but at expense of bigger size [8]. The metal layer thickness did not show any significant impact in the Microstrip Patch antenna resonance. Wider patches ( $W$ ) resulted in a bigger bandwidth.

However, the dimensions of the other parameters need to be optimized at the same time than ( $W$ ) changes to avoid resonance loss. For UWB antennas, less wide ( $Wg$ ), substrates (Fig. 3 (d)) were better, as they increase the

resonance of the antenna with minimal bandwidth reduction. The length of the patch is usually known as  $L=\lambda/2$ , but for UWB this can be taken as the  $f_c$  (central frequency) of the bandwidth. A common sense is to increase ( $L$ ) for lower frequencies, or lower ( $L$ ) for higher ones (Fig. 3 (e)). For the parameter Substrate length ( $L_g$ ), more it is increased more it increases the efficiency of the transmit power (Fig. 3 (f)).

#### 4. Conclusion

In this paper, we have presented the design and parametric analysis of a generic UWB Microstrip Patch Antenna in free space medium conditions with the objective to diagnose early breast cancer. The proposed antenna is relatively small with the size of  $12 \times 18 \times 1.6 \text{ mm}^3$ . The calculated return loss coefficients show that this antenna has a good ability to detect tumors inside the breast using a working multi-frequency range. The future work is to adapt this behavior of UWB antennas to keep a working frequency inside the 1 GHz to 4.5 GHz interval (range of our VNA), and inside 3.4 GHz to 8.5 GHz (the unlicensed range of Europe and USA), with enhancements of gain, radiation efficiency and specific absorption rate, for authorized clinical trials tests.

#### Acknowledgements

Thanks to CONACYT Mexico for the sponsorship. Thanks to the ISA's teams, especially to Catherine Jose, Stephan Dupont and Christophe Pages for their time and experience.

#### References

1. (2021, April 02). "U.S. Breast Cancer Statistics," [Online], Available: [https://www.breastcancer.org/symptoms/understand\\_bc/statistics](https://www.breastcancer.org/symptoms/understand_bc/statistics)
2. G. Carioli, M. Malvezzi, *et al.*, "Trends and predictions to 2020 in breast cancer mortality in Europe," *The Breast*, vol. 36, pp. 89–95, 2017.
3. A. Migowski, "A detecção precoce do câncer de mama e a interpretação dos resultados de estudos de sobrevida," *Ciência & Saúde Coletiva*, vol. 20, no. 4, pp. 1309–1309, 2015.
4. L. Wang, "Microwave Sensors for Breast Cancer Detection," *Sensors*, vol. 18, no. 2, pp. 655, 2018.
5. A. Rahman, *et al.*, "Electromagnetic Performances Analysis of an Ultra-wideband and Flexible Material Antenna in Microwave Breast Imaging: To Implement a Wearable Medical Bra," *Scientific Reports*, vol. 6, no. 1, pp. 1–11, 2016.
6. A.-D. Capobianco *et al.*, "Directive Ultra-Wideband Planar Antennas," in *Microwave and Millimeter Wave Technologies Modern UWB antennas and equipment*, I. Minin, Ed. InTech, 2010.
7. Bolomey Jean-Charles, "Qualitative versus Quantitative approaches to Microwave-Based imaging techniques for Medical Applications," in *Theories and Numerics on Inverse Problems*, Institute for Mathematical Sciences National University of Singapore, vol. 1, pp. 52, 2018.
8. C. A. Balanis, *Antenna theory: analysis and design*, 3. ed. Hoboken, NJ: Wiley-Interscience, 2005.
9. L. Agyemang Konadu, "Development of new microstrip Antenna for early Breast Cancer Detection," Master dissertation, Dept. Physics, Université de Lyon, 2018.

# Validation of Data from an Artificial Sniffer Dog by Common Analytical Techniques

Iona Hardy<sup>1</sup>, Mogens Havsteen Jakobsen<sup>2</sup>, Tuule Treiberg<sup>2</sup>, Charlotte Held Gotfredsen<sup>2</sup>, Eleftheria Dossi<sup>1</sup>  
<sup>1</sup>Cranfield University

Centre for Defence Chemistry, Defence Academy of the United Kingdom, Shrivenham, SN6 8LA, United Kingdom, [i.r.hardy@cranfield.ac.uk](mailto:i.r.hardy@cranfield.ac.uk), [e.dossi@cranfield.ac.uk](mailto:e.dossi@cranfield.ac.uk)

<sup>2</sup>Technical University of Denmark

Department of Chemistry, Kemitorvet, Building 207, DK-2800 Kgs. Lyngby, Denmark, [mhja@kemi.dtu.dk](mailto:mhja@kemi.dtu.dk), [tuutr@kemi.dtu.dk](mailto:tuutr@kemi.dtu.dk), [chg@kemi.dtu.dk](mailto:chg@kemi.dtu.dk)

## Abstract

CRIM-TRACK, an artificial sniffer dog, employs a colourimetric sensor system to monitor the colour change of chromic dyes when in contact with the vapours of illicit molecules (analytes) for detection and identification of substances. Within, the interaction of illicit chemicals and chromic dyes have been studied in solution using Proton Nuclear Magnetic Resonance (<sup>1</sup>H NMR) spectroscopy and Ultraviolet-Visible (UV-Vis) spectrophotometry, to validate data generated from detection experiments using CRIM-TRACK sniffer. <sup>1</sup>H-NMR revealed the colour change mechanism induced by benzyl methyl ketone (BMK), a precursor chemical of methamphetamines, was hydrogen bonding between the BMK and specific dye molecules. It also revealed that hexamine (HEX), an explosives precursor, induced a colour change by formation of ion pairs with the specific dye molecules. The colour changes detected by CRIM-TRACK were confirmed by UV-Vis where a shift in absorption wavelength and/or a change in absorbance occurred.

**Keywords:** chemical precursors, detection, colourimetric sensor, CRIM-TRACK sniffer system, NMR, UV-Vis

## 1. Introduction

The manufacture, trafficking, selling and use of illicit drugs, explosives and their chemical precursors are controlled internationally to try and reduce their socio-economic impact on society. Examples of these impacts include the €30 billion a year European Union illicit drug market [1], and the Manchester Arena bombing that killed 22 [2]. To minimise the impact of these substances, instrumental techniques such as ion mobility spectroscopy, and trained dogs are the main methods currently employed by law enforcement agencies to detect explosive and illicit drug materials [3].

A complimentary detection device, the CRIM-TRACK sniffer device, is currently in development [4], [5]. This device utilises a colourimetric sensor system to detect and identify illicit substance by monitoring and analysing colour change of chromic dyes printed on a chip during contact with the substance's (analyte's) vapour. Data obtained using the CRIM-TRACK sniffer device with the analytes benzyl methyl ketone (BMK), a methamphetamine precursor and controlled chemical, and hexamine (HEX), an explosives chemical precursor. It reported that 4-methoxy-4'-hydroxyazobenzene (DAB4) and bromocresol green (SP6) dyes respond – change colour – to BMK and HEX, whilst 1-hydroxyanthraquinone (AQ2) does not.

Validation of sniffer results was performed by characterising selected dyes from the chip and analytes in solution using NMR spectroscopy and UV-Vis spectrophotometry, then characterising analyte:dye mixtures at different ratios, and comparing the mixtures' data to the single components'. NMR spectroscopy revealed structure changes and UV-Vis to colour changes through wavelength and absorbance variations of the analyte:dye mixtures. This allows investigation into the analyte-dye interactions and confirmation of colour changes detected by CRIM-TRACK sniffer, something that has not been previously investigated by other research groups who also study colourimetric sensor systems using chromic dyes for detection purposes [6].

## 2. Experimental

### 2.1 Materials

4-Methoxy-4'-hydroxyazobenzene (97% purity, DAB4) was synthesised in house at Cranfield University [7]. Bromocresol green (95%, SP6) benzyl methyl ketone (99%, (BMK)) and hexamine (99%, HEX) were obtained from Sigma-Aldrich, 1-hydroxyanthraquinone (>95%, AQ2) from Tokyo Chemical Industry, Ltd. Chloroform (CHCl<sub>3</sub>) (stabilised with 0.6% ethanol) and deuterated chloroform (CDCl<sub>3</sub>) (with molecular sieves; D, 99.8% and 0.025% v/v tetramethylsilane (TMS)) were obtained from Sigma-Aldrich and Cambridge Isotope Laboratories, Inc respectively. All commercially sourced chemicals were used as provided.

### 2.2 Methods

<sup>1</sup>H NMR spectra were recorded on a Bruker Ascend 400 MHz spectrometer in CDCl<sub>3</sub>, with TMS as reference, at ambient temperature for 32 scans. 2 mM dye and 0.25 M analyte solutions in CDCl<sub>3</sub> were freshly prepared before the experiments. 750 µl dye solution was placed in a standard 5 mm NMR tube and the spectra recorded. 6-300 µl aliquots of the analyte solution were then added, and the NMR spectra recorded at 1:1, 5:1, 10:1, 50:1 and 100:1 mol/mol analyte:dye ratios. Processing and analysis of data was carried out using Bruker's TopSpin software.

UV-vis spectra were recorded using a Cary 50 & Thermo Scientific Evolution 220 UV-VIS spectrophotometer and a far UV silica cuvette with 10 mm path length at room temperature. 0.025 mM and 0.05 mM 2 mM dye solutions and 2.5 mM and 5 mM analyte solutions in CHCl<sub>3</sub> were freshly prepared before the experiments.

Mixtures at 50:1, 100:1, 150:1 and 200:1 mol/mol analyte:dye ratios were prepared using the 0.05 mM dye and 5 mM analyte solutions. The 0.025 mM dye and 2.5 mM analyte solutions were recorded to provide the curves of the single components for the creation of a predicted 100:1 curve. These are the same concentrations that are present in 100:1 mixture. The predicted 100:1 is the sum of these curves, assuming additive behaviour. All UV spectra were recorded in triplicates and the data averaged.

## 3. Results & Discussion

BMK and HEX were chosen as analytes as they have ketone and amine functional groups respectively, so were expected to potentially interact differently with the dyes. They are common chemical precursors for the manufacturing of methamphetamine and explosives respectively. DAB4, SP6 were chosen to represent two different families of responsive dyes on the CRIMTRACK microchip (colour changing) while AQ2 dye was chosen as negative non-responsive dye on the microchip. The chemical structures of these chemicals are shown in Figure 1.

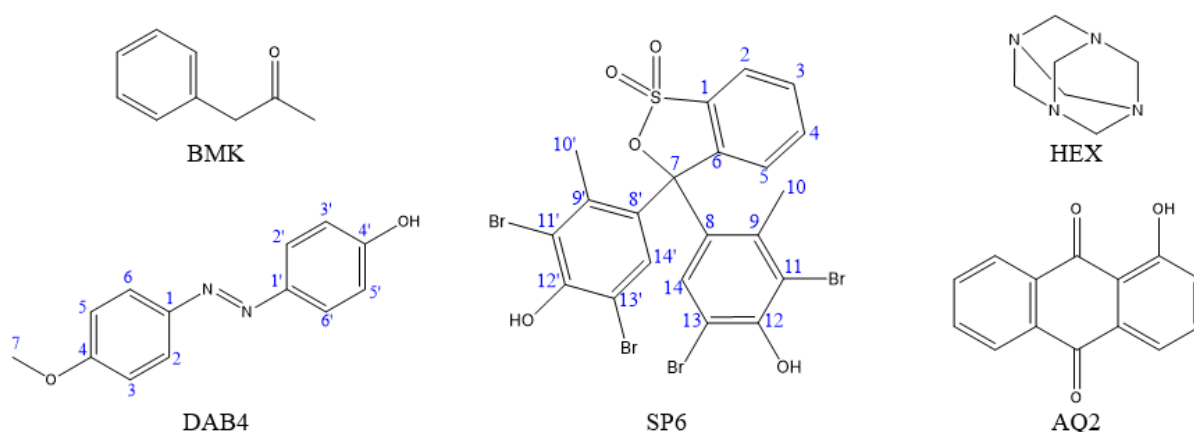


**Figure 1:** Structures of analytes (BMK and HEX) and dyes (DAB4, SP6 and AQ2) with carbons numbered for DAB4 and SP6

### 3.1 BMK: Dye Interactions

During preparation of NMR mixture samples, no visible colour change was observed. The dye solutions remained same the pale yellows on addition of BMK. No formation of a new product is seen in the NMR spectra of the BMK:dye mixtures, nor any changes in the chemical shift of the BMK peaks. Downfield shift of the hydroxyl peaks of DAB4 and SP6 by 0.01 ppm at 1:1 BMK:dye ratio was discerned which increased in magnitude with increase in the ratio of BMK (+0.6 ppm and +0.4 ppm at 100:1 respectively). No effect on the chemical shifts of AQ2's protons was seen at any ratio, confirming AQ2's assignment as a non-responsive dye from the sniffing data.

No visible colour change was observed during the preparation of the UV-Vis mixture samples. Non-additive behaviour was indicated in both DAB4 and SP6 mixtures as the experimental 100:1 and predicted 100:1 curves did not align - there was a hyperchromic shift (to greater absorbance). Additive behaviour was however observed with AQ2. Isosbestic points (where curves of mixtures at different ratios cross, Table 1) in all BMK:dye mixtures confirms that only the single components are present in the solution, and that there is not a third covalently formed product. There was no shift in  $\lambda_{\max}$  of DAB4 or AQ2, but for SP6 there was a hypsochromic shift (to shorter wavelength) by 3 nm.

The NMR and UV-Vis data combined indicates weak electrostatic interactions between BMK and DAB4, and BMK and SP6 in solution. After consideration of the structures (Figure 1), it is believed that there is weak, non-covalent and reversible hydrogen bonding interaction between hydroxyl groups of dyes and ketone of BMK. This would account for the deshielding of the hydroxyl protons. This does not occur with AQ2 as it has a stronger, intramolecular hydrogen bond in place already between the ketone and adjacent hydroxyl group (Figure 1).

	Wavelength, $\lambda$ (nm)								
	DAB4	BMK:DAB4	HEX:DAB4	SP6	BMK:SP6	HEX:SP6	AQ2	BMK:AQ2	HEX:AQ2
$\lambda_{\max}$	357	357	357	412	409	415	406	406	406
Isosbestic point		308	245		318	252		317	241

Table 1: UV-Vis Spectrophotometry Data

### 3.2 HEX: Dye Interactions

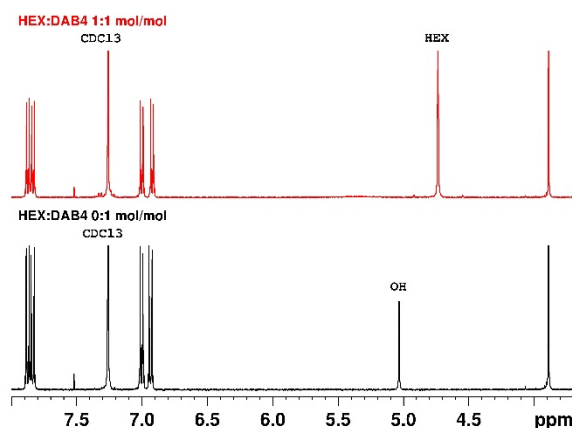
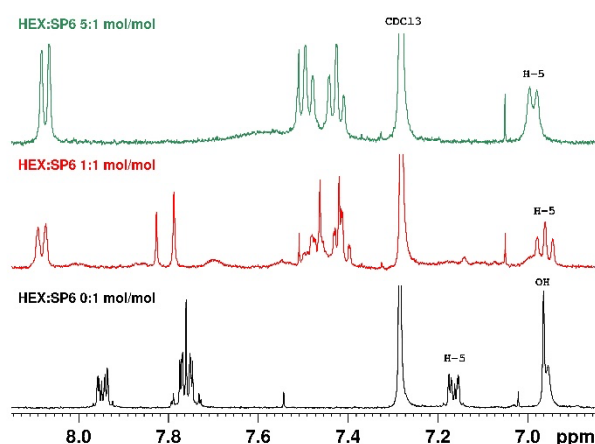


Figure 2:  $^1\text{H-NMR}$  ( $\text{CDCl}_3$ , 400 MHz) spectra of HEX:DAB4 0:1 (black line, bottom) and 1:1 (red line, top).



**Figure 3:** Aromatic region of  $^1\text{H-NMR}$  ( $\text{CDCl}_3$ , 400 MHz) spectra of HEX:SP6 0:1 (black line, bottom), 1:1 (red line, middle) and 5:1 (green line, top).

The pale yellow SP6 chloroformic solution became a bright yellow mixture upon addition of HEX, but no colour changes of DAB4 and AQ2 mixtures were visible by eye. As in the BMK:dye mixtures, the NMR data illustrated that there was no formation of a new product and no changes to the chemical shift of the analyte, HEX. On addition of HEX to DAB4 from 1:1 and SP6 from 2:1 onwards, the hydroxyl proton peaks' intensity decreases to 0. In DAB4, a minor upfield shift ( $-0.01$  ppm) of the chemical shifts of aromatic protons attached to carbon atoms 3' and 5' is observed (Figure 2), determined to be due to greater inductive effect by  $\text{O}^-$  than OH, caused by deprotonation by HEX. The chemical structure of SP6 changes on addition of HEX – the sulphonate ring opens. This is clearly indicated by the additional peaks and changes in the chemical shifts and multiplicities of the aromatic peaks at 1:1 and 5:1 ratios (Figure 3). In the same manner of BMK:AQ2, no effect on the chemical shifts of AQ2's protons was seen at any ratio.

The same colour change of pale yellow to bright yellow was observed during the preparation of the HEX:SP6 mixtures for UV-Vis as was observed during the NMR experiments. As with the BMK:dye mixtures, HEX:DAB4 and HEX:SP6 indicated non-additive behaviour due to hyperchromic shift, and HEX:AQ2 displayed additive behaviour. Isosbestic points (Table 1) in all HEX:dye mixtures confirms that only the HEX and dye are present in the solution and that there is not a third product. Once more, there was no shift in  $\lambda_{\text{max}}$  of DAB4 or AQ2, but for SP6 there was a bathochromic shift (to longer wavelength) by 3 nm.

The observations gained from NMR and UV-Vis together indicates that chemical interaction, in solution, occurs between HEX and DAB4 and HEX and SP6, but not between HEX and AQ2. It is believed that there is strong, non-covalent, irreversible ion-pair formation by deprotonation of the hydroxyl protons which cannot occur with AQ2 due to its strong, intramolecular hydrogen bonding.

#### 4. Conclusions

The interactions of analytes, benzyl methyl ketone (BMK) and hexamine (HEX) with three dyes, 4-methoxy-4'-hydroxyazobenzene (DAB4), bromocresol green (SP6) and 1-hydroxyanthraquinone (AQ2) were investigated in chloroformic solutions. Proton NMR spectroscopy of the mixtures determined the detection mechanism of BMK to be hydrogen bonding and the detection mechanism of HEX to be ion-pair formation by deprotonation when using DAB4 and SP6 dyes. UV-Vis spectrophotometry of the mixtures recorded colour changes not seen by eye and determined cause of colour change: change in absorption amount and/or change of wavelength absorbed. BMK did not induce a visible colour change in the dyes but had a slight increase in absorption whereas HEX had both, changing from pale yellow to bright yellow at a different wavelength in solution. This has validated data from CRIM-TRACK sniffer experiments that reported that DAB4 and SP6 dyes responded to BMK and HEX, whilst AQ2 did not.

## 5. Future Work

Using the methodologies laid out in these proceedings, it is planned to analyse the interactions of other illicit substances such as methamphetamine hydrochloride, cocaine, and precursor chemicals with responding chromic dyes to further validate sniffer data.

## Acknowledgements

This PhD research is funded by Cranfield University in memory of Dr Mike Gibson. Thanks are given to, Deena Francis, Tommy Sonne Alstrøm and Milan Laustsen at the Danish Technical University and Crim-Track Aps for providing the sniffer data this research is based on and assisting in its evaluation.

## References

1. European Monitoring Centre for Drugs and Drug Addiction and Europol, 'EU Drug Markets Report 2019', Publications Office of the European Union, Luxembourg, 2019. doi: 10.2810/796253.
2. D. De Simone, 'The road to the Manchester Arena bombing', *BBC News*, Mar. 17, 2020.
3. R. Bogue, 'Detecting explosives and chemical weapons: a review of recent developments', *Sens. Rev.*, vol. 35, no. 3, pp. 237–243, Jun. 2015, doi: 10.1108/SR-12-2014-0754.
4. J. K. Munk *et al.*, 'CRIM-TRACK: sensor system for detection of criminal chemical substances', *Opt. Photonics Counterterrorism, Crime Fight. Def. XI; Opt. Mater. Biomater. Secur. Def. Syst. Technol. XII*, vol. 9652, no. October 2015, p. 965208, 2015, doi: 10.1117/12.2194915.
5. L. L. Mølgaard *et al.*, 'Improved detection of chemical substances from colorimetric sensor data using probabilistic machine learning', *Chem. Biol. Radiol. Nucl. Explos. Sens. XVIII*, vol. 10183, no. May 2017, p. 1018307, 2017, doi: 10.1117/12.2262468.
6. Z. Li and K. S. Suslick, 'The Optoelectronic Nose', *Acc. Chem. Res.*, vol. 54, no. 4, pp. 950–960, Feb. 2021, doi: 10.1021/acs.accounts.0c00671.
7. C. Frenz, A. Fuchs, H. W. Schmidt, U. Theissen, and D. Haarer, 'Diblock copolymers with azobenzene side-groups and polystyrene matrix: Synthesis, characterization and photoaddressing', *Macromol. Chem. Phys.*, vol. 205, no. 9, pp. 1246–1258, 2004, doi: 10.1002/macp.200400046.

# Metal nanoparticles decorated graphene for the development of resistive gas sensors dedicated to sulphur-containing pollutants

E. Ruiz<sup>1</sup>, T. Gueye<sup>1</sup>, C. Varenne<sup>1</sup>, A. Ndiaye<sup>1</sup>, J. Brunet<sup>1</sup>, A. Pauly<sup>1</sup>

<sup>1</sup>Université Clermont Auvergne, Clermont Auvergne INP, CNRS, Institut Pascal, F-63000 Clermont-Ferrand, France, [elisa.ruiz@uca.fr](mailto:elisa.ruiz@uca.fr)

## Abstract

In this study, we aim to develop graphene-based resistive gas sensors decorated with nanoparticles for the detection of sulfur containing pollutants. In this paper we prepared reduced graphene oxide (RGO) by chemical reduction of graphene oxide (GO) using a reducing agent. We achieved an efficient decoration of the RGO with metallic nanoparticles (NPs) such as Cu, Pd by chemical route and physical route through thermal evaporation. The decorated material (RGO/NPs) is deposited by drop casting on interdigitated electrodes and used as resistive sensors. After the morphological and electrical characterization of these layers, we discuss the sensing performance of the RGO/NPs under H<sub>2</sub>S. The sensing behavior of the RGO under H<sub>2</sub>S exposition at room temperature and high temperatures is discussed and a specific behavior related to n-p transition is highlighted.

**Keywords:** graphene oxide, graphene, gas sensors, H<sub>2</sub>S, reduced graphene oxide, resistive sensors, metal decoration

## 1. Introduction

Hydrogen sulfide (H<sub>2</sub>S) is a pollutant that affects health and environment. It is considered as toxic gas, and fatal if inhaled at higher concentrations. H<sub>2</sub>S is emitted by several sources as industrial processes and decomposition of organic matter, the effects on human body go from a pungent odor, irritation of eyes and breathing system, impairment of nervous system to death [1]. This gas is regulated in occupational environment, for example in France the exposure limit value for H<sub>2</sub>S on a short period (15 minutes) is 10 ppm [2]. So for all these reasons, its control and monitoring in air quality for safety and health is necessary. The sensing material chosen for our sensors is based on graphene and its derivatives. Graphene is a two dimensional material, is a one-atom-thick layer of carbon atoms. It's used in gas sensors applications for its large surface area available for interaction with gaseous species and for its electrical properties especially in resistive gas sensors [3]. However, its applications are limited because of its zero band gap [4]. One solution is to oxidize the graphene to open or tune the gap [5], [6]. Thus, the generation of oxygenated groups through oxidation allows to create active sites for our resistive gas sensors. But depending on the oxidation level, GO can become too resistive, and less interesting for our purpose. For this reason, reduction processes are used to limit the oxidation rate. This reduction process works as the removal of a part of the oxygen containing functional groups, producing a less resistive material. Due to its defects and functional groups, RGO, is a good candidate for gas sensing applications. The decoration by metallic nanoparticles is widely used for the improvement of the sensitivity and will allow to target toxic gases such as H<sub>2</sub>S [7]. Furthermore, by creating specific interactions with these gases the decoration seems to be a key point to solve the sensor selectivity problem inherent to all sensors. In this study, the RGO is prepared by chemical route and decorated by two methods, chemically and physically. After the morphological and electrical characterization, the sensing materials are deposited on resistive transducers and exposed to H<sub>2</sub>S.

## 2. Materials and methods

### 2.1. Preparation of RGO and metallic decoration

In this work, GO flakes are chemically reduced with sodium citrate to produce RGO used as sensing material. 175mg of GO are firstly dispersed in water (150ml) and ethanol (30ml) and homogenized by

alternating heating and ultrasonic treatment to ensure a better dispersion. Then the reducing agent is added (1.6g sodium citrate in 15ml of water) to the dispersion which is maintained at 80°C under stirring. The resulting mixture is then filtered, washed and dried. The decoration was achieved in two ways: chemically and physically. The chemical decoration consists in reduction of metal ions using NaBH<sub>4</sub> on the RGO. And the second was achieved by thermal evaporation of metals generating NPs on the RGO.

To test sensing materials towards H<sub>2</sub>S, the RGO/NPs obtained chemically and physically are then deposited by drop casting on interdigitated electrodes. The resulting resistive sensors are then exposed to H<sub>2</sub>S at different concentrations and temperatures.

## 2.2. SEM and TEM characterization

In order to morphologically characterize the RGO and the decorations, scanning electron microscopy and transmission electron microscopy (SEM and TEM) analysis was carried out and represented in the figure 1.

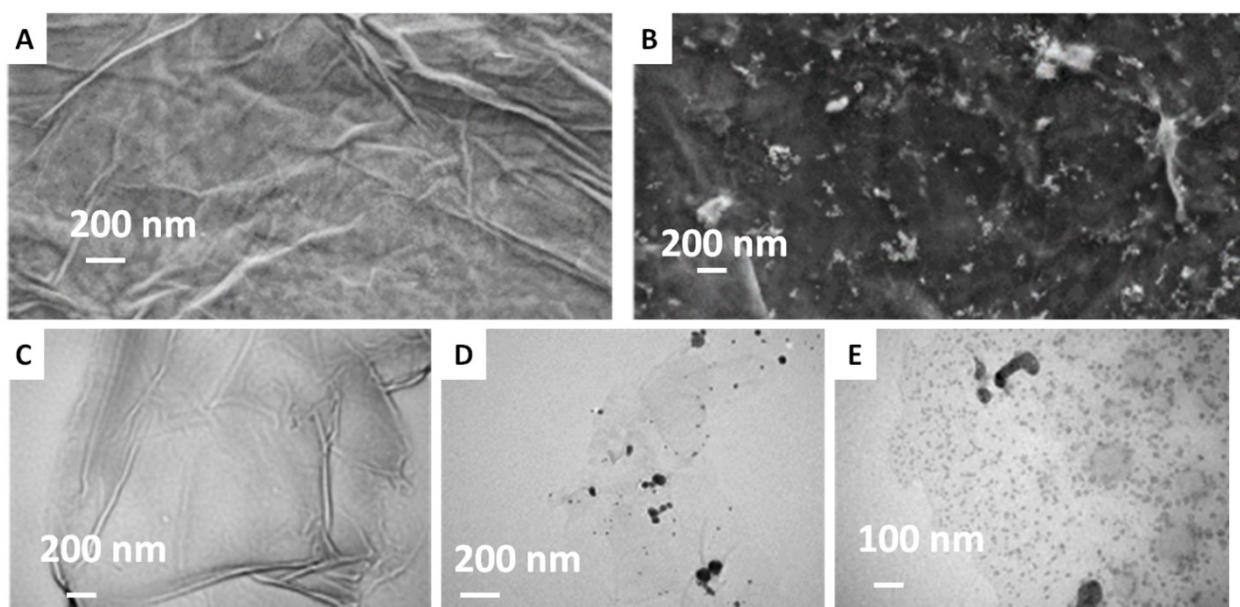


**Figure 1:** SEM images of RGO (A) and chemically decorated RGO/Cu (B); TEM images of RGO (C), chemically decorated RGO/Pd (D) and physically decorated RGO/Pd (E).

We observed graphene sheets which naturally present some ripples as in many graphene materials (figure 1A and 1C). Examples of SEM and TEM images showing the achievement of physical decoration of RGO are presented in figure 1E while those concerning the chemical decoration presented in Figure 1B and 1D. Apart from the ripples that are naturally occurring in graphene, we can identify in the images dots representing the nanoparticles decorated on the RGO matrix. Both physical and chemical decoration seem to highlight the decoration efficiency. The physical method presenting the more homogeneous distribution (figure 1E) than the chemical one (figure 1B and 1D) showing more aggregates.

## 2.3. Electrical characterization

The Current-voltage (I-V) characteristics were carried out before sensing performances studies. It is clear from the obtained curves shown in figure 2 that whatever the decoration method (chemical and physical), the sensing layers present ohmic behavior.

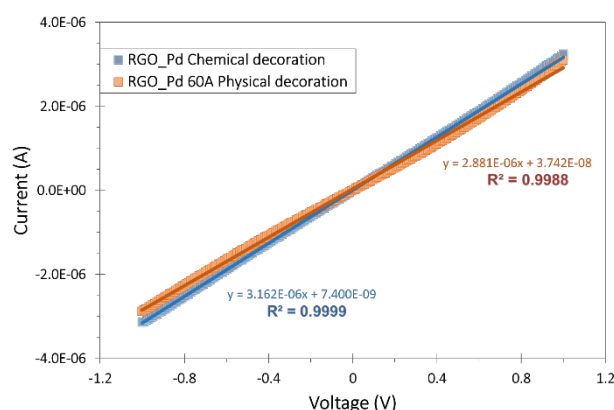


**Figure 2:** I-V characterization of RGO chemically (blue) and physically (orange) decorated with Pd.

This ohmic behavior is also attested by the linearity and the  $R^2$  values and validates their use as resistive sensors. The figure 2 represents the case of Pd decoration, however decoration by other metals present also similar behavior.

### 3. Sensors responses to $H_2S$ exposure

#### 3.1. Sensors responses of chemically decorated RGO

The curves in Figure 3a and 3c represent the sensor responses of the RGO and chemically decorated RGO/Cu at  $100^\circ C$  towards  $H_2S$  in the range 50 ppm to 90 ppm. The RGO alone in Figure 3a shows a decreasing resistance under  $H_2S$ , indicating an n-type behavior. Indeed,  $H_2S$  is a reducing gas, such a resistance decrease results from an electron charge transfer from the gas to the layer. In the same way, the chemically decorated RGO/Cu in figure 3c presents also a decreasing resistance indicating a n-type behavior. In this case, of RGO, we also observed a continuous decrease of the resistance base line, that can be associated to the additional reduction of the matrix by the temperature [8]. The calibration curves (plotted as  $\Delta R/R_0 = (R_{Gas}-R_0)/R_0$ ) represented in figure 3e allow to compare the two sensitivities. We note that the RGO/Cu shows a better sensitivity. In fact, we estimated from the calibration curves a sensitivity of 0.036%/ppm for RGO/Cu against 0.018% for RGO.

#### 3.2. Sensors responses of RGO with physical decoration

The sensor response of physically decorated RGO (RGO/Pd) towards  $H_2S$  in the range 30 ppm to 90 ppm at room temperature is represented on the Figure 3d. The RGO response after a thermal treatment in figure 3b, shows a decreasing resistance under  $H_2S$  indicating an n-type behavior. The RGO/Pd follows the same tendency corresponding to an n-type behavior. The calibration curves in Figure 3f, allow to compare the two sensitivities at room temperature. Here again, at room temperature, the RGO decorated with palladium shows a better sensitivity than the RGO alone with a sensitivity of 0.056%/ppm for the decorated RGO/Pd against 0.040%/ppm for the RGO.

These results show the efficiency of the two decoration methods on the improvement of the sensitivity. The physical method because of its room temperature responsiveness and its higher sensitivity seems to be the best method. However, further investigations of these two methods with other metals need to be undertaken to conclude in the efficiency of one method over the other.

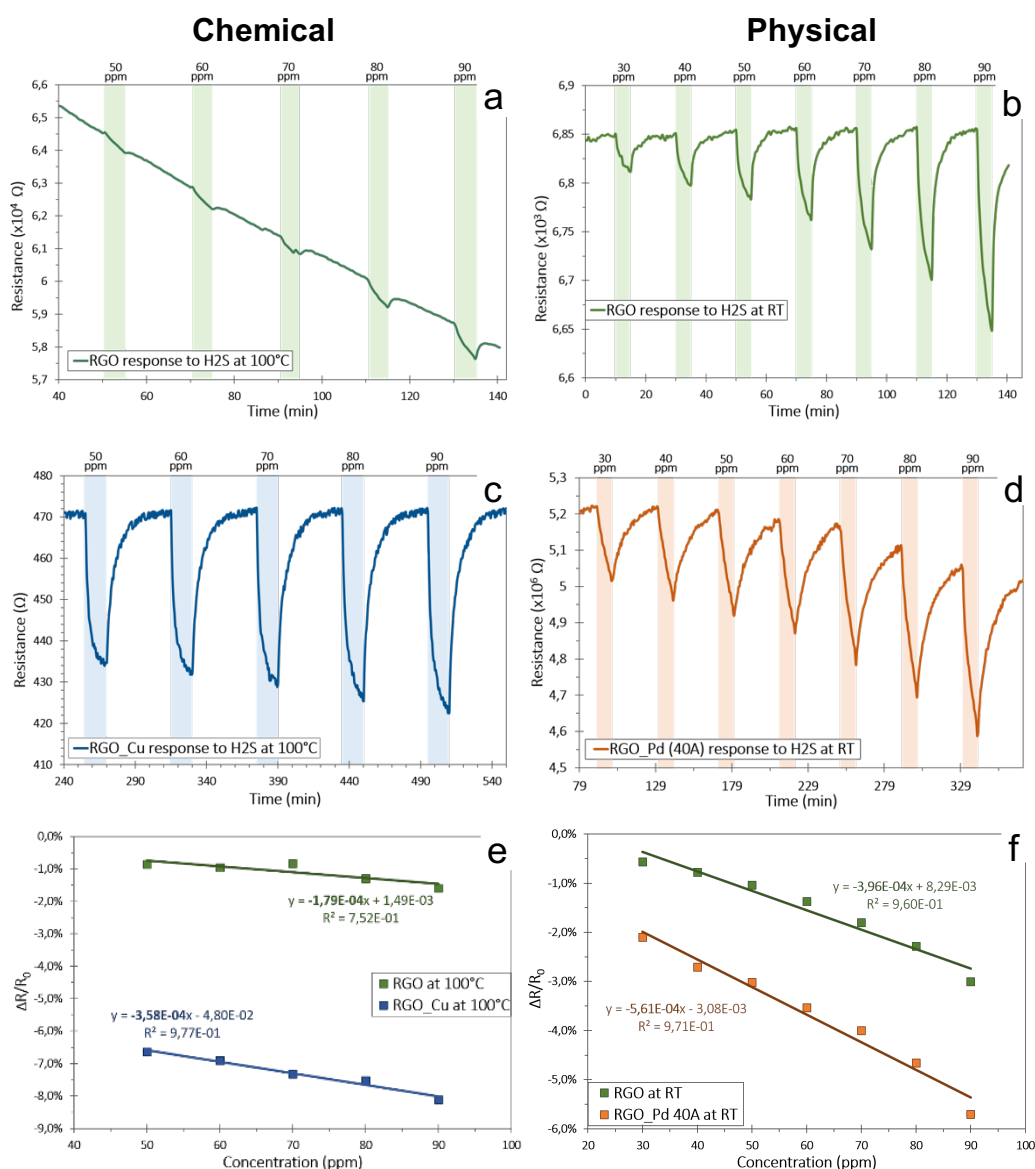


**Figure 3:** Sensor responses of the chemical and physical decoration of the RGO. Sensor response at 100°C a) and RT b) of the RGO non-decorated, sensor response at 100°C of the chemical decoration with Cu c), sensor response at room temperature of the physical decoration with 40Å of Pd d). calibration curves at 100°C e) and RT f).

### 3.3. Sensor responses of non-decorated reduced graphene oxide

The last results to discuss is the behavior of RGO alone, exposed to H<sub>2</sub>S at room temperature, before and after thermal treatment (100°C). The sensor responses represent the variation of the resistance with time for RGO before and after thermal treatment. The responses as presented in figure 4a, show a p to n type transition due to the thermal treatment. In fact, the sensor response of RGO without thermal treatment shows an increase in resistance under H<sub>2</sub>S, indicating a p-type behavior, while after thermal treatment, the resistance of the matrix decreases, showing a n-type. This phenomenon indicating a change of the RGO type doping behavior is caused by the temperature. We presume that this behavior can be attributed to reduction process and is caused by the remaining oxygenated groups. We also note a loss in sensitivity after the transition (Figure 4b) and this could be explained by the additional reduction of the matrix by the temperature, thus reducing the rate of active sites. Studies are currently under investigation to explain the origin of this intriguing behavior.

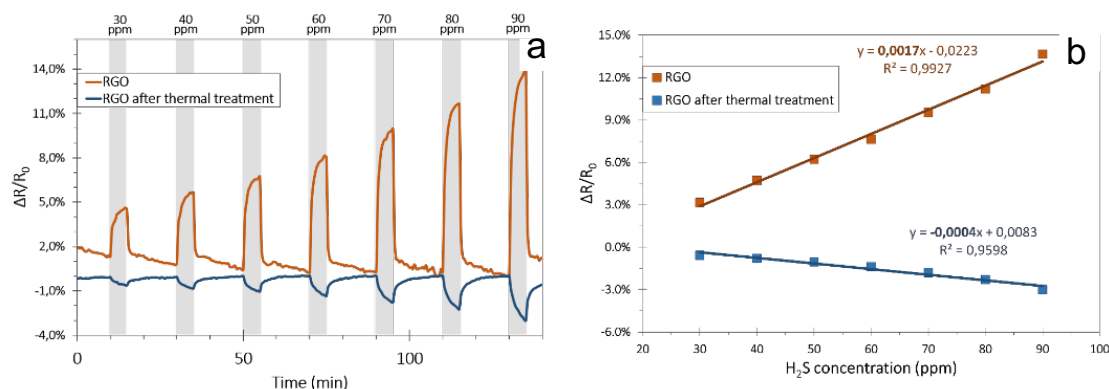


**Figure 4:** a) Sensor response at room temperature towards  $H_2S$  at 30 ppm to 90 ppm, of RGO before (orange) and after thermal treatment (blue). b) calibration curves of the corresponding response.

#### 4. Conclusion

We prepared reduced graphene oxide by chemical route and decorated it by metal nanoparticles chemically with reducing agent, and physically by thermal evaporation. We achieved an efficient decoration both chemically with Cu and physically with Pd. The sensors response of the RGO/NPs confirmed the improvement of the sensitivity of the material with these decoration methods. We also observed that the RGO doping type can be tuned with the temperature. The further investigations will be on the selectivity towards other pollutants, the optimization of the decoration to achieved a higher sensitivity and selectivity, and the understanding of the p-n transition.

#### Acknowledgements

We would like to thank Christelle Blavignac, Claire Szczepaniak, Lorraine Novais Gameiro, Centre Imagerie Cellulaire Sante (CICS) – Université Clermont Auvergne, for their technical support for TEM experiments. The authors thank 2MATECH for SEM samples analysis.

#### References

1. OSHA, “Safety and Health Topics Hydrogen Sulfide.” [Online]. Available: <https://www.osha.gov/hydrogen-sulfide/hazards>.
2. INRS, “Sulfure d’hydrogène - Fiche toxicologique n° 32,” 2014. [Online]. Available: [https://www.inrs.fr/publications/bdd/fichetox/fiche.html?refINRS=FICHETOX\\_32&section=VLE](https://www.inrs.fr/publications/bdd/fichetox/fiche.html?refINRS=FICHETOX_32&section=VLE) PMesurage.
3. F. Schedin *et al.*, “Detection of individual gas molecules adsorbed on graphene,” *Nat. Mater.*, vol. 6, no. 9, pp. 652–655, Sep. 2007, doi: 10.1038/nmat1967.
4. M. Donarelli and L. Ottaviano, “2D Materials for Gas Sensing Applications: A Review on Graphene Oxide, MoS<sub>2</sub>, WS<sub>2</sub> and Phosphorene,” *Sensors*, vol. 18, no. 11, p. 3638, Oct. 2018, doi: 10.3390/s18113638.
5. Y. Jin, Y. Zheng, S. G. Podkolzin, and W. Lee, “Band gap of reduced graphene oxide tuned by controlling functional groups,” *J. Mater. Chem. C*, vol. 8, no. 14, pp. 4885–4894, 2020, doi: 10.1039/C9TC07063J.
6. F. Yavari *et al.*, “Tunable Bandgap in Graphene by the Controlled Adsorption of Water Molecules,” *Small*, vol. 6, no. 22, pp. 2535–2538, Nov. 2010, doi: 10.1002/smll.201001384.
7. D. Chen, J. Tang, X. Zhang, J. Fang, Y. Li, and R. Zhuo, “Detecting decompositions of sulfur hexafluoride using reduced graphene oxide decorated with Pt nanoparticles,” *J. Phys. D: Appl. Phys.*, vol. 51, no. 18, p. 185304, May 2018, doi: 10.1088/1361-6463/aaba95.
8. V. Agarwal and P. B. Zetterlund, “Strategies for reduction of graphene oxide – A comprehensive review,” *Chem. Eng. J.*, vol. 405, no. May 2020, p. 127018, 2021, doi: 10.1016/j.cej.2020.127018.

# Ultra-high sensitive NO<sub>2</sub> gas microsensor for environmental monitoring or mapping of urban air quality

T. Gueye<sup>1\*</sup>, J. Brunet<sup>1</sup>, A. Ndiaye<sup>1</sup>, C. Varenne<sup>1</sup>, E. Ruiz<sup>1</sup>, A. Pauly<sup>1</sup>

<sup>1</sup> Université Clermont Auvergne, Clermont Auvergne INP, CNRS, Institut Pascal, F-63000 Clermont–Ferrand, France.

## Abstract

Our research focused on the study of 50 nm CuPc thin films as a sensing layer for the development of ultra-sensitive microsensors for NO<sub>2</sub> monitoring in the ppb range. Gas sensor characterizations under pollutant highlight very sensitive, repeatable and reproducible response towards NO<sub>2</sub> even at low temperature. A very low detection limit of 4 ppb is performed at 60°C. Such microsensor can be used for high resolution air quality mapping in an urban environment. It can also be used in an early detection system for NO<sub>2</sub> before the critical concentration. The effects of humidity and other interfering gaseous pollutants (H<sub>2</sub>S, SO<sub>2</sub>, O<sub>3</sub> and COVs) on the sensor responses have been investigated.

**Keywords:** Phthalocyanine, Nitrogen dioxide, ppb concentration range, Gas microsensor, Pollutant monitoring.

## 1. Introduction

Nitrogen dioxide, NO<sub>2</sub>, is one of the main gaseous pollutants that contributes to the formation of ozone and acid rain. Its presence into the troposphere contributes to the formation and modification of other air pollutants [1-3]. Taking into consideration its toxicity for human as well as on environment even at low levels and the non-significant decrease of its concentration in air, it's imperative to ensure a continuous monitoring of this gas into the low atmosphere. For such an application, the development of lower cost sensors than satellite experiments and sensors based on chemiluminescence for the detection of NO<sub>2</sub> at the ppb level has attracted considerable attention in recent years as illustrated by many scientific papers on this topic and the increasing economic market of gas sensors.

Encouraging performances have been performed on thin films based on molecular organic semiconductors, in particular free-phthalocyanine (H<sub>2</sub>Pc) and its metal complexes (MPcs) due to their special electrical and optical properties [6-10]. Their p-type semiconductor behavior is of great interest for NO<sub>2</sub> detection in the practical environment because of their great reactivity with oxidizing species and its very low sensitivity towards reducing species. Their cheap synthesis, easy layering process and the great diversity of available molecules (diversity of central metal atom as well as peripheral grafting groups) make them attractive for the development of low-cost and conformable devices. Among metallophthalocyanines, Copper Phthalocyanine (CuPc) has been widely used for the detection of oxidizing pollutants, in particular NO<sub>2</sub> with success and sustainability [10].

This paper deals with the sensing potentialities of nanometric layers of CuPc (thickness: 50nm) associated to conductimetric transducers aimed to developed high sensitive, selective and high-resolution monitoring of nitrogen dioxide in air.

## 2. Material and methods

β-form Copper(II) Phthalocyanine (C<sub>32</sub>H<sub>16</sub>CuN<sub>8</sub>), named as CuPc, was purchased from Sigma- Aldrich company with a purity higher than 90%. Nanometric layers (CuPc: 50nm) were performed by thermal evaporation under secondary vacuum (P = 5.10<sup>-6</sup> mbar). An automatic deposition control system associated with an in-situ quartz oscillator has allowed us to both control the thickness layered on the samples as well as the evaporation rate at 0.2 nm/s to achieve homogenous layers. After the deposition process, the layer thicknesses were confirmed by ellipsometric measurements. Such sensitive layers were realized onto 15mm<sup>2</sup> alumina substrates where were screen-printed interdigitated platinum electrodes on the upper side and a platinum resistive heater on the lower side. During each deposition process, the substrates were maintained at room temperature and no post-deposition thermal annealing

was performed. Interdigitated electrodes were polarized via 5V D.C and a data acquisition system (Keithley model 2700) acquired a voltage image of the electronic conductivity of the CuPc nanometric film.

Infrared spectra of powdered materials and thermally evaporated thin films on silicon substrate were recorded by FT-IR spectrometer (Thermo Nicolet 5700). Surface morphology was probed using a scanning electron microscope (SEM) on thin film processed onto gold substrates. The SEM micrographs were obtained from a Cambridge Scan 360 SEM operating at 3 kV.

For the determination of sensor responses and the assessment of gas detection performances, all the fluid circuit and measuring cell were made with PTFE in order to minimize the adsorption and decomposition of gas molecules on the internal surfaces. The carrier gas is generated from ambient air through silicate gel cartridge as desiccant and activated carbon columns as gas purifier to obtain dry and depolluted air named zero air. The pure and dry nitrogen dioxide  $\text{NO}_2$  is delivered by commercial cylinder of calibrated concentration purchased from Linde. For experiments,  $\text{NO}_2$  is diluted into zero air by computer-controlled mass flow controllers. An in-situ temperature and humidity sensor (hydroclip HC2A from Rotronic) is used to have continuous information about temperature and relative humidity into the exposure chamber where implemented gas microsensor.

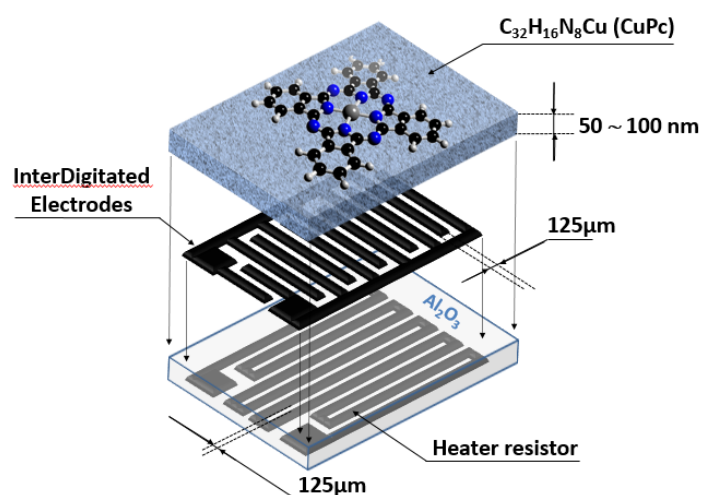


**Fig. 1:** Schematic of phthalocyanine-based conductimetric gas sensor

### 3. Results and discussion

The deposition of phthalocyanine thin films by thermal evaporation at low deposition range on substrates maintained at room temperature performs highly homogenous and amorphous layers. In order to characterize the morphology as well as the molecular organization of the surface, scanning electron microscope (SEM) was used on CuPc layers deposited onto a gold substrate maintained at room temperature. Images of the surface for two magnifications are reported in Fig. 2. At  $\times 10^4$  enlargement (microscopic scale), the CuPc layers are globally smooth and constituted by fine grain crystallites on the surface (Fig. 2a). At nanometric scale ( $\times 10^5$  enlargement), growth germs of nanowire are revealed by SEM micrograph in Fig. 2b. If columnar arrangements of the CuPc macrocycles are well-established for thicker layers (higher than 300nm), global amorphous organization is predominant for nanometric films (thickness  $< 100\text{nm}$ ). Such amorphous organization increases the number of available gas adsorption sites into the layer volume, which further increases its sensitivity to gas.

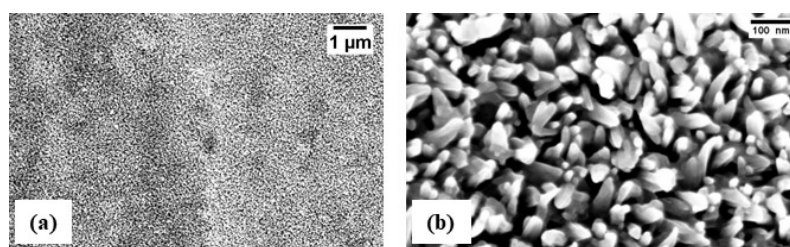


**Fig. 1:** SEM micrographs of CuPc layer with  $10^4$  (a) and  $10^5$  (b) enlargement, respectively

The sensing performances at low temperature of a conductometric sensor implementing 50 nm of CuPc exposed to low concentrations of  $\text{NO}_2$  were measured. The response of phthalocyanine-based gas microsensors strongly depends on the operating temperature and the time of  $\text{NO}_2$  exposure. Indeed, temperature strongly influences the adsorption/desorption ratio of gaseous species. As a consequence, the exposure time/ recovery time ratio must be selected to benefit from a significant variation of sensor signal as compared to noise (high signal/noise ratio) and a good level of reversibility to achieve repeatable measurements. To favor gas adsorption leading to higher conductivity variations and to prevent sensor drift induced by potential outdoor temperature variations, the optimized working temperature was set to  $60^\circ\text{C}$  for all measurements. Regarding the exposure times, the ratio 15min of  $\text{NO}_2$  exposure / 60 min for recovery has been selected. The choice of this long recovery time, compared to the exposure time, is justified by the difficulty of removing the  $\text{NO}_2$  species adsorbed on the Phthalocyanine layer at low temperature with dry air. The sensor response was firstly determined in the 0-30 ppb range. Fig.3a shows the conductivity variations of microsensor versus time for  $\text{NO}_2$  increasing concentrations. Six cycles were successively recorded, corresponding to six different  $\text{NO}_2$ /air ratio ranging from 0 to 30 ppb with a concentration step of 5 ppb. As shown in the figure, the conductivity of the CuPc film increases during exposure to  $\text{NO}_2$  due to the oxidizing nature of the gas, even at very low concentrations. This is a typical response of a p-type semiconductor to an oxidizing analyte. The signal/noise ratio is high and despite the non-complete desorption of  $\text{NO}_2$  molecules from the sensing layer during recovery step under clean air, the magnitude of conductivity variation measured during proportionately increases with  $\text{NO}_2$  concentration. Fig. 3b depicts the  $\text{NO}_2$  calibration curve obtained from the results reported in Fig. 3a. It is defined by the variation of the conductivity of the CuPc-based sensor during exposure step with respect to the  $\text{NO}_2$  concentration in the range of 0 to 30 ppb. The calibration curve is linear with a determination factor greater than 0,99. The sensitivity, calculated from the slope of the linear fitting is equal to  $6,76 \cdot 10^{-10} (\Omega \cdot \text{cm} \cdot \text{ppb})^{-1}$ . If the sensitivity seems low, it is important to mention that metallophthalocyanines have very weak intrinsic conductivity too. However, their reactivity with oxidizing gases is high. Doping by gaseous molecules make them semiconductor with high extrinsic conductivity. From data reported from fig. 3, the threshold as well as the resolution are greater than 5 ppb. Moreover, these microsensors exhibit low power consumption because of low working temperature requested and low current due to the high resistivity of the sensing layer. The enhanced detection properties are probably due to the easy diffusion of gas molecules to the high density of available adsorption sites present into the sensing layer volume because of the reduced phthalocyanine layer thickness.

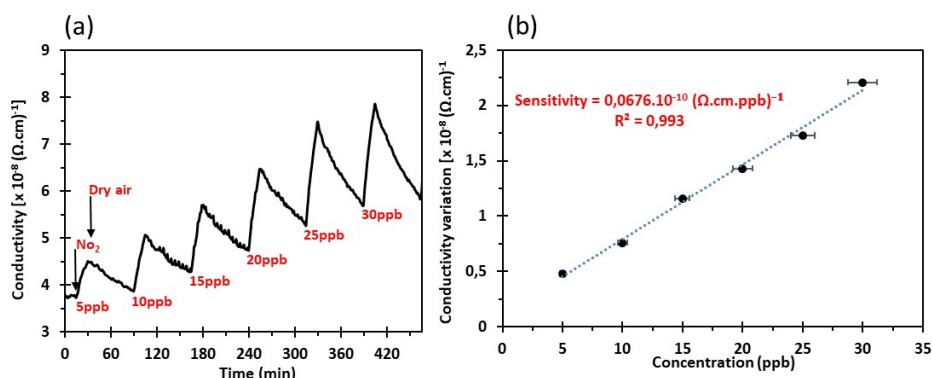


**Fig. 2:** (a) Typical dynamic responses of CuPc (50nm) based sensor in presence of NO<sub>2</sub> (0–30 ppb) and dry air. (b) Conductivity variations of the sensor versus NO<sub>2</sub> concentration. The operating temperature was set to 60°C.

In order to assess the level of repeatability and to investigate a potential hysteresis, measurement during exposures to different increasing and decreasing concentrations have been performed. Fig. 4a shows the conductivity of 50nm-CuPc layer maintained at 60 °C versus time for successive exposures to NO<sub>2</sub> with consecutive recovery under zero air in the 4-20 ppb concentration range. Moreover, two consecutive sequences were achieved in order to evaluate the repeatability of the microsensor. At first, the figure highlights that the evolution of conductivity with time during exposure steps are closely similar for the two sequences. Secondly, desorption profiles during recovery steps are closely similar too. The kinetics of adsorption and desorption remain unchanged as well as the magnitudes of conductivity variations. A very good repeatability is performed. Thirdly, as established by the calibration curve depicted in fig. 4b from the dynamic results reported in figure 4a., the change in conductivity versus concentration is linear. The small dispersion of experimental points for each NO<sub>2</sub> concentration indicates clearly that the resolution is higher than the experimental concentration step chosen, i.e. 4 ppb.

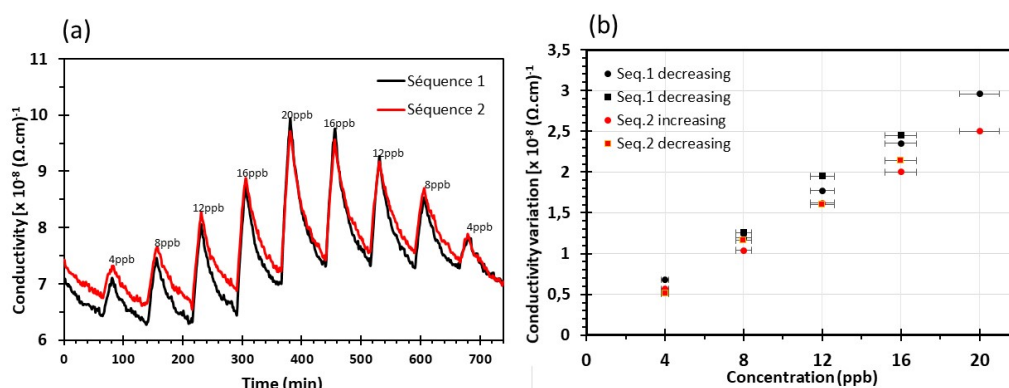


**Fig. 3:** response of the CuPc-based microsensor as a function of NO<sub>2</sub> concentration at 60°C. The concentration range is 4–20 ppb with a 4ppb incremental step. (a) Conductivity variation versus time for two consecutive exposure sequences with increasing and decreasing concentration, (b) Conductivity variations extracted from results reported in fig. (a) versus NO<sub>2</sub> concentrations.

Fig. 5 reports the conductivity of the CuPc thin film maintained at 60°C as a function of time for five pollutants: Nitrogen dioxide NO<sub>2</sub>, Ozone O<sub>3</sub>, Sulphur dioxide SO<sub>2</sub>, Xylene C<sub>8</sub>H<sub>10</sub> and toluene C<sub>7</sub>H<sub>8</sub>). The experiments were carried out successively on the same CuPc layer and the sensor was maintained at 60°C. It is therefore possible to compare the experimental results obtained for successive switchings between 50 ppb of each pollutant considered for 15min and dry air for 1h. These curves emphasize a partial selectivity, the microsensor being completely insensitive to interfering gases such as Xylene, Toluene, SO<sub>2</sub>, and H<sub>2</sub>S (not shown in the figure). In contrast, the great sensitivity of CuPc layers to oxidizing gases like NO<sub>2</sub> and O<sub>3</sub> is well known and confirmed in this low concentration range. Both NO<sub>2</sub> and O<sub>3</sub> produce a significant increase in conductivity, even at ppb level and low working

temperature. Although  $\text{NO}_2$  and  $\text{O}_3$  are two strongly oxidizing gaseous species that induce the creation of free charge carriers in the CuPc layer, a higher sensitivity to  $\text{NO}_2$  is noticeable. It can be seen from the figure that exposure of the CuPc layer to ozone results in an irreversible decrease in sensor conductivity. Such behavior is attributed to the irreversible breaking C-C double bonds of the macrocycles according to an ozonolysis process leading to the slow degradation of the surface as consequently the decrease in the density of active sites. Thus, mainly responsible of the decrease in sensor lifetime,  $\text{O}_3$  is the most prejudicial interfering gas when measuring  $\text{NO}_2$  in the real atmosphere for a CuPc-based gas sensor. Both to achieve a complete selectivity towards  $\text{NO}_2$  and to prevent premature ageing of the sensing layer by  $\text{O}_3$ , chemical filters based on indigo, nanocarbons and hybrid materials can be implemented upstream microsensors as on-line pretreatment for selective ozone removal [11-13].

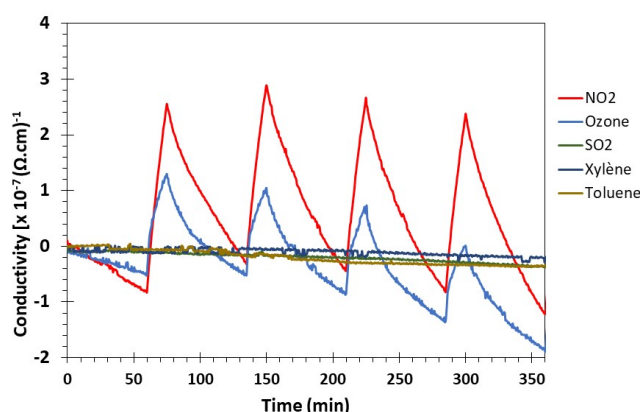


**Fig. 4:** Conductivity variations versus time of CuPc-based sensors maintained at low temperature ( $60^\circ\text{C}$ ) and exposed to 50 ppb of 5 different pollutants:  $\text{NO}_2$ ,  $\text{O}_3$ ,  $\text{SO}_2$ , Xylene and Toluene.

#### 4. Conclusion

Gas sensor characterization under pollutant highlight a very sensitive, repeatable, and reproducible  $\text{NO}_2$  gas sensor with a very low detection limit of 4 ppb at  $60^\circ\text{C}$ . The effect of interfering air pollutants ( $\text{H}_2\text{S}$ ,  $\text{SO}_2$ ,  $\text{O}_3$ , and BTEX) on the sensor response has been assessed: no sensor response was observed. A high level of selectivity was reached. It constitutes a great advantage for sensors aimed to be distributed in real environment.

#### Acknowledgements

This work has been supported and funded by ANR CAPTAIN Project grant ANR-18-CE04-0008-01 of the French Agence Nationale de la Recherche.

#### References

1. Gruber, N.; Galloway, J.N. An Earth-system perspective of the global nitrogen cycle. *Nature* 2008, 451, 293–296.
2. Erismann, J.W.; Grennfelt, P.; Sutton, M. Nitrogen emission and deposition: The European perspective. *Sci. World J.* 2001, 1, 879–896
3. Tee Lamont Guidotti (1978). The higher oxides of nitrogen: *Inhalation toxicology.*, 15(3), 0–472. doi:10.1016/0013-9351(78)90125-1
4. Rijnders, E; Janssen, N A; van Vliet, P H; Brunekreef, B (2001). Personal and outdoor nitrogen dioxide concentrations in relation to degree of urbanization and traffic density. *Environmental Health Perspectives*, 109(suppl 3), 411–417. doi:10.1289/ehp.011109s3411
5. Schneider, Philipp et al., (2017). Mapping urban air quality in near real-time using observations from low-cost sensors and model information. *Environment International*, (2017), S0160412016310741–. doi :10.1016/j.eint.2017.05.005
6. Bernardis, Daniel A.; Malliaras, George G.; Owens, Róisín M. (2008). [Materials Science] Organic Semiconductors in Sensor Applications Volume 107 || ., 10.1007/978-3-540-76314-7(), -. doi:10.1007/978-3-540-76314-7

7. A. Heilmann, V. Lantto, M. Müller, C. Hamann, NO<sub>2</sub> monitoring as an air pollutant using lead phthalocyanine thin film sensors, *Sens. Actuators B* 7 (1992) 522–525.
8. Mead, M.I.; Popoola, O.A.M.; Stewart, G.B.; Landshoff, P.; Calleja, M.; Hayes, M.; Baldovi, J.J.; McLeod, M.W.; Hodgson, T.F.; Dicks, J.; et al. The use of electrochemical sensors for monitoring urban air quality in low-cost, high density networks. *Atmos. Environ.* 2013, 70, 186–203
9. J. Brunet, J.P. Germain, A. Pauly, J.P. Blanc, Comparisons between NO<sub>2</sub> and O<sub>3</sub> sensing properties of phthalocyanines and n-InP thin films in controlled and non-controlled atmosphere, *IEEE Sens. J.* 4 (2004) 735–742.
10. Y.-L. Lee, W.-C. Tsai, C.-H. Chang, Y.-M. Yang, Effects of heat annealing on the film characteristics and gas sensing properties of substituted and un-substituted copper phthalocyanine films, *Appl. Surf. Sci.* 172 (2001) 191–199.
11. J. Brunet, L. Spinelle, A. Pauly, M. Dubois, K. Guérin, M. Bouvet, C. Varenne, B. Lauron, A. Hamwi, All-organic device with integrated chemical filter dedicated to the selective measurement of NO<sub>2</sub> in air, *Organic Electronics* 11 (2010), 1223-1229.
12. J. Brunet, M. Dubois, A. Pauly, L. Spinelle, A.L. Ndiaye, K. Guérin, C. Varenne, B. Lauron, An innovative gas sensor system designed from a sensitive organic semiconductor downstream a nanocarbonaceous chemical filter for the selective detection of NO<sub>2</sub> in an environmental context. Part I: Development of a nanocarbon filter for the removal of ozone. *Sens. Actuator B Chem.* 173 (2012), 659–667.
13. J. Brunet, A. Pauly, M. Dubois, M.L. Rodriguez-Mendez, A.L. Ndiaye, C. Varenne, K. Guérin, Improved selectivity towards NO<sub>2</sub> of phthalocyanine-based chemosensors by means of original indigo/nanocarbons hybrid material, *Talanta* 127 (2014), 100-107.

# Performance Evaluation of Nitrogen-doped Graphene / Carbon Black Supported Pt<sub>3</sub>Co Nanoparticles as PEM Fuel Cell Cathode Electrocatalyst

D. K. Perivoliotis<sup>1</sup>, X. Jia<sup>2</sup>, T. Wågberg<sup>3</sup>

<sup>1</sup>Department of Physics, Umeå University  
Linnaeus väg 24, Umeå 90187, Sweden, [dimitrios.perivoliotis@umu.se](mailto:dimitrios.perivoliotis@umu.se)

<sup>2</sup>Department of Physics, Umeå University  
Linnaeus väg 24, Umeå 90187, Sweden, [xueen.jia@umu.se](mailto:xueen.jia@umu.se)

<sup>3</sup>Department of Physics, Umeå University  
Linnaeus väg 24, Umeå 90187, Sweden, [thomas.wagberg@umu.se](mailto:thomas.wagberg@umu.se)

## Abstract

The development of novel and highly active electrocatalysts for fuel cells towards the oxygen reduction reaction (ORR) is a core challenge for the widespread commercialization of such energy conversion technologies. Considerable efforts and significant achievements have been made in the field leading to the development of numerous ORR electrocatalysts with exceptional performance. However, most of these studies are focused on the performance of these catalysts on the rotating disk electrode (half-cell) level and only few data are available at a complete-cell level. In this work, we applied a simple microwave assisted method to realize platinum-cobalt alloyed nanoparticles, abbreviated as Pt<sub>3</sub>Co NPs, uniformly distributed on mixtures of nitrogen-doped graphene (NG) and Vulcan carbon (XC). The obtained Pt<sub>3</sub>Co NPs/NG-XC hybrid materials were complementary characterized and deposited onto the gas diffusion layer (GDL) towards the preparation of the membrane electrode assemblies (MEAs). The morphology and the surface properties of the catalyst layer were thoroughly examined. The effect of the NG to XC ratio on the polymer electrolyte membrane (PEM) fuel cell performance was investigated. According to the results, the optimum XC to NG ratio was found to be 10:90 and the corresponding catalyst exhibited a maximum power density of 0.4 W cm<sup>-2</sup> at an operating temperature of 60 °C and Pt loading of 0.2 mg cm<sup>-2</sup>, outperforming not only the NG and XC based references but also the benchmark Pt/C catalyst. Notably, the exceptional performance was attributed to (i) the alloyed structure of Pt<sub>3</sub>Co NPs, (ii) the intriguing properties of NG as catalyst support as well as (iii) the unique 2D/3D micro-architecture and increased hydrophobicity of the catalyst layer. Overall, Pt<sub>3</sub>Co NPs/ XC-NG (90-10) is a highly efficient ORR electrocatalyst, revealing huge potential for application in practical energy conversion devices.

**Keywords:** Polymer Membrane Electrolyte Fuel Cell; Electrocatalysis; Oxygen Reduction Reaction; Nitrogen-doped Graphene; Alloyed Nanoparticles

## 1. Introduction

Nowadays, unprecedented energy demands have forced the research community to invest in alternative energy sources, including fuel cells. Polymer electrolyte membrane fuel cells (PEMFCs) have emerged as the most promising and environmentally friendly power sources for application in automobiles and portable electronics. The commercialization of such systems requires the development of new highly efficient and durable cathode electrocatalysts to accelerate the kinetically sluggish oxygen reduction reaction (ORR). In this regard, much effort has been devoted during the past decade aiming at either the development of catalytic nanoparticles with complex nanostructures (i.e., alloyed, core-shell) or the exploration of novel supports. Among the different supporting materials, graphene due to its large surface area, excellent electrical conductivity, and good chemical stability has been widely used as a platform for the construction of ORR electrocatalysts [1]. For most graphene-based electrocatalysts, their performances have been only evaluated in the half-cell test, showing a great potential for further use in PEMFCs; however, they cannot be accurate as they do not represent their activities and durability under real operating conditions. The main reasons can be summarized as following: (i) the mass transfer resistance (O<sub>2</sub> diffusion) which is significantly eliminated in half-cell tests (rotating disk electrode, RDE, measurements) is dominant under PEMFC conditions; (ii) the lower active sites accessibility at the MEA level due to the triple-access (gas-liquid-solid) requirements; (iii) the high O<sub>2</sub> concentration at PEMFC level results in water and heat management issues and last (iv) the different operating conditions (i.e. temperature, humidity,

etc.) of the fuel cells [2-3]. Therefore, there is a compelling need to be conducted more research on the performance of graphene-based electrocatalysts under practical conditions before their application in commercial PEMFC devices.

Herein, we take the advantage of the excellent ORR electrocatalytic performance of the alloyed Pt<sub>3</sub>Co NPs at half-cell level [4] and we go beyond the state of the art by investigating the effect of different catalytic NP supporting materials on their PEMFC performance. In more detail, we enable mixtures of nitrogen-doped graphene (NG) and Vulcan carbon (XC-72R) at different ratios as platforms for the Pt<sub>3</sub>Co alloyed NPs aiming at a deeper understanding of the role of graphene as supporting material under real conditions. Overall, these results clearly suggest the incorporation of graphene nanosheets into the currently used Vulcan carbon support toward the development of high performance ORR electrocatalyst under practical PEMFC conditions and pave the way for the commercialization of the fuel cell technology.

## **2. Experimental Part**

### **2.1. Microwave-assisted synthesis of Pt<sub>3</sub>Co NPs/ NG-XC hybrids**

Pt<sub>3</sub>Co nanoparticles supported on mixtures of N-doped graphene and Vulcan XC 72R were synthesized through a two-step dry-state microwave reaction followed by a post-annealing treatment. First, the appropriate amount of platinum(ii) acetylacetonate (Pt(acac)<sub>2</sub>) and cobalt(ii) acetate tetrahydrate ((CH<sub>3</sub>COO)<sub>2</sub>Co·4H<sub>2</sub>O), were dispersed in tetrahydrofuran (THF) and afterwards mixed with the proper ammonium nitrate (NH<sub>4</sub>NO<sub>3</sub>) dissolved in methanol. The solution was poured into an agate mortar containing mixtures of NG and Vulcan XC 72R and ground until a completely dry powder had formed. The designed Pt to Co atomic ratio was 3:1 and the % Pt loading at the final hybrids 20% wt. Samples containing 0, 5, 10, 20 and 100 % NG were prepared. Next, the powder was loaded into a quartz crucible and placed in a dead-ended quartz tube connected to a custom modified household microwave oven (800 W), capable of supplying gases into the reaction vessel. After 1 h purge in a flow of Ar, the microwave oven was set to full power for 5 min. Afterwards, the chamber was purged with 5% H<sub>2</sub> in Ar for at least 30 min after which the microwave oven was set to 50% power for 1 h. At the last step, the samples were placed in a tubular furnace and treated at 700 °C under 5% H<sub>2</sub> in Ar atmosphere for 2 h.

### **2.2. Physical Characterization**

X-ray diffractograms were acquired with a Panalytical X'Pert<sup>3</sup> Powder diffractometer using a CuKα (λ = 1.5406 Å) source. X-ray photoelectron spectra (XPS) were acquired with a Kratos Axis Ultra DLD spectrometer using a monochromated Al Kα source operated at 120 W. Scanning electron microscopy (SEM) imaging was carried out with a Zeiss Merlin field emission SEM operating with an accelerating voltage of 4 keV. Transmission electron microscopy (TEM) was performed with a JEOL-1230 microscope with an accelerating voltage of 80 kV. For the contact angle measurements, small individual water droplets were placed on the dry catalyst and measured with an optical tensiometer from Biolin Scientific. The angles were fitted by the Young Laplace method using Attension software.

### **2.3. Membrane electrode assembly (MEA) fabrication and characterization**

The fabrication of 5 cm<sup>2</sup> membrane electrode assemblies (MEAs) was made by sandwiching pre-treated membranes (Type N212) between the anode and cathode electrodes. The cathode electrode was prepared by decorating a gas diffusion layer (type 28 BC carbon paper, Sigracet®) with the produced Pt<sub>3</sub>Co NPs/ NG-XC catalysts (loading of 0.2 mg<sub>Pt</sub> cm<sup>-2</sup>). Catalyst deposition took place by spraying the appropriate catalyst ink (5 mg ml<sup>-1</sup> catalyst in a mixture of Nafion solution (DuPont, Ion-Power 5 wt. %), distilled water and 2-propanol in 0.3 : 8.7 : 1 volumetric ratio), followed by drying at 60 °C. The same procedure was followed for the preparation of the anode electrode using the commercial available 20% Pt/C catalyst instead. Membranes were pre-treated by heating for 1 h at 80 °C consequently in 3% H<sub>2</sub>O<sub>2</sub>, H<sub>2</sub>O DI, 0.5 M H<sub>2</sub>SO<sub>4</sub> and H<sub>2</sub>O DI respectively and finally stored in H<sub>2</sub>O DI until usage. The MEAs were finally produced by hot-pressing with a pre-treated N212 membrane for 4 min at 130 °C at 60 kg cm<sup>-2</sup> pressure with a Stahls Hotronix® 6" × 6" heat press. The as produced MEAs were loaded into a cell fixture (quickCONNECT, Baltic FuelCells GmbH) with serpentine flow fields connected to a Scribner 850e fuel cell test system. The fuel cell was operated at 60 °C and 95% RH on both anode and cathode with gas flows of 100 ml min<sup>-1</sup>. Break-in procedures took place by operating the cell at constant potential of 0.55 V until reaching stable performance.

### 3. Results and discussion

Alloyed Pt<sub>3</sub>Co nanoparticles with a 3:1 Pt to Co atomic ratio decorated on mixtures of NG and Vulcan XC 72R at different ratios (0:100, 5:95, 10:90, 20:80 and 100:0) were obtained in a two-step dry-state microwave reaction. In more detail, a dry mixture of the carbon supports (NG and Vulcan), metal precursors and NH<sub>4</sub>NO<sub>3</sub> (oxidative agent) were successively exposed to microwaves under Ar and 5% H<sub>2</sub> in Ar atmosphere, followed by a post-annealing treatment in reductive atmosphere. The presence of NH<sub>4</sub>NO<sub>3</sub> contributes to the controlled oxidative removal of carbonaceous species in the very initial stages of the NP formation yielding NPs with significant higher electrochemical active surface area (ECSA) according to our previous work [4]. The final post-annealing step not only allows the further reduction of the NPs but more importantly contributes to a better alloyed structure. The morphology of the as produced hybrid electrocatalysts was investigated via transmission electron microscopy (TEM) imaging. No significant differences between the samples were detected. A representative TEM image of Pt<sub>3</sub>Co NPs/ XC-NG (90:10) is shown in Fig. 1a. As it can be seen, the Pt<sub>3</sub>Co NPs are uniformly distributed on both carbon supports while their size was approximately 5 nm. The X-ray diffraction (XRD) patterns show an upshift of all Pt *fcc* peaks compared to the commercial Pt/C indicating the incorporation of the Co into the Pt lattice. The absence of separate peaks attributed to Co or Co oxides further confirms the alloyed structure of the Pt<sub>3</sub>Co NPs. Furthermore, X-ray photoelectron spectroscopy was employed to gain insight into the hybrids elemental composition. According to the results, C, O, Pt and Co were detected in all samples while N (as pyridinic N, pyrrolic N and graphitic N) was also detected in samples containing NG. The Pt : Co atomic ratio derived from the XPS was calculated around 2.6 : 1.0 in all cases, being close to the designed 3 : 1.

The catalyst films were deposited onto the gas diffusion layer (carbon paper) via spraying method. Their microstructure and surface properties (hydrophobic behaviour) were thoroughly investigated by means of SEM imaging and contact angle measurements, respectively. Interestingly, SEM imaging revealed a 3D/2D porous micro-architecture for all Pt<sub>3</sub>Co NPs/ XC-NG based catalyst layers (Fig. 1b) due to the unique combination of NG and Vulcan XC 72R supports (NG acted as a spacer) contrasting the layer composed of the Pt<sub>3</sub>Co NPs/ NG catalyst. In that case, a compact structure of stacked 2D NG sheets was formed (Fig. 1b, inset). Next, contact angle assays suggested an increased hydrophobicity for all Pt<sub>3</sub>Co NPs/ XC-NG specimens. In more detail, their contact angle was found between 135° and 140°, being significantly higher than to that of Pt<sub>3</sub>Co NPs/ NG (115°) and Pt<sub>3</sub>Co NPs/ XC (118°) catalyst layers.

The PEMFC performance of all Pt<sub>3</sub>Co/XC-NG catalysts was evaluated at an operating temperature of 60 °C and Pt loading on both anode and cathode of 0.2 mg cm<sup>-2</sup>. According to the results (Fig. 1c), the optimum XC to NG ratio was found to be 90:10 and the corresponding catalyst exhibited a maximum power density of 0.4 W cm<sup>-2</sup>, being 40 % and 15 % higher compared to that of Pt<sub>3</sub>Co/XC reference and commercial Pt/C catalyst, respectively. Actually, the addition of NG to the Vulcan not only allowed us to exploit the exceptional properties of NG (i.e. high electrical conductivity, affinity with metal NPs, chemical stability) [1] but also acted as spacer by yielding a catalyst layer with increased porosity and hydrophobicity. Both characteristics are essential when considering the application at MEA level as they ensure both a high utilization efficiency (accessibility of active sites) and an effective water management within the MEA (avoiding the flooding phenomena that typically lead to reduced performance) [2-3]. On the other hand, the surprisingly low maximum power density of 0.1 W cm<sup>-2</sup> for the Pt<sub>3</sub>Co/NG hybrid was primarily ascribed to the low accessibility of the active sites due to the compact microstructure (stacked NG nanosheets) of the catalytic layer [3]. The later result highlights the significance of evaluating the electrocatalyst performance at full-cell level instead of only reporting their ORR activity at RDE level.

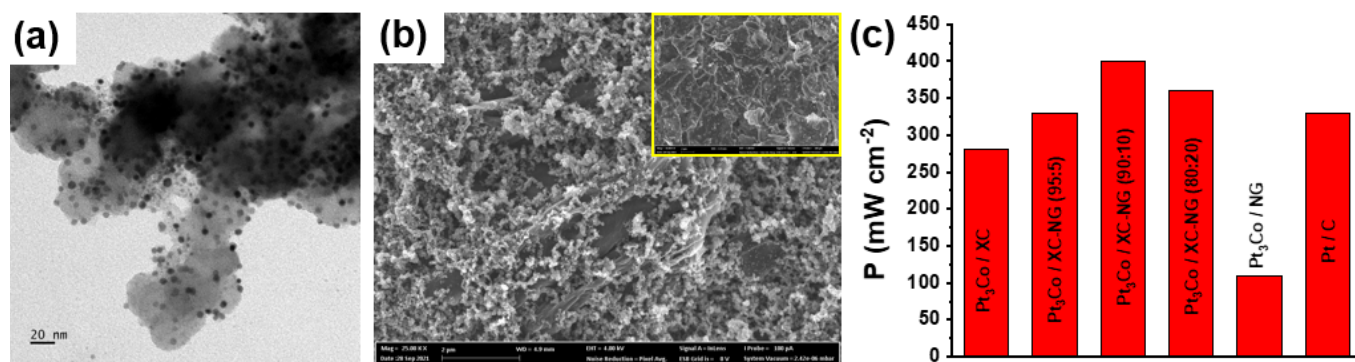


**Fig. 1:** (a) TEM image of Pt<sub>3</sub>Co / XC-NG sample; (b) SEM image of the Pt<sub>3</sub>Co / XC-NG catalyst layer. Inset: image of Pt<sub>3</sub>Co / NG catalyst layer; (c) PEMFC performance of all Pt<sub>3</sub>Co catalysts as compared with that of commercial Pt/C catalyst.

#### 4. Conclusion

In summary, the fabrication of the Pt<sub>3</sub>Co/XC-NG hybrids, with different XC-to-NG ratios, as potential electrocatalysts for ORR, through a simple dry-state microwave-assisted procedure, was accomplished. TEM imaging along with complementary spectroscopic techniques (XRD and XPS) confirmed the successful formation of uniformly distributed alloyed Pt<sub>3</sub>Co NPs (with average size of 5 nm) onto the different carbon supports. The addition of NG to the Vulcan not only allowed us to exploit the exceptional properties of NG but also acted as spacer by yielding a catalyst layer with increased porosity and hydrophobicity as proved by SEM imaging and contact angle measurements. The hybrid material with the optimum XC-to-NG ratio, namely Pt<sub>3</sub>Co/XC-NG (90:10), demonstrated an excellent PEMFC performance (0.4 W cm<sup>-2</sup> at an operating temperature of 60 °C and Pt loading on both anode and cathode of 0.2 mg cm<sup>-2</sup>), outperforming not only the XC and NG based references but more importantly the benchmarked Pt/C catalyst. Such exceptional performance was ascribed not only to the alloyed structure of Pt<sub>3</sub>Co NPs and the intriguing properties of NG but more importantly to the unique 2D/3D micro-architecture and increased hydrophobicity of the resulting catalyst layer which ensure the accessibility of the active sites and the efficient water management at the MEA level.

#### Acknowledgements

D.P. gratefully acknowledges the support from Kempe Foundation.

#### References

1. D.K. Perivoliotis, N. Tagmatarchis, “Recent advancements in metal-based hybrid electrocatalysts supported on graphene and related 2D materials for the oxygen reduction reaction”, *Carbon*, vol. 118, pp. 493-510, 2017.
2. H. Su, Y.H. Hu, “Recent advances in graphene-based materials for fuel cell applications”, *Energy Sci Eng.*, vol. 9, pp. 958– 983, 2021.
3. X. Tian, X. F. Lu, B. Y. Xia, X. W. Lou, “Advanced Electrocatalysts for the Oxygen Reduction Reaction in Energy Conversion Technologies”, *Joule*, vol. 4, No. 1, pp. 45-68, 2020.
4. R. Sandström, J. Ekspong, E. Gracia-Espino, T. Wågberg, “Oxidatively induced exposure of active surface area during microwave assisted formation of Pt<sub>3</sub>Co nanoparticles for oxygen reduction reaction”, *RSC Adv.*, vol. 9, pp. 17979-17987, 2019.

# Memristive Graphene/Ionic Liquid Devices: Characterization and Demonstration of Associative Learning

I. Köymen<sup>1,\*</sup>, S. Liu<sup>2</sup>, S. Ergöktaş<sup>2</sup>, C. Kocabaş<sup>2</sup>

<sup>1</sup> Department of Electrical and Electronics Engineering, TOBB University of Economics and Technology, Ankara 06560, Turkey [ikoymen@etu.edu.tr](mailto:ikoymen@etu.edu.tr)

<sup>2</sup> Department of Materials, National Graphene Institute, University of Manchester, M13 9PL, Manchester, United Kingdom

## Abstract

Flexible and biocompatible memristive devices are particularly attractive for bioelectronic systems due to the interest in improving computing capabilities and the motivation to interface electronics with biological systems including drug delivery, neural interfaces and biosensors. Structures made of more unorthodox, organic material can address different issues due to their characteristics: flexibility, conformability, biocompatibility and simple and low-cost fabrication. It has been observed that gating Graphene/Ionic Liquid (IL) devices leads to the formation of an electrical double layer (a thin layer of ions with a thickness of a few nanometers) at the graphene/IL interface due to the local potential difference which also controls the local conductivity. This structure provides a memristive mechanism based on a dynamic p-n junction formation along the channel. Motivated by this memristive behavior, graphene/IL devices were assembled with the aim of demonstrating memristive behavior and associative learning. This work investigates memristive properties of flexible graphene/ionic liquid devices on polymer substrates. The I-V characteristics of these novel devices and switching mechanism are investigated. Two distinct topologies (single input, single output and double input, single output) of devices are manufactured and tested to mimic conditioning. It is observed that the application of voltage pulse trains of both positive and negative polarities increases the device conductance and allows larger currents to pass after repetitive excitation. This characteristic was exploited to condition devices and emulate associative learning.

**Keywords:** memristor, graphene, ionic liquid, associative learning, neuromorphic applications

## 1. Introduction

There has been a shift in the evolution of electronics; while area constraints remain ever present, there is also an interest in improving the functionality of devices. The memristor is a fine example of a device which satisfies both requirements: it is small and has properties which introduce new functionality to electronics such as memory and nonlinear behavior, making it suitable for bioinspired circuits. Following this trend, biocompatible electronic material is increasingly being applied to biomedical applications. The key motivating factor here is that organic material is particularly suitable for interfacing electronics with biological systems including drug delivery, neural interfaces and biosensors [1]. Structures utilizing poly(3,4-ethylenedioxythiophene) doped with poly(styrenesulfonate) (PEDOT: PSS) [2] and ion gel [3] have yielded biocompatible and conformable circuits which allow healthy measurements without having to penetrate tissue by binding well to the curvilinear surfaces (such as the surface of the neocortex and hippocampus). Though memristors are more commonly fabricated with CMOS compatible processes, alternative material, as mentioned previously, is being investigated such as perovskites [4], chalcogenides [5], organic materials [6] and graphene [7], [8]. Structures employing more unorthodox, biocompatible material are fabricated to offer flexibility, conformability, biocompatibility and simple and low-cost fabrication. These devices can have diverse topologies, some reportedly have areas in the range of mm<sup>2</sup> [9] and even cm<sup>2</sup> [3]. The devices fabricated and investigated in the present work benefit from the low-cost, simple fabrication methods.

Graphene/IL devices have been investigated due to their optoelectronic properties [10]. Electrical and optical properties of graphene can be electrostatically tuned [11]. When used with electrolytes or IL, gating graphene/IL devices leads to the formation of an electrical double layer (a thin layer of ions with a thickness of a few nanometers) at the graphene/IL interface [10] due to the local potential difference which also controls the local conductivity as seen in Fig. 1 (a). This structure provides a memristive mechanism based on a dynamic p-n junction formation along the channel. At low bias voltages, the p-n junction blocks the current flow through the

graphene and yields high resistive state (HRS) as seen in Fig. 1 (b). This self-formed p-n junction is under forward bias, therefore increasing the bias voltage lowers the potential barrier and enhances the current. Furthermore, the Dirac point shifts to negative voltages which increases the local doping. Combination of these competing effects yields a threshold voltage. After this threshold voltage, the device enters the low resistive state (LRS) where the condition for p-n junction is broken. As a result of this mechanism, it has been observed that graphene/electrolyte/graphene structures exhibit capacitance and resistance which are strongly dependent on input voltage [10]. This behavior is attributed to gate-induced change of Fermi energy of graphene due to the bias voltage. Maximum resistance (and minimum capacitance) is observed when carrier concentration is at a minimum. This quality is in fact very similar to the ionic movement in memristive devices [12]. It is not surprising that hysteretic I-V behavior has already been observed in other similar structures [13] as well as the graphene/IL devices studied in this work, since as with memristors charge carriers move due to an excitation signal and concentrate on one side of the device which leads to a time dependent resistance variation, upon reversing the polarity of the excitation signal, ions move to the opposite side of the device and opposite (incremental or decremental) change in resistance in time is observed.

The graphene/ IL devices on flexible polymer substrates presented in this work exhibit I-V responses which are nonlinear and memristive with clear high resistive and low resistive states (HRS and LRS respectively). The devices assembled for the purposes of this work are not of the conventional sandwich-like memristor variety. They have a lateral dynamic doping profile which generates a lateral p-n junction as shown in Fig. 2.

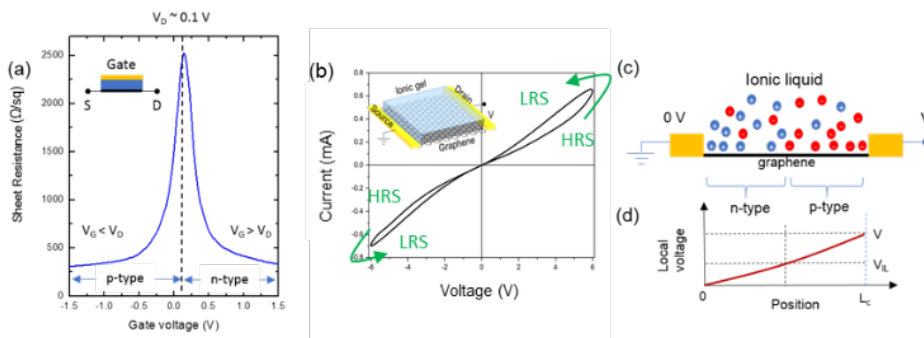


Fig. 1 Mechanism of ionic gating and hysteresis in graphene and graphene/IL devices (a) Variation of the sheet resistance of graphene with the gate voltage applied to the electrolyte. Graphene shows ambipolar transport for both electrons ( $V_G > V_D$ ) and holes ( $V_G < V_D$ ). Dirac point is around 0.1V. (b) Graphene/IL memristor: I-V curve of graphene memristor depicting low (LRS) and high resistance state (HRS) with pinched hysteresis. Device layout is shown in the inset. (c) Schematic representation of a dynamic p-n junction formed on the graphene channel. The variation of the local potential redistributes ions in the electrolyte and forms dynamic doping on graphene (d) Variation of the local potential along the channel under a bias voltage. Ionic liquid behaves as a floating gate which yields position dependent gating.

Associative learning is a process during which two seemingly independent experiences are mentally linked to one another. A familiar example of associative learning is the Pavlov's dog experiment, where a bell is rung each time Pavlov's dog is given food until finally the dog begins salivating at the sound of the bell even when there it is not presented with food. This learning mechanism whereby the body or brain begins to expect a certain type of stimulus after experiencing an independent stimulus is also called conditioning. This type of learning behavior which can be observed in memristive devices of various forms have been reported [14], [15].

Motivated by the myriad of intriguing qualities (tunable thermal radiation, electrochromic, memristive characteristics) of graphene/IL devices we assembled two different configurations of such devices with the aim of demonstrating memristive behavior and conditioning. These features could enable complex neuromorphic circuits that can emulate signal processing and conditional learning.

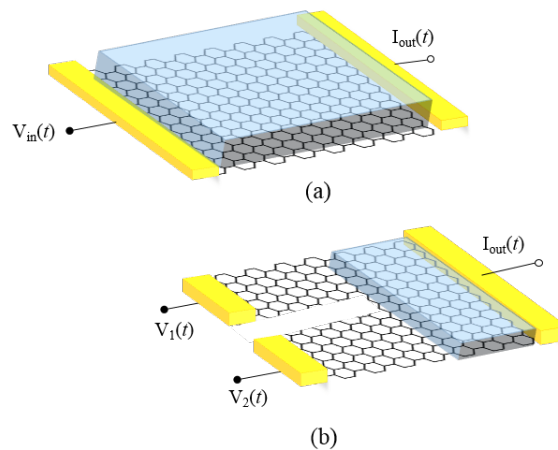


Fig. 2 Graphene/IL self-gated devices on flexible polymer substrates (a) Single input-single output device (b) Double input-single output device

## 2. Device Characterization

The graphene/IL devices are considerably different compared to majority of devices which are being and have been investigated with regards to memristive behavior, and are in the vein of the newer, biocompatible, flexible and low cost organic material based memristive devices. Their structure does not follow the common recipe of metal/oxide/ doped oxide/ metal [12]; therefore, it was important to conduct preliminary measurements to characterize these devices. The measurements presented in this work are taken from large samples (area in the order of  $\text{cm}^2$ ) as opposed to nano/micrometric devices. Another important reason for these preliminary measurements is to determine the input signal amplitude and frequency range for the experiments to follow. Not having much prior information with regards to where these devices operate, it was crucial to pinpoint frequency and amplitude response to determine pulse lengths and strengths.

Graphene/IL devices were assembled on flexible polymer substrates. I-V measurements were performed by applying ac voltage signal of different frequencies to observe hysteresis and the variation of device behavior due to differing driving frequencies. A drawing of the single-input single-output devices measured in this capacity is depicted in Fig. 2 (a).

## 3. Results and Discussion: Pulse Train Measurements for Learning Mechanism

Fig. 4 shows the measurement results recorded after the application of identical pulse trains to flexible polymer substrate graphene/IL devices. What is expected from a typical bipolar memristive device is that its memristance will decrease due to a positive excitation signal (for a voltage driven device this will mean measured current will increase in value due to continuous positive driving voltage) and a negative input signal will lead to an increase in memristance (lowering the resulting measured current value). However, the graphene/IL devices exhibit the same switching direction in both positive and negative input cycles. As such, while the measured current response to positive voltage pulses is as expected (a decreasing memristance: HRS to LRS), the response to negative pulses indicate decreasing memristance. The memristance of the devices seems to increase during polarity switches, then decreases for both negative and positive inputs. Absolute value of current magnitude due to repetitive application of both negative and positive pulses increase. Once the driving signal is 0V, the device resets. It can be said that the current response is symmetrical.

Fig. 3 depicts the characteristic pinched hysteresis loops for graphene/IL devices. The devices exhibit passive behavior: their I-V characteristics are limited to the 1<sup>st</sup> and 3<sup>rd</sup> quadrants. The frequency dependency is also as expected; higher frequencies lead to more linear behavior, hysteresis loops get wider for lower frequencies.

It is also important to note that conditioning is demonstrated with these simple pulse train experiments. Voltage pulses periodically rise to 10V and fall back down to 0V. Had these devices merely exhibited linear resistance, the measured currents would look like a scaled version of the pulse trains, reaching a certain constant current value for every pulse. However, the nonlinear, time dependent I-V characteristic of the memristive graphene/IL devices is apparent in Fig. 4. The excitation is 0V between each pulse; thus, when the device resets, the measured

current is also 0A. Following the reset after both positive and negative cycles, the magnitude of measured current of the device begins to increase while being applied repeated pulse trains of the same polarity. This behavior is due to the increasing conductance of the graphene/IL devices resulting from being applied repeated pulses. Similar to physiological systems where the increase in channel conductance translates to more current being delivered to the post-synaptic neuron [16], the conductance of this device too increases due to repeated excitation and thus larger current flows through the device.

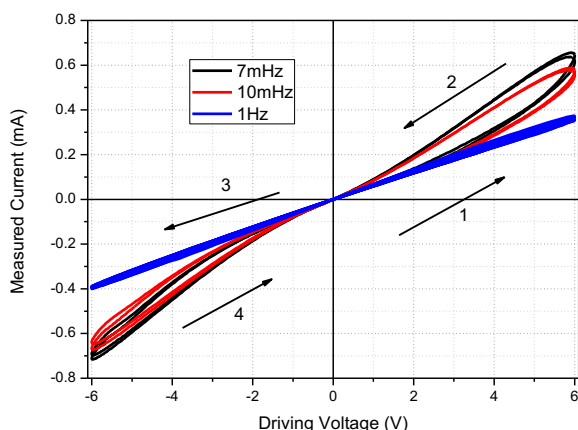


Fig. 3 Hysteresis plots of Graphene/IL devices at 3 distinct driving signal frequencies. The plots get wider as driving frequency diminishes. The switching direction is denoted with arrows.

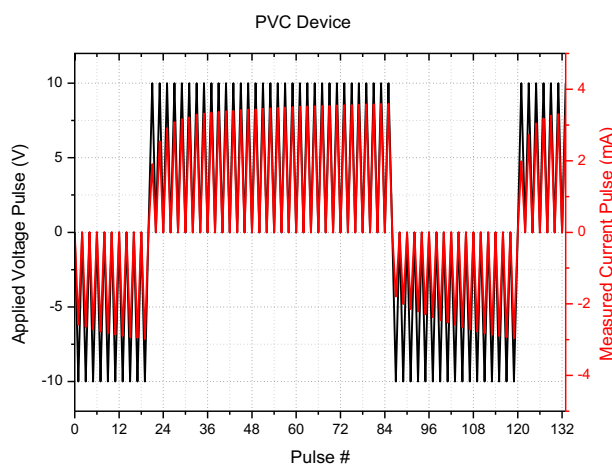


Fig. 4 Flexible polymer substrate Graphene/IL device excited with repetitive positive and negative 10 V pulse trains. Current response shown in red.

### 3.1 Two input one output device

A two input one output graphene/IL device is assembled as shown in Fig. 2 (b). This configuration is different to the typical memristor topology; yet similar to multi-gated devices seen in literature [3]. This configuration allows mimicking associative learning. It is also useful in observing the behavior of different geometries of graphene/IL devices.

Each pulse in Fig. 5 is 0.1s long. The graphene/IL device is driven with two distinct voltage pulse sources  $V_1$  and  $V_2$  shown in black and blue in Fig. 5 respectively. The resulting current through the device is measured and shown in red. This figure demonstrates that: repeated positive input, increases synaptic weight, increases the conductance of channels, applying two input voltage pulses simultaneously leads to a higher current through the device. These results contribute to the observation of behavior that is analogous to associative learning. When the device is driven with  $V_1=-10V$  alone initially, the measured current is  $-2.66mA$ . When  $V_1=V_2=-10V$  is applied simultaneously, current through the device increases as mentioned above. Then when  $V_1=-10V$  is applied alone

again, the measured current is 2.8mA, goes up to 2.84mA before it decreases to 2.78mA. This increase is due to the fact that the device has been conditioned to expect a second pulse simultaneously. Even though, it is only driven by  $V_1$ , the device behaves as if it is being applied  $V_1$  and  $V_2$  simultaneously and therefore the current through it is larger than it was when it was originally applied the same amplitude of the single input voltage.

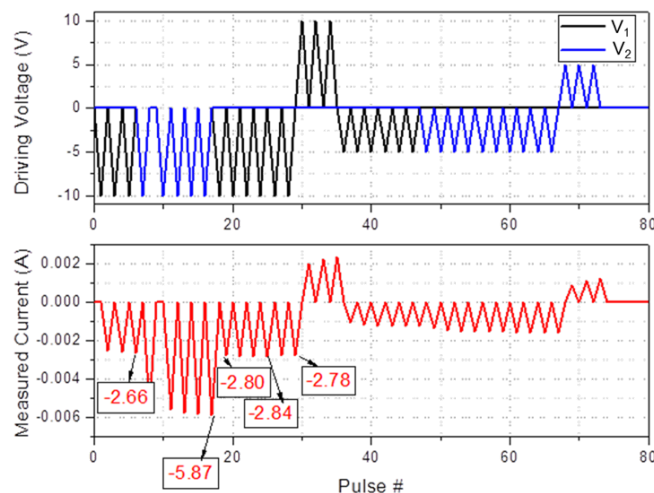


Fig. 5 The response of a 2-input terminal 1-output terminal flexible polymer substrate graphene/IL device to voltage pulses.

#### 4. Conclusion

The switching properties of IL were utilized in this work for the purpose of achieving memristive I-V characteristics. IL with graphene, on flexible polymer substrates yield flexible, low cost devices that are simple to assemble. We show in this work that these devices exhibit repeatable memristive behavior and that these switching qualities can be harnessed to demonstrate learning. Some key findings particular to these devices are that they exhibit pinched hysteresis loops which vary with frequency (higher frequencies lead to more linear behavior, lower frequencies widen hysteresis loops and lead to more nonlinear behavior). Secondly, these graphene/IL devices' conductance responds to positive and negative stimuli in the same way. Pulse train measurements demonstrate memory: repetitive pulses led to decreasing conductance and gradually increasing current output pulses. The two input terminal one output terminal device measurements point to associative learning, following simultaneous excitation from both terminals, the conductance decreases, after removing one of the voltages, the conductance increases again but once the single pulse is sent again, the device, expecting the second pulse simultaneously, becomes more conducting again.

The graphene/IL devices presented in this work are novel memristive devices which are different to CMOS compatible, semiconductor memristors. The measurement results demonstrate that the graphene/IL devices are very promising for further applications where devices can be trained with electrical signals and be made into heat or light sensitive devices to act as compact sensor/ processor units.

#### Acknowledgements

Itr Köymen acknowledges the partial support of this work by the Scientific and Technological Research Council of Turkey (TUBITAK) 2218 Scheme. Coşkun Kocabaş acknowledges the support from the European Research Council (ERC) Consolidator Grant ERC-682723 SmartGraphene.

#### References

- [1] P. Gkoupidenis, D. A. Koutsouras and G. G. Malliaras, "Neuromorphic device architectures with global connectivity through electrolyte gating," *Nature Communications*, vol. 8, p. 15448, 2017.
- [2] D. Khodagholy, J. N. Gelinias, T. Thesen, O. Devinsky, G. G. Malliaras and G. Buzsáki, "NeuroGrid: recording action potentials from the surface of the brain," *Nature Neuroscience*, vol. 18, pp. 310-315, 2015.

- [3] Y. Kim, A. Chortos, W. Xu, Y. Liu, J. Y. Oh, D. Son, J. Kang, A. M. Foudeh, C. Zhu, Y. Lee, S. Niu, J. Liu, R. Pfattner, Z. Bao and T.-W. Lee, "A bioinspired flexible organic artificial afferent nerve," *Science*, vol. 360, no. 6392, pp. 998-1003, 2018.
- [4] K. Oehkan, S. Razmkhah, P. Febvre, E. Zhitlukhina, Belogolovskii and M, "Investigating a Discrete Model of Memristive Systems," in *XIth International Scientific and Practical Conference on Electronics and Information Technologies (ELIT)*, Lviv, 2019.
- [5] K. A. Campbell, R. A. Bassine, M. F. Kabir and J. Astle, "An Optically Gated Transistor Composed of Amorphous M + Ge<sub>2</sub>Se<sub>3</sub> (M = Cu or Sn) for Accessing and Continuously Programming a Memristor," *ACS Appl. Electron. Mater.*, vol. 1, no. 1, pp. 96-194, 2019.
- [6] N. Raeis-Hosseini and J. Rho, "Solution-Processed Flexible Biomemristor Based on Gold-Decorated Chitosan," *ACS Appl. Mater. Interfaces*, 2021.
- [7] I. Köymen, P. A. Göktürk, C. Kocabaş and Ş. Süzer, "Chemically addressed switching measurements in graphene electrode memristive devices using in situ XPS," *Faraday Discuss.*, vol. 213, pp. 231-244, 2019.
- [8] T. F. Schranghamer, A. Oberoi and S. Das, "Graphene memristive synapses for high precision neuromorphic computing," *Nature Communications*, vol. 11, no. 1, 2020.
- [9] Z. Wang, L. Wang, M. Nagai, L. Xie, M. Yi and W. Huang, "Nanoionics-Enabled Memristive Devices: Strategies and Materials for Neuromorphic Applications," *Advanced Electronic Materials*, vol. 3, no. 7, p. 1600510, 2017.
- [10] E. O. Polat and C. Kocabas, "Broadband Optical Modulators Based on Graphene Supercapacitors," *Nano Letters*, vol. 13, no. 12, pp. 5851-5857, 2013.
- [11] N. Kakenov, O. Balci, T. Takan, O. V. A, H. Altan and C. Kocabas, "Observation of Gate-Tunable Coherent Perfect Absorption of Terahertz Radiation in Graphene," *ACS Photonics*, vol. 3, no. 9, p. 1531–153, 2016.
- [12] D. B. Strukov, G. S. Snider, D. R. Stewart and R. Williams, "The missing memristor found," *Nature*, vol. 453, pp. 80-83, 2008.
- [13] M. Kettner, I. Vladimirov, A. J. Strudwick, M. G. Schwab and .. T. Weitz, "Ionic gel as gate dielectric for the easy characterization of graphene and polymer field-effect transistors and electrochemical resistance modification of graphene," *Journal of Applied Physics*, vol. 118, no. 2, p. 02550, 2015.
- [14] V. K. Sangwan, H.-S. Lee, H. Bergeron, I. Balla, M. E. Beck, K.-S. Chen and M. C. Hersam, "Multi-terminal memtransistors from polycrystalline monolayer molybdenum disulfide," *Nature*, vol. 554, no. 7693, 2018.
- [15] C. Wu, T. W. Kim, T. Guo, F. Li, D. U. Lee and J. J. Yang, "Mimicking Classical Conditioning Based on a Single Flexible Memristor," *Advanced Materials*, vol. 29, no. 10, 2017.
- [16] B. Linares-Barranco, T. Serrano-Gotarredona, L. Camuñas-Mesa, J. Perez-Carrasco, C. Zamarreño-Ramos and T. Masquelier, "On Spike-Timing-Dependent-Plasticity, Memristive Devices, and Building a Self-Learning Visual Cortex," *Frontiers in Neuroscience*, vol. 5, p. 26, 2011.

# Characterization of Hydrophobic UV-Curable Acrylated Coating from Palm Oil Based Urethane Acrylate (POBUA) for Wood Coating Application

Nor Batrisya Ismail<sup>1</sup>, Ain Najiyah Jamaluddin<sup>1</sup>, Nurul Alia Norizham<sup>1</sup>, Nurul Hikmah Mohd Nor<sup>2</sup>, Norfazlinayati Othman<sup>2</sup>, Mohd Sofian Alias<sup>3</sup>, Khairul Azhar Abdul Halim<sup>3</sup>, Mahathir Mohamed<sup>3</sup> and Mohd Hamzah Harun<sup>3\*</sup>

<sup>1</sup>Chemistry Department, Faculty of Science, Universiti Putra Malaysia, 43400, Serdang, Selangor

<sup>2</sup>Physics Department, Faculty of Science, Universiti Putra Malaysia, 43400, Serdang, Selangor

<sup>3</sup>RadTech Malaysia, c/o Malaysian Nuclear Society, Radiation Processing Technology Division, Malaysian Nuclear Agency, Bangi, 43000, Kajang, Selangor

Corresponding author: hamzah@nuclearmalaysia.gov.my

## Abstract

Acrylated hydrophobic coating was prepared from palm oil based urethane acrylate (POBUA) by using the UV-curing technique. The purpose of the study was to investigate wetting properties and the application of this UV-curable palm oil resins for wood coating. Five different sample formulations were prepared that used nanosilica as the roughness agent, PFOA as the modifier and IC-500 as the photoinitiator. Surface contact angle and IR spectroscopy were characterized for each sample. IR spectroscopy confirmed the presence of POBUA resins in all samples. Nine hydrophobic coatings are obtained and the highest water contact angle value acquired is 116.29° which can be considered as a good hydrophobicity value for a wood coating application.

**Keywords:** acrylated hydrophobic coating, pobua, palm oil resin, uv-curable palm oil resin

## 1. Introduction

For the last few decades, bio-based polymers and resins have seen growing demands in industrial applications because of their potential reduced cost and environmental effect. When compared to traditional petroleum-based polymers, such polymers have numerous advantages and massive benefits towards green environment. Presently, Malaysia is known as the second largest producer and exporter of palm oil in the world after Indonesia. Global palm oil production increases tremendously in the past decades, almost doubling every 10 years (Khatun et al., 2017). Due to palm oil industry developing rapidly in Malaysia, it is taken as the subject for research and invention process.

Palm oil and its derivatives such as palm olein and stearin, have unsaturation levels that are half or less than half of that of soybean oil. As a result, it has never been considered as a suitable raw material for the production of resins. Nevertheless, it was interested in knowing the application of palm oil or its derivatives compared to linseed oil, soybean oil, and other oils. Materials from the palm oil products can be modified into radiation curable oligomers or resins, namely acrylated oils. Ibrahim et al. reported that the epoxidation of palm oil products produced compounds such as epoxidized palm oil products (EPOP) that can be used as a plasticizer and plastic stabilizer (Ibrahim et al., 1987). Acrylated palm oil is produced using the acrylation method, in which acrylic acid is inserted into the oxirane group of the EPOP. This method is similar to that used to produce epoxy acrylate (Husin et al., 1990). Palm oil based urethane acrylate (POBUA) can then be synthesized from the epoxidized palm olein acrylate (EPOLA) by isocyanation process. The potential application of POBUA is as a UV-curable palm oil resins for coating. UV-radiation curable coating is an environmentally friendly method that avoids or minimizes the emission of volatile organic compounds and harmful air pollutants. It is a fast-drying process that turns a reactive liquid chemical system into a non-tacky solid crosslinked at room temperature by using UV light to produce polymerization (Mehnert et al., 1998). This form of coating requires three components which are polymerizable resin, a photoinitiator, and a UV radiation source (Rosli et al., 2003). Since most radiation curable resins on the market today are derived from non-renewable, petroleum-based synthetic resins, there is an urgent need for developing new radiation curable resins based on renewable resources for wood coating, printing ink, and pressure sensitive adhesive applications.

In this study, the characteristics and wetting properties of UV-curable palm oil based urethane acrylate (POBUA) as a wood coating were investigated and discussed. The application of palm oil coatings in the current market is also evaluated. The goal for starting this study is to gain a better understanding of the explored system, which will be valuable for researchers working on developing this coating for technologically promising applications requiring hydrophobic property.

## 2. Materials and Method

### Materials

The chemicals used in this study were palm oil based urethane acrylate, POBUA (Nuklear Malaysia), 1H, 1H, 2H, 2H-Perfluorodecyl acrylate, PFOA namely, nanonanosilica, (Sigma), Irgacure-500, IC-500 and acetone. All chemicals were used as received.

### Preparation of resins formulations

The formulations of the resins involve four main materials which are POBUA as the oligomer, PFOA as the modifier or monomer, nanosilica as the roughness agent and IC-500 as the photoinitiator. All formulations have a fixed weight of POBUA which is 15g and photoinitiator was 5% of the total weight of POBUA. Meanwhile the compositions of PFOA and nanosilica were varied as shown in Table 1. The materials are mixed together by stirring the mixture at 200-250 revolutions per minute (rpm) using the mechanical stirrer until all the mixture are fully miscible. Then, the resins are left overnight at room temperature.

Table 1: Composition of SiO<sub>2</sub> and PFOA for the preparation of UV-curable film at fixed dose of POBUA and IC-184

Sample	POBUA content (g)	PFOA content %	Nanonanosilica content (%)	IC-500 content (%)
A	15	-	-	5
B	15	0.25	-	5
C	15	1.0	-	5
D	15	1.0	0.1	5
E	15	1.0	0.5	5

### Coating and UV-curing process

Figure 1 shows the coating and UV-curing process of the sample. Acetone was used to clean the substrate and bar coater before the coating process. All formulation samples were coated on a 7.4 x 6.4 cm wood substrate using a bar coater into a 250 μm thickness of film. The films were then exposed to UV radiation using IST UV radiation machine. The UV conveyor's speed was set at 10m/min for each pass and the current was at 7.5 Ampere. Each sample was passed for 2 times to be cured and the characteristics for each cured sample were analyzed.

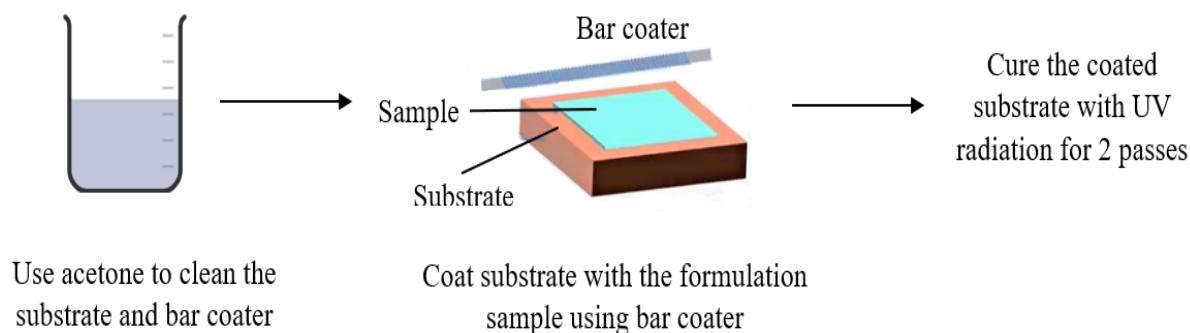


Figure 1: Coating and UV-curing of the sample

## Characterization

The properties of all cured films were studied from several tests. The thermogravimetric analysis (TGA) records the weight fluctuation, which the weight loss during heating as a function of temperature. Optical contact angle tests were performed on coating samples via Attention Theta Lite Optical Tensiometer (Biolin Scientific, TL 100) by sessile drop method. Fourier transform infrared (FTIR) spectra to determine the chemical bonds and molecular structure of cured samples. Meanwhile the gel contents test was done using Soxhlet method with acetone as the solvent. In each case a small mesh packet containing the sample was suspended vertically in the Soxhlet extractor such that it is lower than the siphon arm level. The solvent is then boiled for 20 hours. The films then were dried in a vacuum oven at 60°C and finally reweighed the films. The gel content was calculated as follow:

$$\text{Gel content, \%} = \frac{\text{Mass of sample after extraction, g}}{\text{Mass of sample before extraction, g}} \times 100$$

## 3. Results and discussion

### Water Contact Angle Studies

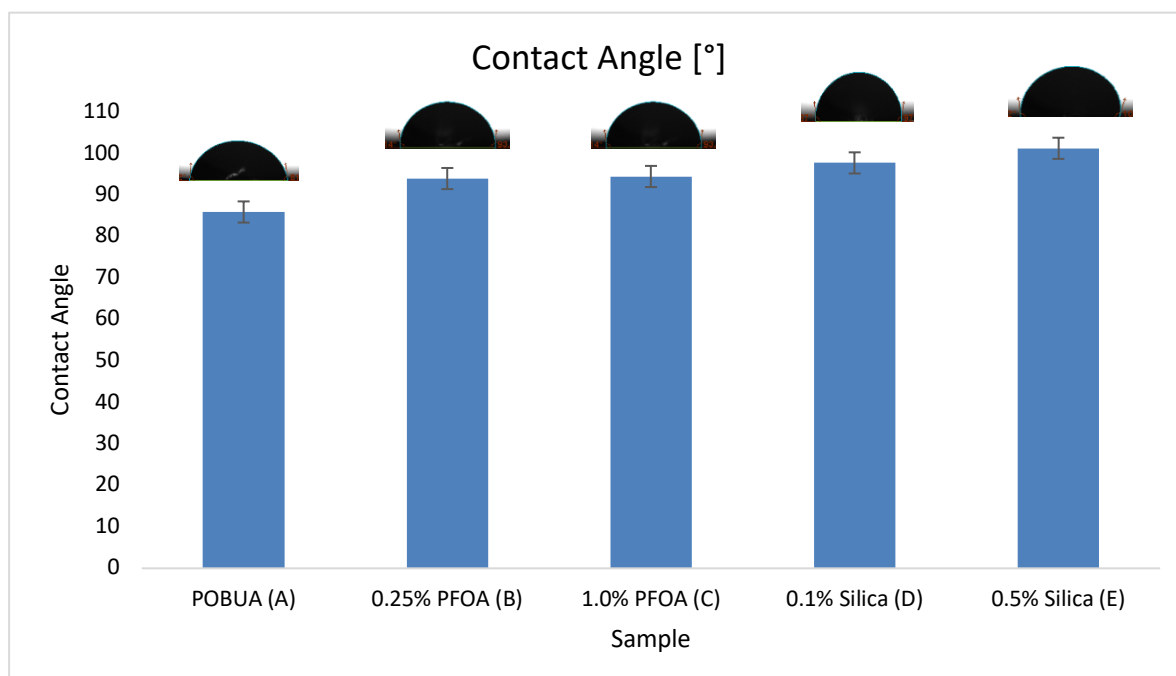


Figure 2: Contact angle for different POBUA formulations

Figure 2 shows the optical contact angle for the wood substrates that have been coated and cured with different POBUA formulations. From the figure, it can be summarized POBUA formulation showed the lowest hydrophobicity at 85.8° and it is due to the unavailability of any modifier and roughness agent (Harun et al., 2018). When POBUA was introduced with the 0.25% PFOA modifier, the coating exhibited hydrophobic properties with water contact angle obtained was 93.9°. When the modifier was increased up to 1.0%, the water contact angle slight increased at 94.4°. The formulations then were introduced with roughness agent which was nanonanosilica and the amount of nanonanosilica improved the hydrophobicity with water contact angle obtained for 0.1% Nanonanosilica was 97.64° and for 0.5% Nanosilica 101.1° respectively. In summary, an optimum composition for each component in the formulation is needed to obtain a higher value of surface hydrophobicity. For example, if the amount of nanosilica is increased, the amount of PFOA also need to be increased to compensate each other and then good hydrophobicity will be obtained and in turn improve the wood coating formulation.

### FTIR

FTIR analysis results in an absorption spectrum which provides information about the chemical bonds and molecular structure of a material. The chemical composition of different hydrophobic coatings coated on wood was studied by FTIR spectroscopy using ATR technique in transmission mode. The functional groups of

POBUA, nanosilica and PFOA were determined by FTIR spectroscopy and results are shown in Figure 3. The FTIR spectra of POBUA shows clearly strong band of CH<sub>3</sub> and CH<sub>2</sub> stretching at 2923 cm<sup>-1</sup> and 2853 cm<sup>-1</sup> respectively. C=O (carboxylic group) at 1727 cm<sup>-1</sup>. Absorption band at 1636 cm<sup>-1</sup>, 1409 cm<sup>-1</sup> and 809 cm<sup>-1</sup> ascribed to C=C stretching, scissoring and out-of-plane bending of the C=C of the vinyl moieties of the acrylate groups. Si-O-Si symmetric vibration mode is noticed at 1060 cm<sup>-1</sup> and 1068 cm<sup>-1</sup> for 0.5% Nanosilica in POBUA-SiO<sub>2</sub>, meanwhile C-F stretching shows at 1000 cm<sup>-1</sup> for the addition of 1% PFOA. The conversion of double bond that occurred within palm oil acrylate coating during the polymerization reaction under UV radiation was observed. The disappearance of the reactive C=C bond upon cured was detected at 1660-1600 cm<sup>-1</sup> and 809 cm<sup>-1</sup>. Before UV radiation, the FTIR spectrum showed unsaturation C=C bond peak at 1636 cm<sup>-1</sup>, 1409 cm<sup>-1</sup> and 809 cm<sup>-1</sup>. Due to the consumption of C=C of POBUA vinyl group in the curing reaction, no more traces for their IR bands detected after being cured (Saharudin et al., 2018).

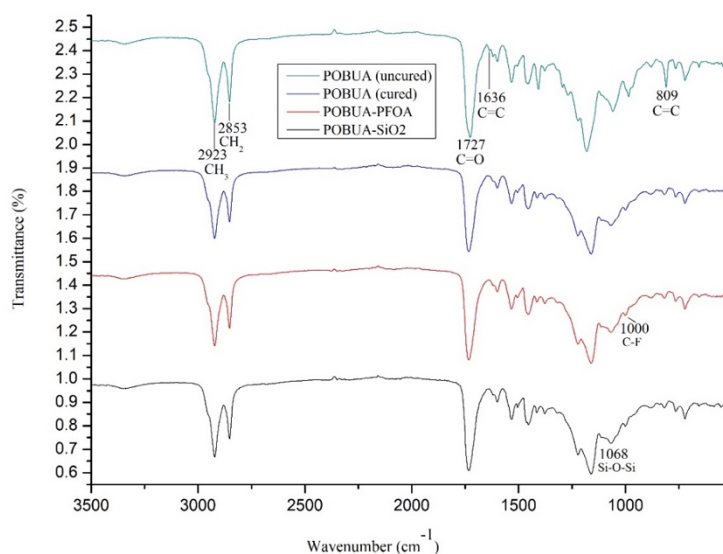


Figure 3: IR spectra of different acrylated POBUA formulations

### Degree of Crosslinking

Gel content allows the measurement of swell ratio which a measure of the degree of cross-linking in the gel phase. The film was extracted with acetone solvent to determine the crosslinked portion which the insoluble fraction that produced from the film. Table 2 tabulated the gel content percentage of UV-cured film for all compositions. The gel content of all UV-cured films increases with the increasing amount of nanosilica and PFOA. Furthermore, the crosslinking percentage of palm oil-based cured coating for all compositions was greater than 90%. This indicated that POBUA and the modifiers was compatible to each other (Nik Salleh et al., 2019).

Table 2. Gel content for different composition of hydrophobic coating surfaces at different passes of UV exposure

Samples	Gel Content (%)		
	3	6	10
POBUA	93.83	94.90	96.97
0.25% PFOA	94.83	98.55	99.10
1.0% PFOA	91.73	93.90	97.14
0.1% Nanosila	96.83	98.33	99.67
0.5% Nanosilica	93.10	94.52	97.01

### Thermogravimetric analysis (TGA)

Thermal properties of the POBUA coating films were evaluated by TGA. Figure 4 shows TGA thermograms of the POBUA coating surfaces. The thermograms for all surface coating exhibits a same degradation

temperature (Salih et al., 2015). TGA thermograms reveal that the decomposition of palm oil-based acrylate coating was two-stage degradation. The first stage occurred at the temperature range at 150°C, and can be attributed to the loss of the volatile compounds or the photoinitiator; The total weight loss at this stage (at the end of the stage at 208°C) was found to be around 4% of the total weight for POBUA with nanosilica and PFOA while POBUA with nanosilica and POBUA with PFOA film lost around 5% of its total weight. The onset temperature of this stage in POBUA films was 50°C. The major decomposition of the polymer films occurred in the second stage, which was attributed to the decomposition of the organic polymer chains. The onset temperature for this stage was 260°C for all surface coating. From 260 °C to 450 °C, the weight loss was dramatic decrease at ~85% and was attributed to the decomposition of the cured POBUA; the rest was the SiO<sub>2</sub> component and carbon.

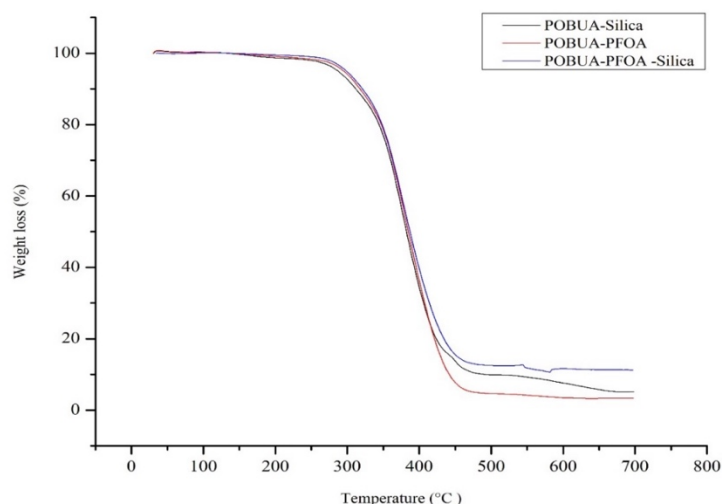


Figure 4: TGA thermograms of the POBUA coating formulations

## Conclusions

POBUA formulations with different compositions of SiO<sub>2</sub> and PFOA were successfully prepared along with the same composition of IC-500 in all samples. These formulations were successfully cured onto the wood substrate to obtain a coating using the UV-curing technique. Water Contact Angle test was conducted to identify the surface wetting properties of the cured POBUA samples. The samples containing nanosilica showed the highest water contact angle indicates the significant contribution of roughness agent in repelling water from being contacted with the coated surface. Based on the film properties, the palm oil acrylate coating was successfully cured as the peak for C=C disappeared after being cured. The results of gel content showed the percentage of cross-linking within the palm oil acrylate and the modifiers was more than 90%. These results proved the polymerization and crosslinking of the POBUA resins during the curing process. In conclusion, a hydrophobic acrylated coating from POBUA was successfully obtained by using the UV-radiation technique. From the analysis conducted, the POBUA resins can be a potential hydrophobic coating for wood applications in the industry.

## References

1. Harun, M. H., Talib, Z. A., Ibrahim, N. A., Chyi, J. L. Y., Salleh, N. G. N., Alias, M. S., & Othman, N. (2018). Characterization of transparent hydrophobic coating with nanosilica and graphene oxide fillers by sol-gel method. *International Journal of Nanoelectronics & Materials*, 11(3).
2. Hussin et. al., (1990). *Jurnal Sains Nuklear Malaysia*, 8(2), 149-155.
3. Ibrahim, M., Leong, Y. C., Ong, E. L., & Salmiah, A. (1987). Potential applications of expoxidized palm oil in plastics and rubber industries. In *International Oil/Palm/Palm Oil Conferences. Progress and Prospects.(Technology) Proceedings June 29-July 1 Kuala Lumpur (No. L-0115)*. PORIM.
4. Khatun, R., Reza, M. I. H., Moniruzzaman, M., & Yaakob, Z. (2017). Sustainable oil palm industry: The possibilities. *Renewable and Sustainable Energy Reviews*, 76, 608-619.
5. Mehnert, R., Pincus, A., Janorsky, I., Stowe R., & Berejka, A. (1998). *UV and EB Curing Technology and Equipment*, London: Wiley/SITA.

6. Nik Ghazali Nik Salleh, Khairul Azhar Abdul Halim, Mek Zah Salleh, Nurul Huda Mudri, Mohd Sofian Alias, Mohd Hamzah Harun, Rida Tajau, Sharilla Muhammad Faizal, and Rosley Che Ismail, Development of Radiation Curable Overprint Varnishes Based on Palm Oil Acrylate Resin, Konferen RadTech Asia 2019, 17-20 Okt 2019, Hangzhou, China.
7. Rosli, W. W., Kumar, R. N., Zah, S. M., & Hilmi, M. M. (2003). UV radiation curing of epoxidized palm oil–cycloaliphatic diepoxide system induced by cationic photoinitiators for surface coatings. *European Polymer Journal*, 39(3), 593-600.
8. Saharudin, K. A., Sreekantan, S., Basiron, N., Chun, L. K., Kumaravel, V., Abdullah, T. K., & Ahmad, Z. A. (2018). Improved super-hydrophobicity of eco-friendly coating from palm oil fuel ash (POFA) waste. *Surface and Coatings Technology*, 337, 126-135.
9. Salih, A. M., Ahmad, M. B., Ibrahim, N. A., Dahlan, K. Z. H. M., Tajau, R., Mahmood, M. H., & Wan, Z. (2015). Synthesis of radiation curable palm oil–based epoxy acrylate: NMR and FTIR spectroscopic investigations. *Molecules*, 20(8), 14191-14211.

# Optimization of the Optical Characteristics of a Multilayer Coating with Thin Films of Germanium Telluride

E. Pritotskii, M. Pankov

Laboratory of neuromorphic optical systems, Institute on Laser and Information Technologies  
of Russian Academy of Sciences, Shatura, Moscow region, Russia  
egorslim@gmail.com

## Abstract

A model of a multilayer optical coating with a four-level transmission coefficient has been developed. Based on the calculated data the values of the thicknesses were determined, at which the greatest change in the transmittance occurs for modulated optical radiation at a wavelength of 1550 nm. Experimental samples of coatings with thin films of GeTe and antireflection films of ZnS have been prepared and their optical transmission characteristics have been investigated. Combinations of the parameters of multilayer structures for the implementation of contrast levels of transmission have been determined. The results of the study represent the implementation of a multilevel weight function based on thin film of phase-change materials for artificial optical synapse.

**Keywords:** multilayer coating, phase-change material, optical synapse, neuromorphic system

## 1. Introduction

The most promising are information systems that combine the processes of storing and processing information. Artificial neuromorphic systems are built on these principles, in which neurons are connected by synapses [1]. Synapses have the form of scalar weights, the values of which affect the activation of the neuron (Fig. 1).

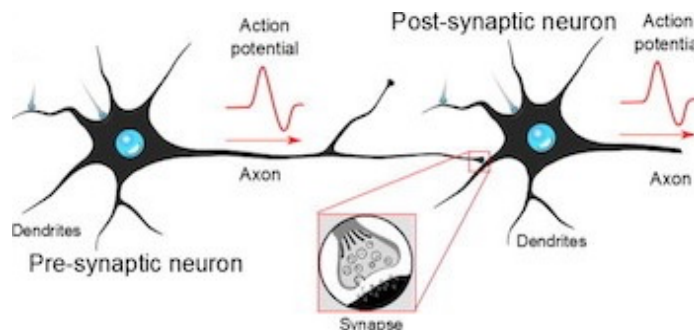


Fig. 1: Neural communication across the synapse

The development of neuromorphic processors is carried out in the direction of increasing the levels of registration of the weight coefficient at the synapse by software algorithms, where the weighting factor is written in four integers in one artificial synapse, and the computing core is implemented using classical semiconductor technology [2]. Another way to improve recording is to use materials that change their electrical and optical properties when exposed to heat. Nonvolatile memory technology is realized through reversible phase transitions in thin films of chalcogenide materials and allows reproducing several levels of electrical conductivity [3]. The advanced development of neuromorphic systems is possible due to the transition to optical computational technologies, including due to laser induction of materials with a phase transition. Optical synapses are technologically implemented on fibers [4] or planar waveguides [5], where the main principle of the device is high-speed modulation of transmission.

## 2. Model

Chalcogenides are one of the phase change materials for neuromorphic applications. As an example, we have chosen the well-studied compound of germanium telluride (GeTe). Due to the high absorption in the visible range, laser induction of thin GeTe films is possible by pulsed sources with a wavelength in this range. Modulation wavelength is in the C-band due to the low value of the extinction coefficient for an amorphous GeTe film (Fig. 2).

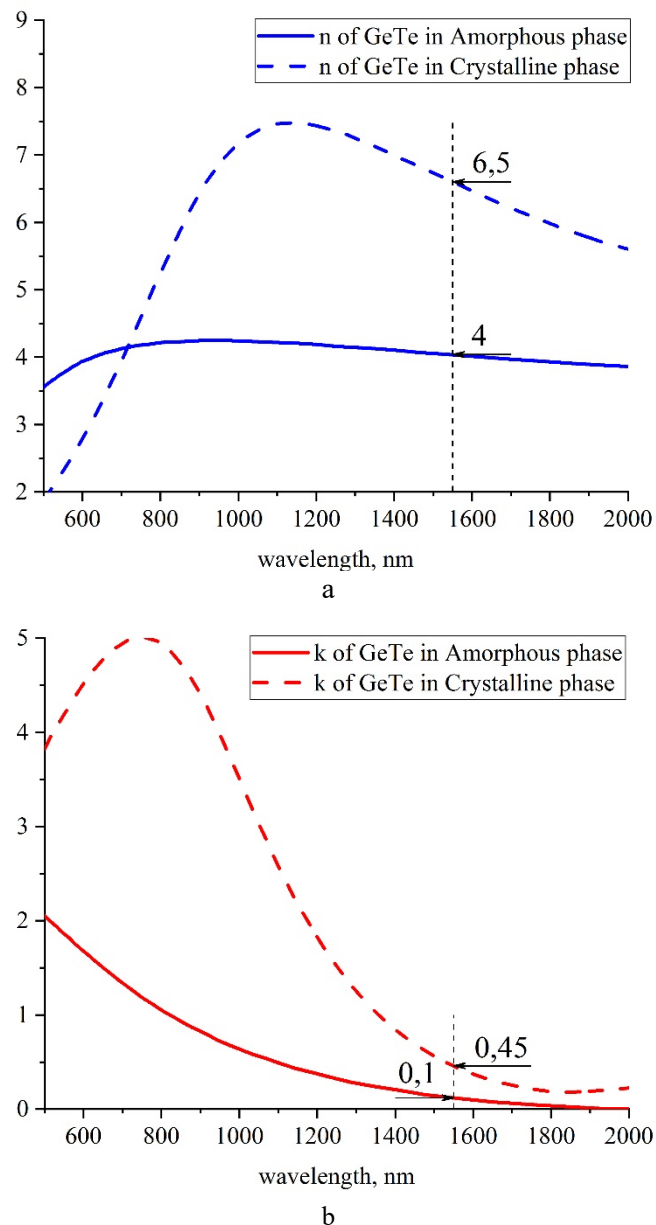


Fig. 2: Complex refractive index of GeTe film, a - refractive index, b - extinction coefficient [6].

Measurement of the optical properties of thin films made of phase change materials by photometric and ellipsometric methods allows to optimize various parameters of multilayer structures using software methods for calculating the optical characteristics of reflectance, transmittance and absorption [7]. The initial data are the dependences of the refractive index and the extinction coefficient on the wavelength. The refractive index of the GeTe film increases after crystallization and the reflection coefficient at the boundaries with silicon dioxide (SiO<sub>2</sub>) waveguides can reach 50% due to the difference in refractive indices. And the extinction coefficient of the

GeTe film increases too. The Fig.3 shows the calculated dependences of absorption on the thickness of the GeTe film in two states.

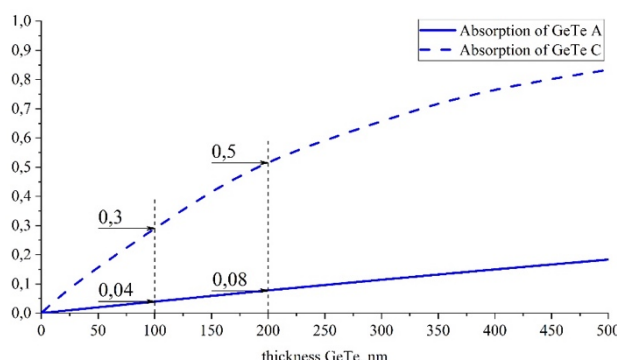
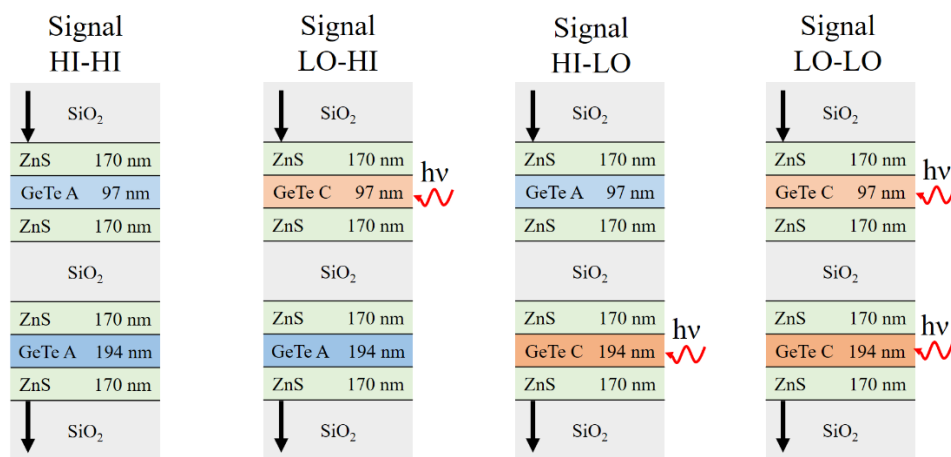


Fig. 3: Calculated dependency of absorption of a GeTe film for the thickness in the amorphous (GeTe A) and crystalline phases (GeTe C) based on the extinction coefficient

The thickness of the GeTe films is selected based on the calculated absorption in the crystalline state. To minimize reflectance, we used antireflection layers of zinc sulphide (ZnS). This approach will reduce the required energy density of the initiating laser radiation and increase the contrast of the transmission levels for the modulated optical signal. The first structure with an amorphous film GeTe of 97 nm and antireflection layers ZnS of 170 nm provides a transmittance of 95%. Upon transition to the crystalline state, the absorption increases and the transmittance decreases to 65%. The second structure an amorphous film GeTe of 194 nm and antireflection layers ZnS of 170 nm transmits 90%, but during the phase transition, the absorption increases even more, and the transmittance decreases to 42%. The combination of such structures and laser induction of individual GeTe films gives us four levels of contrast transmission (Fig. 4). This model will ensure the reproducibility of the transmittance values during multiple cycles of recording the weight coefficient into an artificial optical synapse.



$$T_1 = T_{1A} \times T_{2A} = 0,87 \quad T_2 = T_{1C} \times T_{2A} = 0,58 \quad T_3 = T_{1A} \times T_{2C} = 0,37 \quad T_4 = T_{1C} \times T_{2C} = 0,24$$

Fig. 4: Four calculated constructions with contrast transmittance T.

### 3. Experiment

We have obtained antireflection amorphous GeTe films with antireflection layers of ZnS by sputtering in a vacuum at a temperature of 130 °C. We heated individual samples in a vacuum at a temperature of 300 °C for three hours to obtain a reference crystalline phase. The measured optical characteristics of the obtained structures differ for two thicknesses of GeTe films and their phase state in accordance with the calculation model. Combinations of these structures provide four contrast levels of transmittance (Fig. 5).

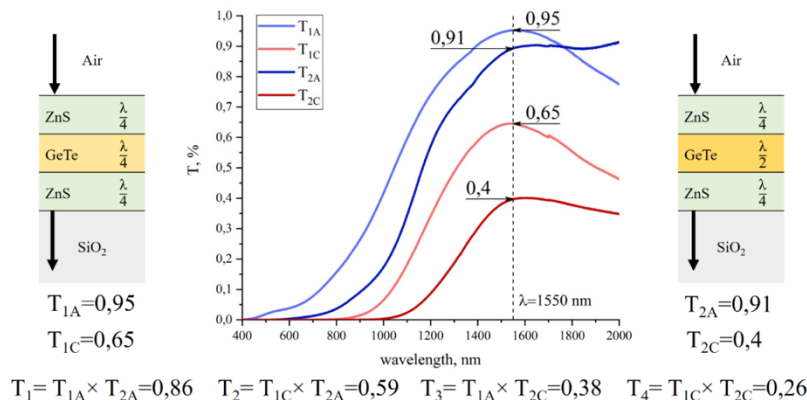


Fig. 5: Optical characteristics of the fabricated three-layer structures and the corresponding transmittance levels of combinations of these structures.

This approach will make it possible to technologically implement a two-bit optical synapse. The switching rate depends on the rate of change in the phase state in thin films of germanium telluride and the parameters of laser radiation.

#### 4. Conclusion

To create an artificial optical synapse, it is necessary to ensure minimum reflectance losses, signal contrast, high switching speed with a simple design based on proven technologies. Calculation of the optical characteristics of thin films of GeTe in multilayer structures makes it possible to create models of multilayer coatings with a four-level transmission coefficient. The calculated data were used to determine the thicknesses for the antireflection layers of ZnS, equal to 170 nm, and the thicknesses of GeTe films, equal to 97 and 194 nm, at which the greatest change in transmittance occurs for modulated optical radiation at a wavelength of 1550 nm. The optical characteristics of experimental samples of coatings of GeTe films with antireflection ZnS layers demonstrated similarity with the calculation model. The results of the study will make it possible in the future to implement multilevel switching of transmittance for modulating an optical signal at fast reversible laser-induced phase transitions in phase-change materials.

#### Acknowledgements

This work was supported by RFBR Grant No.19-29-12024/19 in part of the synthesis of thin films with phase change materials, Grant No. 075-15-2019-1950 of the Ministry of science and higher education of Russian Federation in part of the analysis main properties of basic elements for neuromorphic optical systems, and within the State assignment FSRC «Crystallography and Photonics» RAS in part of the study of optical properties of multilayer structures.

#### References

1. Zhang, W. Designing crystallization in phase-change materials for universal memory and neuro-inspired computing / W. Zhang, R. Mазzarello, M. Wuttig, E. Ma // Nature Reviews Materials. – 2019. – Vol. 4, Issue 3. – P. 150-168.
2. Merolla, P.A. A million spiking-neuron integrated circuit with a scalable communication network and interface / P.A. Merolla, J.V. Arthur, R. Alvarez-Icaza, A.S. Cassidy, J. Sawada, F. Akopyan, B.L. Jackson, N. Imam, C. Guo, Y. Nakamura, B. Brezzo, I. Vo, S.K. Esser, R. Appuswamy, B. Taba, A. Amir, M.D. Flickner, W.P. Risk, R. Manohar, D.S. Modha // Science. – 2014. – Vol. 345, Issue 6197. – P. 668-673.
3. Ahmanathan, A. Multilevel-cell phase-change memory: A viable technology / A. Athmanathan, M. Stanisavljevic, N. Papandreou, H. Pozidis, E. Eleftheriou // IEEE Journal on Emerging and Selected Topics in Circuits and Systems. – 2016. – Vol. 6, Issue 1. – P. 87-100.
4. Gholipour, B. Amorphous metal-sulphide microfibers enable photonic synapses for brain-like computing / B. Gholipour, P. Bastock, C. Craig, K. Khan, D. Hewak, C. Soci // Advanced Optical Materials. – 2015. – Vol. 3, Issue 5. – P. 635-641

5. Cheng, Z. On-chip photonic synapse / Z. Cheng, C. Ríos, W.H.P. Pernice, C.D. Wright, H. Bhaskaran // *Science advances*. – 2017. – Vol. 5, Issue 9. – P. e1700160. – DOI: 10.1126/sciadv.1700160.
6. Wuttig, M. Phase-change materials for non-volatile photonic applications / M. Wuttig, H. Bhaskaran, T. Taubner // *Nature Photonics*. – 2017. – Vol. 11, Issue 8. – P. 465-476.
7. Arakelyan, S.M. Modeling of sizes of coefficients of reflection and transmission for multilayered coatings / S.M. Arakelyan, O.Y. Butkovskiy, A.A. Burtsev, S.L. Lysenko, M.A. Pankov, E.M. Pritotskiy, A.P. Pritotskaya // *Computational nanotechnology*. – 2017. – Issue 4. – P. 14-20.

## Innovative virtual approach for treatment of fears and enhancement of cognitive abilities

Giuseppe Scavone<sup>1</sup>, Debora Benatti<sup>1</sup>, Maria Donadio<sup>1</sup>, Antonio Ruoto<sup>2</sup>, Diego Carmine Sinitò<sup>2</sup>, Emilio Massa<sup>2</sup>, Vito Santarcangelo<sup>2</sup>

<sup>1</sup> Centro Rham Srl

Via I Maggio 60, Matera, Italy, [info@rham.it](mailto:info@rham.it)

<sup>2</sup> iInformatica Srl

Corso Italia 77, Trapani, Italy, [info@iinformatica.it](mailto:info@iinformatica.it)

### Abstract

Research and development activities carried out by Centro Rham Srl together with innovative SME iInformatica concerned the design and experimental prototyping of innovative sceneries for the treatment of fears using virtual reality headsets in conjunction with the use of binaural audios and biofeedback-monitoring devices. This wearable device is a prototypical headset that allows to manage sceneries together with audios characterized by pink noise (relaxing) components and binaural beats (alfa, theta, delta) aimed at a therapeutical treating of phobias. Thanks to spectrogram analysis it is possible to understand the frequency and intensity components that characterize a certain acoustic stimulus, with the aim, together with a tactile/visual aid, to evoke a cognitive response. Biofeedback is acquired and monitored in real time using more wearable sensors. Research also concerned digital sceneries and tactile devices prototyping for an upgrade of cognitive abilities. This prototypical acoustical-sensorial experience is given by the union of binaural audios focused on the improvement of mnemonic abilities together with the use of cards and of an haptic pneumatical matrix to stimulate different cognitive functions of orientation (temporal and spatial), attention (visive and tactile), memory (visuospatial, visive-for related objects, episodic and associative), logic and reasoning (correlation with acoustic and tactile inputs). Furthermore, the spectrogram analysis is fundamental for lexical and phonetic analysis.

**Keywords:** biofeedback, acoustic experience, fear treatments, binaural beats

### 1. Introduction

This Paper aims to introduce the potential of audio analysis tools (both spectral and its components) with a particular focus on the properties of binaural audio [8], particularly used for meditation purposes, and to induce sensations in the listener. In order to introduce the concept of audio waveform, it is necessary to point out that the human ear perceives sounds in the range between 20 Hz and 20 KHz. Such a range characterizes the frequency responses of commercial earphones, consequently these sound output devices will be the instruments targeted by our acoustic investigation activity, thanks also to the possibility of managing acoustic stereo channels. Frequency is the number of repetitions (cycles) of vibrations made in one second, and is measured in Hz (one hertz is equivalent to one pulse per second). If a sound wave repeats 50 times per second it will have a frequency of 50 Hertz.

The spectrum of audible audio frequencies is divided into three categories: low, medium, and high:

1. 1 – 20 Hz: Non-perceivable subsonic frequencies
2. 20 – 60 Hz: Sub-low
3. 60 – 250 Hz: Low
4. 250 – 500 Hz: Medium-low
5. 500 Hz – 2.500 Hz: Medium
6. 2.500 – 5.000 Hz: Medium-high
7. 5.000 – 20.000 Hz: High
8. > 20.000 Hz: Ultrasounds, not perceivable by humans

It is therefore possible to reproduce sub-low sounds for the human ear using earphones. The sound pressure level (SPL) is the pressure change generated by the headphones in relation to the intensity of a sound and is measured in decibels (dB SPL). The intensity of a sound represents the vibration amplitude, that is the variation of the sound wave from the zero-base line, that is not sound (0 dB). The greater the amplitude of the sound wave the

louder and more audible the sound will be, on the contrary the lower the amplitude at the same frequency the weaker the sound will be. The threshold of pain is set at 130 dB.

Considering the frequency ranges of the human brain, they have been divided into 5 frequency ranges:

- \* gamma (30 > 70 Hz): are rare and emitted during states of ecstasy, compassion and deep inspiration;
- \* beta (14 > 30 Hz): are very typical, emitted during normal daily activities;
- \* alpha (8 > 13,9 Hz): are those emitted when we daydream or are intensely inspired and focused in creative activities;
- \* theta (4 > 7.9 Hz): are present during the REM phase of sleep, when we are dreaming;
- \* delta (0,1 > 3,9 Hz): are released during deep sleep.

It is therefore evident that, considering a 'sound-brain wave' correlation, it is impossible to reproduce sounds in the delta-alpha range. It is instead possible to emit and listen to continuous sounds in the beta and gamma audible range.

However, using the rhythm it is possible to induce waves in any desired range. The repetition of tones at regular intervals (Hz) is called isochronic beat and is characterized by intermittence. It is one of the simplest methods of neuro-acoustic stimulation and represents one of the most immediate systems of induction, realizable in the form of rhythm at regular intervals. The low tones (range 150 - 180 Hz) are particularly suitable for such induction (isochronic frequency on audible carrier). A possible solution to tone generation in subsonic frequencies (that coincides with the delta-theta-alpha ranges) is represented by the theory of binaural beats. Binaural beats are beats that are perceived by the brain when two sounds with a frequency below 1500 Hz and a difference of less than 30 Hz are heard separately through earphones. It is important to point out that these beats are not a consequence, as it normally happens, of a physical superposition of sound waves (which is impossible using earphones), but are generated directly in the brain. This phenomenon was identified in 1839 by Heinrich Wilhelm Dove. Human auditory frequencies are approximately restricted to perception in the range between 20 and 20 000 Hz, while the frequencies detected for cognitive brain activities are below 30-40 Hz, making natural input through hearing of frequencies near or below the lower human acoustic threshold difficult or impossible. In order to trigger such frequencies, for example on 10 Hz as the Alpha waves normally detected in the phases of relaxation, it is usually applied a beat of 315 Hz in one ear and a beat of 325 Hz in the other, so that the brain generates a third beat with a frequency of 10 Hz. An alternative to binaural tones is Monaural Beats, which are similar to Binaural beats, with the difference that the two carrier tones are mixed before being sent to the ear. When two slightly different beats, appropriately interwoven into a single low-intensity sound, are submitted to the same ear, the brain processes and perceives a third beat equivalent to the difference of the two beats heard. It is a very effective technique and does not require the use of stereo headphones. However, unlike binaural beats, they need amplitude (higher volume) and can be less pleasant to listen to. The purpose of this research work is to carry out a review of the documentation on this phenomenon, addressing the aspects of binaural audio with therapeutic and marketing of materials purposes, introducing experimental development prototype concrete applications, developed by innovative SME iInformatica in the research and development paths carried out with the Centro Rham S.r.l. company.

## **2. Binaural beats**

A common format of a spectrogram is a graph with two geometric dimensions: one axis (e.g., the abscissa) represents time and the other axis represents frequency; a third dimension indicates the amplitude of a particular frequency at a particular time, and is represented by the intensity or colour of each point in the image. A spectrogram is thus represented as a "heat map", that is, as an image where the intensity is shown by varying the colour or brightness.

However, it is often quite difficult to interpret the spectrogram on a linear scale. A useful solution for the representation of audio waveforms is to change the scale used to represent frequencies, so that equal frequency intervals no longer correspond to equal intervals on the x-axis. This corresponds to using a non-linear scale, that is a scale for which the distances are related to the magnitude to be represented by means of a non-linear relationship. One of the most widely used nonlinear scales is the logarithmic scale. In music, the presence of gamma components are often found in songs, continuously or isochronously associated with rhythm. The analysis of the spectrogram of pink and white noise is particularly interesting. The spectrogram of applause is a classic

example of pink-white noise, a symbol of expression of chorality and similar to that of sea waves (pink noise) or hair dryer.

Among the state-of-the-art reference software there is the Brainwave Generator software.

The possibility of having a dynamic binaural beat is particularly interesting, so as to have a decrease/increase of the functional frequency to the state to be induced. This is particularly common in the documentation in order to gradually move from a state of initial clarity (beta) to a state of relaxation (alpha/theta).

As mentioned in the introductory paragraph, binaural beats are the result of two sounds with a frequency of less than 1500 Hz and a difference of less than 30 Hz, which are heard separately through earphones and generated directly in the brain. These sounds have been the topic of numerous scientific publications. The following is a brief documentation review on the subject.

In the paper [1] patients who underwent listening prior to cataract surgery showed a decrease in surgical anxiety using audio treatment at 20 Hz for the first 5 minutes and then for 55 minutes at 10 Hz.

The paper [2] shows as a case study the stimulation of people with binaural beats at a frequency of 9.55 Hz. This showed an improvement in WMC (working memory capacity). An important confirmation of the possibilities to improve problem solving using binaural audio comes from the paper [3].

The paper [4] shows important correlations between listening to binaural audio and EEG signals.

In the paper [5], cognitive enhancement effects were found in the presence of monoaural and binaural beat stimulation. By using a neuro-feedback device to transmit impulses, it is possible to see how a rhythmic impulse is received by the brain in the form of an electrical impulse. This phenomenon is known as FFR (Frequency Following Response).

### **3. Case study on cognitive enhancement and treatments of fears**

The research and development activities carried out by Centro Rham Srl [7], together with the innovative SME iInformatica, concerned the design and experimental prototyping of innovative scenarios for cognitive enhancement, orthoptic treatment, treatment of fears through the use of virtual reality visors in conjunction with the use of binaural audio and biofeedback monitoring devices. The wearable device is a prototype visor that allows interactive scenarios to be administered together with audio characterised by pink noise components (relaxing) and binaural beats (alpha, theta, delta) targeted to the therapeutic treatment of phobias. By analysing the spectrogram, it is therefore possible to understand the intensity and frequency components that characterise a given acoustic stimulus with the aim of evoking a cognitive response, together with tactile/visual support. Biofeedback is acquired and monitored in real time via additional wearable sensors.

Considering the treatment of phobias, it is possible to verify the level of neurofeedback (EEG) of the user during the administration of virtual reality scenarios related to a particular phobia, together with the use of binaural audio that have the purpose of managing anxiety using theta-type frequencies, typical of meditation. Using a neuro-feedback device (wearable EEG) it is then possible to detect trends of gamma, beta, alpha, theta and delta waves in relation to the visual-acoustic stimulus presented. The research also involved the prototyping of digital scenarios (Introspecto) and tactile tools (Box Ricorda) for the enhancement of cognitive skills. The Introspecto software aims to objectively evaluate selective attention and visual sustained attention, verifying the contribution of the administration of binaural audio in terms of improved performance. The HMI can be used both via tablet and visor, in order to perform appropriate orthoptic evaluations. Box Ricorda [6] is a further deliverable of the research, and represents a prototypal acoustic-sensorial experience given by the evaluation in terms of cognitive improvement through the administration of binaural audio aimed at the enhancement of memory skills, together with the use of cards and a haptic matrix for the stimulation of different cognitive functions of orientation (temporal and spatial), attention (visual and tactile), memory (visual-spatial, visual-object related, episodic and associative), logic and reasoning (correlation with acoustic and tactile input).



Fig. 1: The figure shows virtual reality devices combined with binaural audios for the treatment of phobias and to an improvement of cognitive abilities monitored through neuro-feedback (left) and the Ricorda box, implemented experimental prototype (right).

#### 4. Conclusion

The purpose of the paper is to present the potential of binaural beats through the analysis of waveforms, the state of the art and prototypes created during the research and development activities carried out by the innovative SME iInformatica together with Centro Rham (in the area of health care and therapy). This overview shows how important this technical-scientific field can be for the design and implementation of new solutions in many different scenarios. The methods and systems presented are protected by industrial patents. We hope this reading was interesting and may open up opportunities for dialogue and comparison for new interesting solutions and applications.

#### Acknowledgements

Authors would like to sincerely thank Michele Di Lecce, Nicolò Montesano, Saverio Crisafulli, Giulio Setzu and Gianluca Signore for the support in the experimental development and drafting of the paper

#### References

1. D. Wiwatwongwana, “*The effect of music with and without binaural beat audio on operative anxiety in patients undergoing cataract surgery: a randomized controlled trial*”, PMC, 2016
2. J. Kraus, “*The effect of binaural beats on working memory capacity*”, Studia Psychologica, 2015
3. B. Hommel, “*High-Frequency Binaural Beats Increase Cognitive Flexibility: Evidence from Dual-Task Crosstalk*”, Psychol, 2016
4. V. Sharma, “*Effect of Binaural beats on brain EEG signals – A study*”, SCITSE 2017, 2019
5. H. Engelbregt, “*The Effects of Binaural and Monoaural Beat Stimulation on Cognitive Functioning in Subjects with Different Levels of Emotionality*”, Adv Cogn Psychol, 2019
6. G. Scavone, “*Uno strumento ludico-formativo volto alla stimolazione sensoriale e al supporto per lo stimolo e il recupero di alcune funzioni cognitive*“, UIBM. Patent P. n. 202020000007130, 2020
7. G. Scavone, “*Intelligent systems to support patients*“, ASA, 2019
8. L. Goes (2008), “*Binaural beats: Brain wave induction and the use of binaural beats to induce brain wave patterns*“, Pulsus, 2008

# Surface Coatings for Small Aircraft Brakes Application

Marco Granata and Francesco Bellucci \*

CRdC Tecnologie Scarl, Via Nuova Agnano 11, 80125 Napoli, Italy  
marcogranata1993@gmail.com1\* Corresponding author

## Abstract

The rapid development of additive manufacturing technologies has improved the choice of materials in various industrial sectors, specifically relating to friction materials for brakes application in the aeronautical sector. Currently, materials for aircraft brakes range from the low-cost sintered friction pad/liner material vs sintered rotor disc material to the high-cost carbon fiber material vs carbon fiber material. The subject of this paper was developed in the framework of a European project (E-BRAKE). One of the objects of this scientific research regards the potential use of thermal spray additive manufacturing technologies to produce a thin film of friction material onto low-carbon steel surface to allow its use as potential composite material for brake units.

In this research friction composite surface coatings were deposited with two different thermal spray additive manufacturing technologies, respectively the High Velocity Oxygen Fuel (HVOF) and the Atmospheric Plasma Spraying (APS), for the purpose of creating high friction and wear resistance composite surface coatings onto low-carbon steel surface. Tribological properties (friction coefficient and wear rate), thermal conductivity, and diffusivity as well as metallographic structures and adhesion to the low-carbon steel surface of these surface coatings were evaluated to assess their potential use as brake materials.

**Keywords** Additive Manufacturing Technologies, High Velocity Oxygen Fuel, Atmospheric Plasma Spraying, Composite surface coatings, Wear-resistance surface coatings, Friction material coatings

## 1. Introduction

The object of our study is related to materials for small aircraft brake application. A brake is a mechanical device that inhibits motion by absorbing energy from a moving system. It is used for slowing or stopping a moving vehicle most often accomplished by means of friction. A typical multi-disk aircraft brake is schematically shown in Figure 1. As can be seen in this figure, the brake consists of series of discs; the stators, which are stationary units connected to the wheel axle or leg, and the rotors, which form the rotating part, connected to the wheel. Under the action of hydraulic pressure, these series of discs get compressed, forcing the wheel to slow down due to friction. The discs are typically provided with slots for better heat dissipation at high temperature. During the braking action, the brake is activated by the hydraulic system pressure, which compresses the heat stack. In this way, the rotors and the stators are squeezed together by hydraulic pistons and the brake produces torque by virtue of friction forces generated at the rubbing interface between the rotors and the stators.

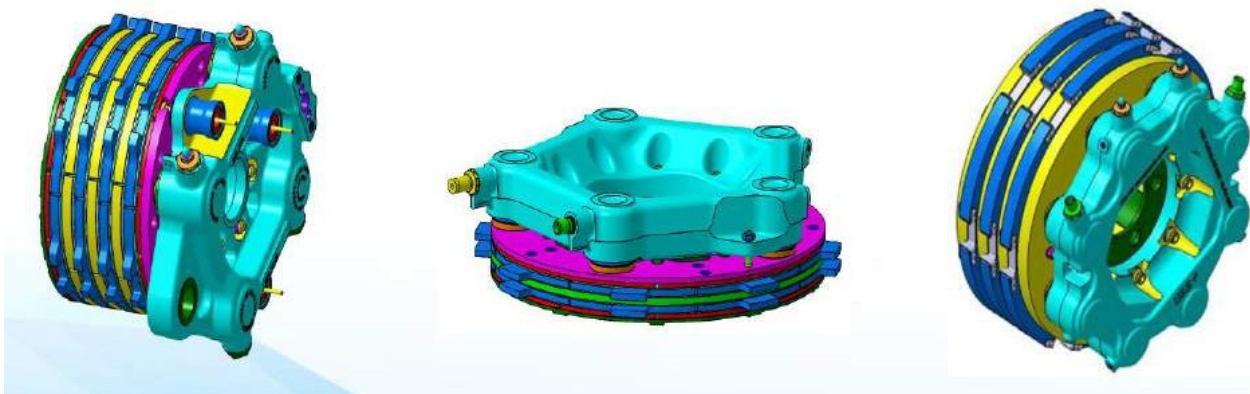


**Figure 1.** Aircraft brake system.

In a recent report of Umbria Aerospace System (UAS), [1] a scenario of the materials usually adopted for A/C braking system design for small aircraft is discussed. Friction material selection is based on the following main aspects:

- Weight requirements. Wheel brake assembly total weight is one of the key points and guideline on

friction material selection.

- System performance requirements. Dynamic braking performance (maximum temperature, dynamic friction coefficient, dynamic braking pressure, friction material wear rate) and parking condition performance (static friction coefficient, parking pressure)
- Cost aspects. The selection of friction material has a direct implication on cost aspects. Both non recurrent and recurrent costs, including scheduled maintenance costs, drive the selection.
- Maintenance aspects

Considering the main criteria three different solutions underlining advantages and disadvantages for each solution are reported:

- Sintered friction material VS steel
- Sintered friction material VS Sintered friction material
- Carbon fiber material VS carbon fiber material

In the first configuration either stator and rotor are made in steel (carbon steel or stainless steel) and only stator or rotor discs are equipped with a thin film of friction material. Two types of sintered material are usually implemented: Iron based sintered material and copper based sintered material. Both solutions are characterized by a good dynamic friction factor. Friction factor decreases for increasing temperature. Mean dynamic friction value in normal braking condition is equal to about 0,21-0,23. In high energy condition, where maximum temperature reaches 800÷900 °C, friction factor becomes equal to 0,18-0,20 (reduction up to 16-18%). Maximum operating temperature allowed is below 900÷950 °C. Temperature higher than the specified one may cause thermal distortion of the discs and degradation of the mechanical properties of the disc material. Heat sink mass relevant to this configuration is very high if compared with heat sink mass relevant to carbon fiber solution. Heat sink mass is related to material specific heat (about 600-620J/(kg\*K) in high energy condition) and material density (equal to about 4,8kg/dm<sup>3</sup> for sintered friction material and equal to 7,8kg/dm<sup>3</sup> for steel). Static friction factor, adopted for parking condition, is usually above 0,32-0,35 (high static friction factor). Parking condition is assured applying a low pressurization. Usually parking condition is verified without particular problems. Wear parameter, defined as ratio between wear material and kinetic input energy is variable from 1,10 and 1,35 grams/MJ. Number of allowed braking is lower than carbon fiber disc solution.

**Table 1.** Sintered material coating vs Steel Properties

Sintered material VS steel	
Design Parameter	Rating
Dynamic Friction Coefficient	Low
Friction Coefficient VS Temperature	Decreasing with temperature
Dynamic braking pressure	High
Static Friction Coefficient	Good
Max allowed temperature	900 °C
Heat sink mass / brake weight	High
Wear parameter	Medium
Number Allowed Braking	Medium
Cost	Low

In case of sintered material vs sintered material (both rotor and stator disc equipped with friction material) max allowed temperature are aligned with the previous scenario and below to 900-950°C. Main advantage to adopt this solution is to obtain higher friction coefficient and a better thermal stability of friction coefficient at different operating temperature. Mean friction factor achievable adopting this technology is typically within the range 0,24-0,27. The two presented solutions are heavier (3,5÷4 times) than carbon fiber solution. The implementation of sintered material both on stator and rotor discs is more expansive than solution implementing friction material only on rotor or stator disc.

**Table 2.** Sintered material coating vs Sintered material coatings Properties

Sintered material VS sintered material	
Design Parameter	Rating
Dynamic Friction Coefficient	medium
Friction Coefficient VS Temperature	Stable with temperature
Dynamic braking pressure	medium
Static friction coefficient	Good
Max allowed temperature	900 °C
Heat sink mass / brake weight	high
Wear Parameter	medium
Number Allowed braking	medium
Cost	Medium/Low

The last configuration is the lightest solution. Carbon fiber material is characterized by low density (1,80 kg/dm<sup>3</sup>) and very high material specific heat (from 1500J/kg\*K for normal braking condition up to 1900J/kg\*K in high temperature condition). Mean friction factor are typically in the range 0,23-0,33, with maximum value up to 0,38-0,40. Dynamic friction factor increases with the material temperature, so the braking capability is better for high energy braking conditions. Other advantage of carbon fiber solution is the wear rate. Discs durations typically 3–4 times than discs made in steel and sintered friction material. In low temperature condition material friction factor is low. For that reason, carbon fiber material solution shows low performance for parking brake conditions (high parking pressure is required). One of most important disadvantage points is represented by unitary cost.

**Table 3.** Carbon Fiber Brakes Properties

Carbon fiber material	
Design Parameter	Rating
Dynamic Friction Coefficient	High for high energy condition
Friction coefficient tVS Temperature	Increasing with temperature
Dynamic braking pressure	Low
Static friction coefficient	Bad
Max allowed temperature	900 ÷ 950 °C
Heat sink mass / brake weight	Low
Wear parameter	Low
Number Allowed braking	High
Cost	High

With the aim of improving the state of art related to aircraft brake materials, starting with the results provided by UAS, the innovative solution proposed is to use rotor and stator discs made in steel, both equipped with a thin coating (e.g. 0.5 mm), obtained with two different thermal spray additive manufacturing technologies, respectively the High Velocity Oxygen Fuel (HVOF) and the Atmospheric Plasma Spraying (APS), of a suitable friction material. In this way the main brake material is steel covered with a noble coating.

The coatings reported in this scientific poster are made by using two different Thermal Spray additive manufacturing technologies, namely High Velocity Oxygen Fuel (HVOF) and Atmospheric Plasma Spraying (APS). The first technology was used to create coatings in Stellite, Colmonoy 6 and Tungsten Carbide, while the APS spraying technology was used to create a coating with a CoNiCrAlY alloy bond coat and a Chromium Oxide layer topcoat. Once created the different coatings the parameters investigated were Tribological Properties (Friction Coefficients and Wear Rate), Structural Properties (Adhesion of coatings on the low-carbon steel substrate, Metallographic Structures and Coating Hardness) and Thermal Properties (Thermal Conductivity and Thermal Diffusivity). An extent of this investigation is recently reported in the literature [2].

## 2. Thermal Spray Technologies and Friction coatings

The first thermal spray technology investigated is High Velocity Oxygen Fuel (HVOF). This is a thermal spray coating process, which is used to improve or restore a component's surface (properties or geometry). This surface

engineering technique better enables life extension of equipment by increasing erosion and wears resistance, and corrosion protection.

HVOF spraying was developed in the 1980s and is a subset of thermal spraying. A common combustion of Kerosene and pure oxygen produces a Mach 2 jet that projects the powder on the substrate giving the highest bond value between coating and substrate (Figure 4).

The HVOF thermal spray process is schematically reported in Figure 4. It's characterized by very high gas and particle velocities, followed by a low gas temperature, as compared to plasma spray processes [3]. Typically, a common combustion of Kerosene and pure oxygen produces a Mach 2 jet that melts or partially melts the powder and projects them on the substrate giving the highest bond value between coating and substrate. These techniques combine high velocity powder particles with low temperature to build up a dense and tightly adherent coating with low oxidation and residual stress [4,5]. Therefore, hard friction material can be applied on many different substrates such as steels, plastic materials, titanium, copper, aluminium, and other different metallic alloys [5]. The application of ceramic coatings obtained via HVOF improves the coated substrate properties, such as corrosion resistance, wear-resistance, hardness or combinations of these to extend product life, to increase performance and to reduce production time and costs. The coating quality, such as physical and mechanical properties of HVOF sprayed coatings are strongly influenced by its structure that depends on the process parameters such as the fuel/oxygen ratio flow rate, nozzle geometry, spray distance and powder size distribution [6].

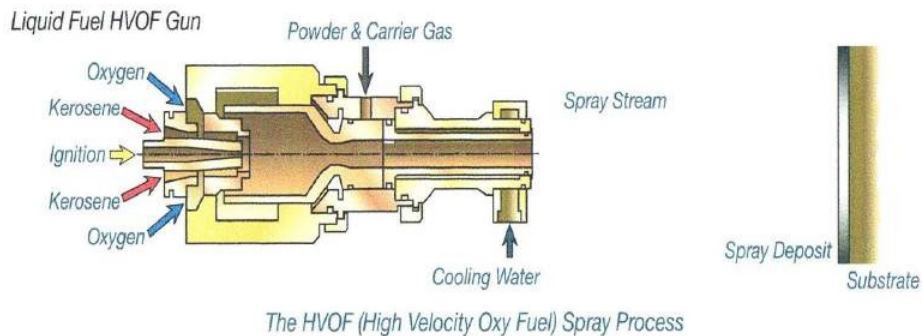


**Figure 2.** High Velocity Oxygen Fuel scheme process

Coating produced with the HVOF technology present several advantages such as, high density (low porosity) due to greater particle impact velocities, high strength bond to the underlying substrate and improved cohesive strength within the coating, low oxide content due to less exposure time, smoother as-sprayed surface due to higher impact velocities and smaller powder sizes, great wear resistance due to harder, tough coatings, improved corrosion resistance due to less through thickness porosity. On the other hand, HVOF spraying process presents some disadvantages. The sprayed coatings result extremely complex, with their properties and microstructure depending upon numerous processing variables; powder sizes are restricted to a range of about 5 - 60  $\mu\text{m}$ , which implies a difficulty in finding the feedstock powders as well as their high cost. As with all the thermal spraying processes, special health and safety concerns must be addressed. HVOF spraying usually needs to be done in a specialized thermal spray booth, with suitable sound attenuation and dust extraction facilities. Furthermore, HVOF spraying requires experienced, qualified personnel to ensure safe operation and to achieve consistent coating quality. Another important factor is HVOF equipment that requires more investment than other thermal spraying processes, such as example flame and arc spraying. Deposition of coatings is difficult or impossible to achieve on to internal surfaces of small cylindrical components, or other restricted access surfaces, because HVOF spraying needs line of sight to the surface and a spray distance of 150-300 mm.

The second thermal spray process investigated is Atmospheric Plasma Spraying (APS). Atmospheric Plasma Spraying scheme is reported in Figure 5. Despite the purpose is the same as for other thermal spray processes, the philosophy at the base of the APS technology is completely different, and surely is the most sophisticated and fascinating one between them.

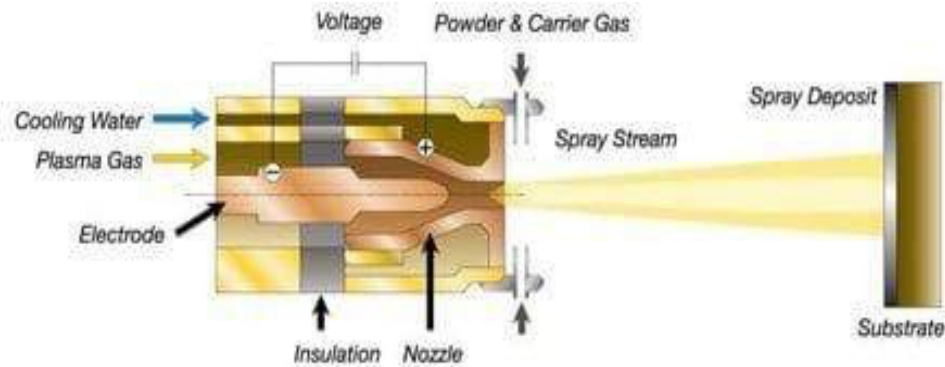
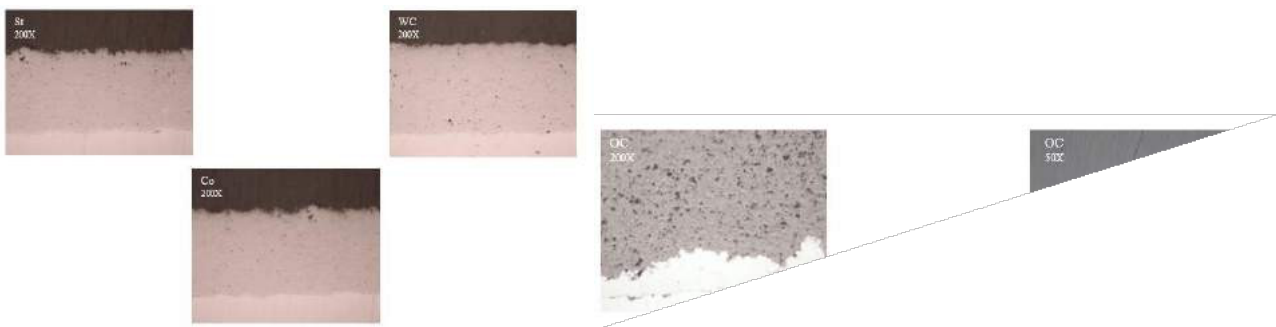


**Figure 3.** Atmosphere Plasma Spraying scheme.

In fact, gas such as Ar, H<sub>2</sub>, N<sub>2</sub>, He, are flowed through an electric arc that drives the gas to become plasma. The result is to produce heat and pressure waves that, investing the powder, transfer kinetic and thermal energy useful to project it onto the substrate. With these technologies it is possible to use a wide range of powders for the realization of different coatings and the choice depends on the properties that the coating must exhibit. The main ones are WC (tungsten carbide), CrC (chromium carbide), Cr<sub>2</sub>O<sub>3</sub> (chromium oxide), Nickel-based alloys, Cobalt-based alloys. The material precursor of the coating could be in the form of powders, wires, melted materials, solutions, or suspensions. What distinguishes the plasma spray process from other technologies is its applicability and capacity to process a wide variety of materials, including metallic and refractory materials at atmospheric pressure. The coatings properties are improved by deposition of coatings with finer microstructure, which are more suitable for mechanical and thermal stresses than the lamellar microstructure of conventional plasma-sprayed coatings. It is widely used to deposit thick coatings (from hundreds of micrometers up to a few millimetres) in a substrate to protect in aggressive environments or to improve its function. APS is commonly used in many industrial sectors, including aeronautics, energy, automotive, mining, biomedical, and electronics. The synthesis of coatings by APS technique occurs by stacking the lamellae resulting from the impact, flattening, and solidification by the colliding molten particles. The material precursor of the coating can be in the form of powders, wires, melting materials, solutions, or suspensions. In this technique, a carrier gas conducts the material particles by injecting them at high velocity through the plasma, where they are molten or partially molten, taking the form of droplets that settle and solidify on the surface being coated. The material to be deposited is carried in the form of a solution or powder to a torch with sufficient enthalpy to generate a plasma jet to melt the particles. The parameters of the plasma spraying process, as well as the characteristics of the precursor (solids or liquids) used for coating, influence the properties of the deposited materials. Characteristics of the coatings such as porosity, atomic structure, roughness, cohesion, and adhesion are fundamentally related to the interaction of the precursor with the plasma jet. The main driving force for the manufacture of thick coatings by APS is their high deposition rate; a few kilograms per hour of raw material can be processed with torches, with a power level of a few tens of kilowatts at a relatively low operating cost. Plasma spray is probably the most versatile of all thermal spray processes because there are few limitations of materials that can be sprayed or on the material, size, and shape of the substrate.

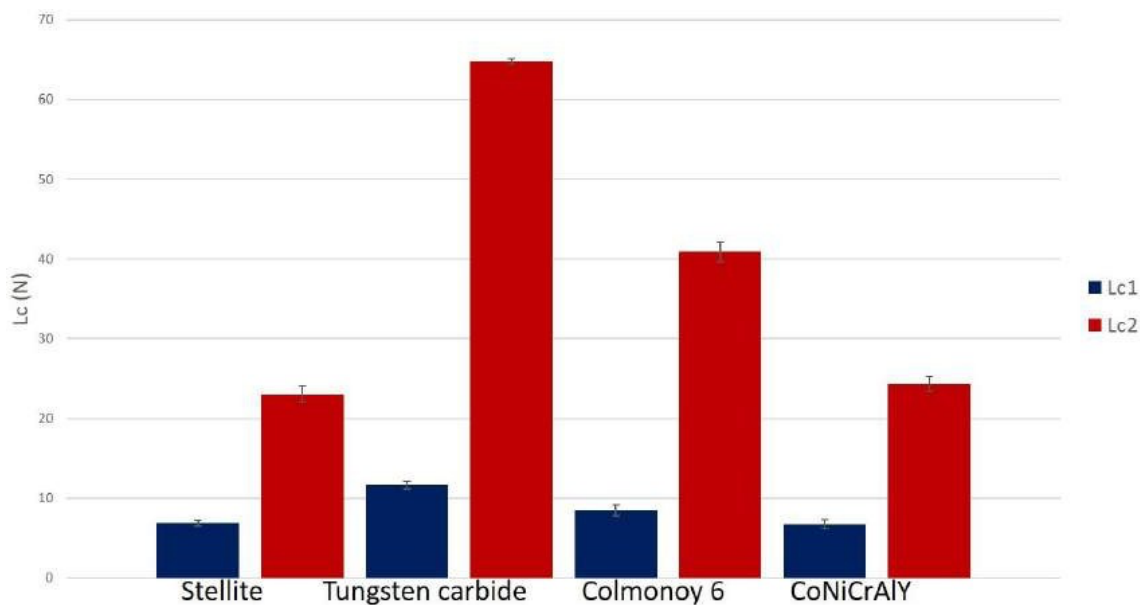
### 3. Result and Discussion

Figure 6 shows the optical microscope morphologies of coatings obtained with the HVOF and APS technologies, respectively. These sprayed specimens have a light grey colour on the entire coated surface, while the Plasma sprayed ones exhibit a dark grey colour on the entire coated surface. As reported in Table 6, the HVOF spray coatings present a very low level of porosity (less than 1%), absence of un-melted particles, a very low present of oxides and no cracks. No interface separation and contamination between the different materials present into the coatings were observed.



**Figure 4.** Left: Metallographic examination of Stellite 1, Colmonoy 6 and Tungsten Carbide. To the right metallographic examination of CoNiCrAlY bond coat and Chromium Oxide topcoat.

In addition to the microstructures, the adhesion between coating and low-carbon steel substrate was also evaluated. The Scratch tests on Stellite 1, Tungsten Carbide and Colmonoy 6 coatings are performed. Two different critical loads were evaluated. Critical load 1 (or Lc1) represents the load in which the formation of cracks within the coatings begins; critical load 2 (or Lc2) represents the load where the total detachment of the coating begins. In Figure 7 it is reported the comparison of the two different critical loads of the coatings produced. As shown in this figure, Tungsten Carbide coating shows better adhesion to low-carbon steel substrate. The results show a critical load at the beginning of cracks at about 10 N and a critical load of separation at 65 N.



**Figure 5.** Critical load of cracks begin (blue) and detached (red).

Friction and wear test were carried out on low-carbon steel samples to obtain a comparative starting baseline. Alumina ball wear imprints diameters, for all the tribological test, were in the range between 0.8-0.85 mm. Figure 8 shows the friction coefficients histograms and wear test histograms of each coatings examined are shown in figure 8 and 9 respectively, while their values are reported in Table 6.

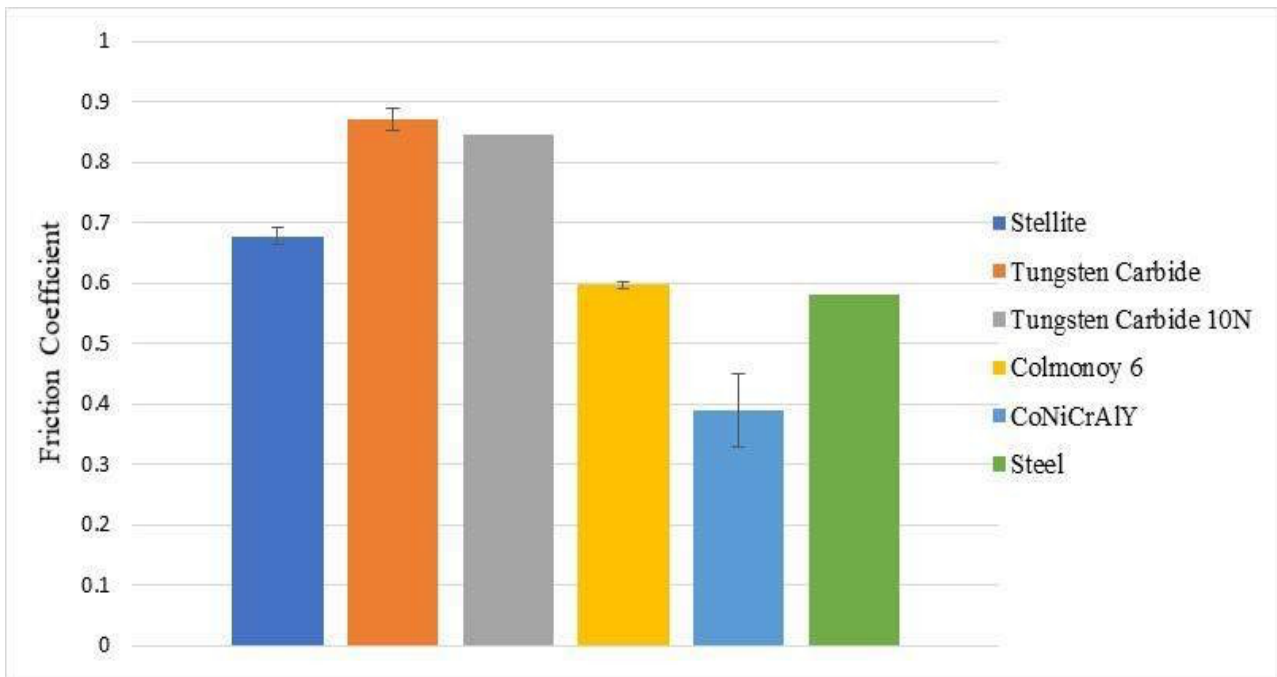


**Figure 6.** Friction coefficient histograms of thermal spray coatings.

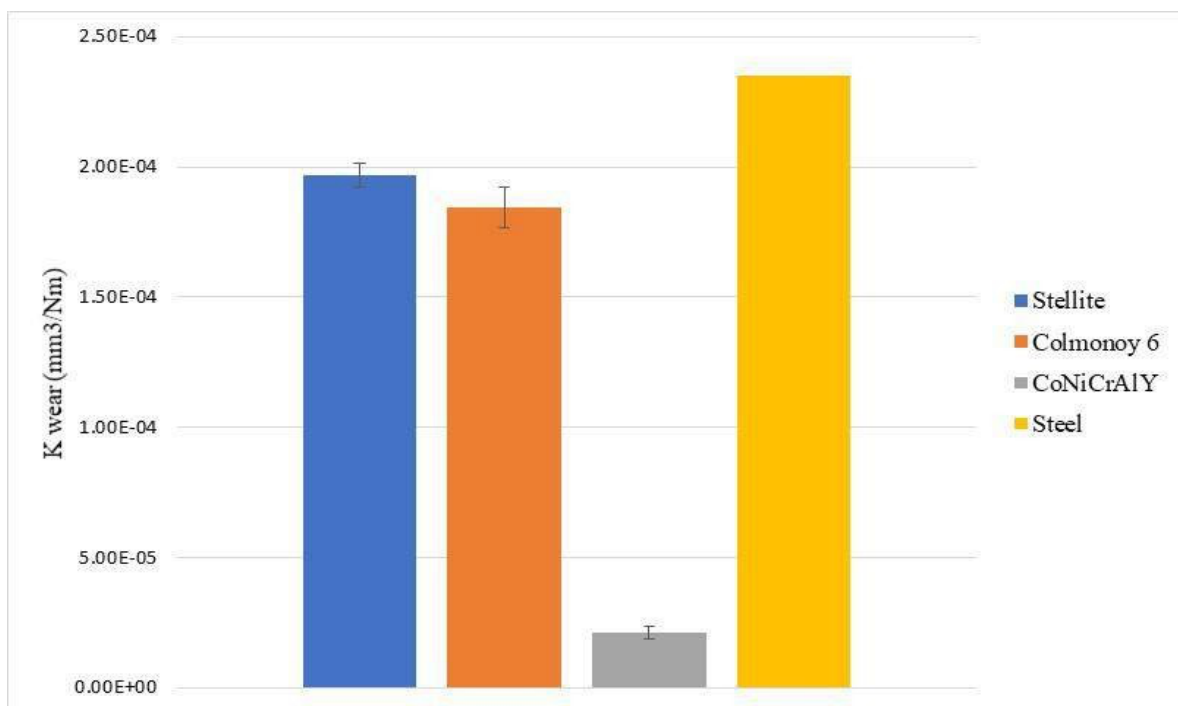


**Figure 7.** Wear rate average histograms of thermal spray coatings.

By comparing the average friction coefficient values among the coatings investigated it is observed that the higher values were exhibited by the Tungsten Carbide at 5 and 10 N, while Colmonoy 6 samples showed much higher wear resistance compared to Stellite 1, while Cr<sub>2</sub>O<sub>3</sub> exhibited a higher wear resistance.

The wear rate results exhibited by the Tungsten Carbide coating were not reported in this figure due to the impossibility to measure wear tracks in this case. The reason of the lack is due to the impossibility to measure wear tracks. In fact, tests carried out for Tungsten Carbide coatings at both tests (5 and 10 N), the surfaces of the specimens were only flattened.

**Table 4.** Friction coefficient and wear average

	Friction Coefficient Average	Wear Rate Average (mm <sup>3</sup> /Nm)
Stellite 1	0.68	2,00·10 <sup>-4</sup>
Tungsten Carbide at 5N	0.87	N/A
Tungsten Carbide at 10N	0.84	N/A
Colmonoy 6	0.60	1,80·10 <sup>-4</sup>
CoNiCrAlY bond coat and Chromium Oxide top coat (OC)	0.39	2,50·10 <sup>-5</sup>

Figures 11 and 12 show, respectively, the thermal conductivity and diffusivity histograms of the produced coatings.

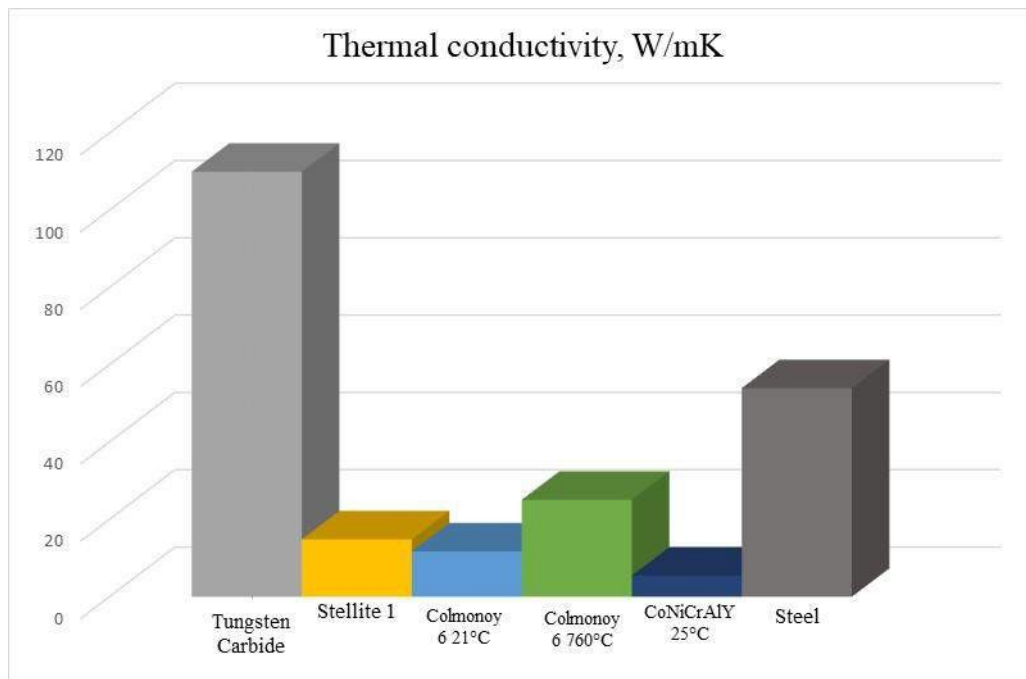


**Figure 8.** Thermal conductivity and thermal diffusivity of analysed coatings.

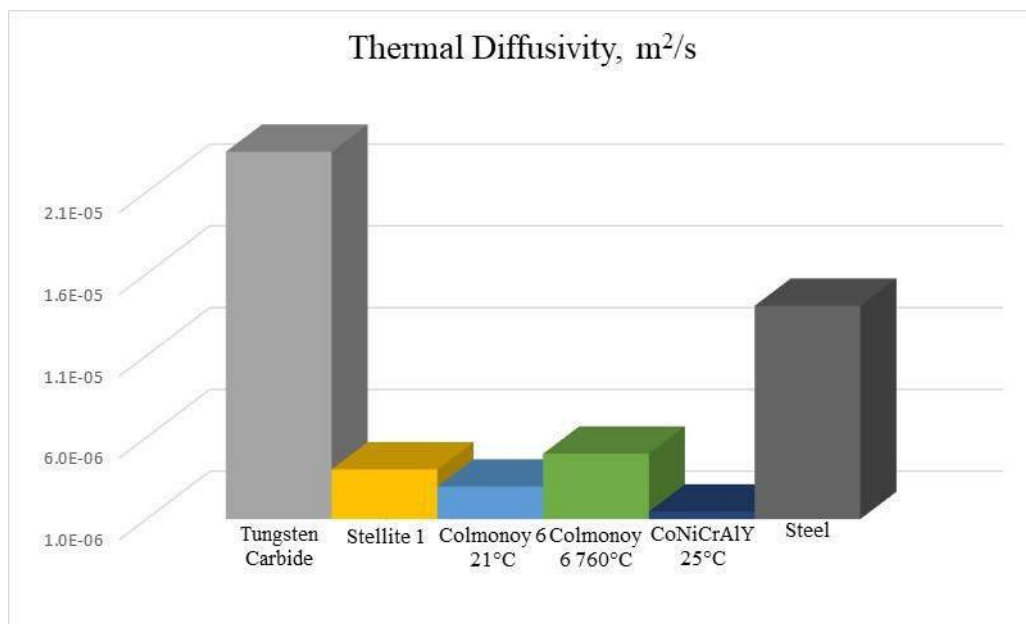


**Figure 9.** Thermal diffusivity of analysed coatings.

As a matter of fact, all coatings analysed exhibit lower thermal properties compared to that shown by the low-carbon steel substrate, except for the tungsten carbide. In fact, as reported in Figures 16 and 17, considering the thermal conductivity and diffusivity results at the same time it can be concluded that the Tungsten Carbide coating presents the better thermal properties compared to the other investigated coatings.

#### 4. Conclusion

In this presentation, different coatings for aircraft brake application produced with two thermal spray technologies were analysed. Results obtained in this investigation can be summarized as follows:

1. The HVOF sprayed specimens' structures present a light grey colour on the entire coated surface, while the Plasma sprayed one's exhibit a dark grey colour on the entire coated surface. The coatings present a very low level of porosity (less than 1%), absence of un-melted particles, a very low presence of oxides and no cracks. No interface separation and contamination between the different materials present into the coatings were observed. Similar hardness values were obtained for all the tested coatings.
2. All the coatings produced, except for Cr<sub>2</sub>O<sub>3</sub>, exhibit higher friction coefficient and wear resistance compared to the low-carbon steel substrate. Among all tungsten carbide shows the highest friction coefficient (0.84).
3. All the coatings show higher wear resistance compared to the low-carbon steel substrate. It is worth to mention that the results shown by the tungsten carbide coating were not reported due to the impossibility to measure the wear tracks at both the nominal loads employed (5 and 10 N).
4. Scratch tests results showed a high adhesion of coatings on the low-carbon steel substrate. In fact, all the specimens exhibit high critical loads related to the crack initiation and the detachment of the coating. Also in this case, tungsten carbide coating presents the better adherence to low-carbon steel substrate. The results show a critical load at the beginning of cracks at about 10 N and a critical load of separation at 65 N.
5. All analysed coatings exhibit lower thermal properties compared to low-carbon steel, except for the tungsten carbide. In fact, tungsten carbide coating exhibits high thermal conductivity (about 110 W/mK) and diffusivity (about  $2.34 \cdot 10^{-5}$ ). This means that coatings made in tungsten carbide has high capacity in propagate the thermal field even in non-stationary conditions without accumulating it into the braking rotor-stator interfaces avoiding the overheat of the friction surfaces with catastrophic consequences.

Carrying out a comparative analysis of the results obtained, it can be concluded that the tungsten carbide coating exhibits superior properties compared to the other investigated coatings. Therefore, a small tungsten carbide thickness (0.5 mm) can improve the braking action without greatly altering the brake weight. The application of this coating presents an additive cost, but thanks to its high properties, the braking action improves, and the brake

wear is reduced, and its life in-service is improved.

In the light of these results, for the future work, analysis about the variation of friction coefficient and wear rate of the coating materials reported as a function of temperature can be performed. Furthermore, another fundamental aspect may concern the stability of friction coefficient (dynamic and or static) and, also, the wear rate stability of the friction coatings analyzed.

### Acknowledgements

The authors acknowledge the financial support of Clean Sky 2 Joint Undertaking (CS2JU), EU Horizon 2020 research and innovation program, under project no. 821079, E-Brake.

Heartfelt thanks also to all the partners involved in the project, Piaggio Aerospace, MaGroup, Mare Group, Università degli studi di Perugia, Umbria Aerospace System.



## **References**

1. Massimo Paoletti, Luca Lini, “Brake Material Selection Criteria”, 2018, UAS Report Document
2. M. Granata, G. Gautier di Confienigo, D. Scamardella and F. Bellucci, “Potential Coatings For Aircraft Brakes Application. Part I: Thermal Spray Coatings”, 2021, International Journal of Astronautics and Aeronautical Engineering, in press.
3. E. Dongma, M. Wenzelburger, R. Gadow, “Analysis and optimization of the HVOF process by combined experimental and numerical approaches”, 2008, Surface & Coatings Technology 202, Elsevier, 4470-4478.
4. V. Sobolev, J.M. Guilemany, J. Nutting, “High Velocity Oxy-Fuel Spraying”, 2004, Maney, p. 397.
5. L. Pawlowsky, “The Science and Engineering of Thermal Spray Coatings”, 1995, Wiley.
6. T.S. Sidhu, S. Prakash, R.D. Agrawal, “State of the Art of HVOF Coating Investigations”, 2005, Marine Technology Society Journal, Volume 39, Number 2, p. 53-64.